Westaway, R. (2017) Integrating induced seismicity with rock mechanics: a conceptual model for the 2011 Preese Hall fracture development and induced seismicity. In: Rutter, E. H., Mecklenburgh, J. and Taylor, K. (eds.) *Geomechanical and Petrophysical Properties of Mudrocks.* The Geological Society of London, pp. 327-359. (doi:10.1144/SP454.12)

This is the author's final accepted version.

There may be differences between this version and the published version. You are advised to consult the publisher's version if you wish to cite from it.

Deposited on: 25 January 2017

Integrating induced seismicity with rock mechanics: a conceptual model for the 2011 Preese Hall fracture development and induced seismicity

Rob Westaway
School of Engineering, University of Glasgow,
James Watt (South) Building, Glasgow G12 8QQ, U.K.

e-mail: robert.westaway@glasgow.ac.uk

Abstract
By integrating multiple datasets with relevant theory, covering fluid injection and fracturing, a conceptual model has been developed for the fracture development and induced seismicity associated with the fracking in 2011 of the Carboniferous Bowland Shale in the Preese Hall-1 well in Lancashire, NW England. Key features of this model include the steep fault that has been recognized adjoining this well, which slipped in the largest induced earthquakes, and the presence of a weak subhorizontal 'flat' within the depth range of the fluid injection, which was 'opened' by this injection. Taking account of the geometry of the fault and the orientation of the local stress field, the model predicts that the induced seismicity was concentrated ~700 m SSE of the Preese Hall-1 wellhead, in roughly the place where microseismic investigations have established that this activity was located. A further key observation, critical to explaining the subsequent sequence of events, is the recognition that the fluid injection during stage 2 of this fracking took place at a high net pressure, ~17 MPa larger than necessary. As a result, the fluid injection 'opened' a patch of the 'flat', making a hydraulic connection with the fracture network already created during stage 1. Continued fluid injection thus enlarged the latter fracture network, which ultimately extended southward far enough to intersect the steep part of the fault and induce the largest earthquake of the sequence there. Subsequent fluid injection during fracking stages 3 and 4 added to the complexity of this interconnected fracture network, in part due to the injection during stage 4 being again under high net pressure. This model can account for many aspects of the Preese Hall record, notably how it was possible for the induced fracture network to intersect the seismogenic fault so far from the injection point: the interconnection between fractures meant that the stage 1 fracture continued to grow during stage 2, rather than two separate smaller fractures, isolated from each other, being created. Calculations indicate that, despite the high net pressure, the project only 'went wrong' by a narrow margin: had the net pressure been ~15 MPa rather than ~17 MPa the induced seismicity would not have occurred. The model also predicts that some of the smaller induced earthquakes had tensile or 'hybrid' focal mechanisms; this would have been testable had any seismographs been deployed locally to monitor the activity. The analysis emphasizes the undesirability of injecting fracking fluid under high net pressure in this region, where flat patches of fault and/or subhorizontal structural discontinuities are present. Recommendations follow for future 'best practice' or regulatory guidelines.

Supplementary material: Background information on the stratigraphy, structural geology, rock-mechanical properties of the study region, and its state of stress, as well as theory for fluid injection, hydraulic fracturing, and Coulomb failure analysis, is available at http://**********************************.

Introduction
The first attempt at fracking for shale gas exploration in the UK took place in the Preese Hall-1 (PH1) well near Blackpool, Lancashire (Figs 1, 2), in the spring of 2011. It resulted in a sequence of ~50 induced earthquakes (e.g. Galloway 2012), including two that were felt, on 1 April (magnitude M_L 2.3) and 27 May (M_L 1.5). Earthquakes of this size constitute a nuisance, rather than a hazard (e.g. Westaway & Younger 2014; Westaway 2015); they caused no injuries or damage to property. Even so, the adverse public reaction was severe, including sustained attacks on the personal integrity

of researchers involved (e.g. Smythe 2015), and has proved to be a major reason why a UK shale gas industry has hitherto failed to develop. Such an outcome following any instance of induced seismicity might have been anticipated, given the public reactions in previous years to similar-magnitude induced seismicity in France and Switzerland, as a result of hydraulic fracturing for the development of geothermal energy (e.g. Majer *et al*. 2007; Häring *et al*. 2008; Deichmann & Giardini 2009).

Figure 1 here: Preese Hall map
Figure 2 here: regional map

A variety of physical mechanisms has been proposed for such occurrences, in which the causative factor for the induced seismicity might be the physical properties of the rocks being fracked, or the properties of the faults that slip in the induced earthquakes, or the pattern of pressure variations in the fracking fluid (e.g. Davies *et al*. 2013; Hitzman *et al*. 2013; McClure 2015; Maxwell *et al*. 2015). It has also been proposed that the likelihood of induced seismicity that is strong enough to be felt relates to the pre-existing state of stress in the rock mass being fracked (e.g. Westaway 2016a). The aims of the present study are to develop a working hypothesis for the combination of physical processes responsible for this occurrence of induced seismicity, to thus establish the geomechanical reason(s) why the PH1 project 'went wrong', and to thereby identify lessons learned that might benefit future projects or inform the regulatory process. Ideally, the workflow for such an analysis should involve integration of geomechanical and microseismic analysis, maybe as suggested by Maxwell (2011), with each feeding back to influence the other. However, this approach is not possible in this instance, given the lack of microseismic monitoring during the fluid injection. The present study will therefore integrate diverse geomechanical data and *in situ* stress data, with the objectives of explaining the limited information available regarding the induced seismicity and making predictions concerning the sequence of physical processes that occurred.

A significant feature of the PH1 case study was the wellbore deformation documented following the largest of the induced earthquakes (e.g. de Pater & Baisch 2011). Although Harper (2011) suggested candidate mechanisms whereby these occurrences might have been causally related, de Pater & Baisch (2011) were more equivocal regarding any cause-and-effect connection, while de Pater & Pellicer (2011) concluded that it was 'unlikely' that the 1 April 2011 earthquake caused the wellbore deformation. On the other hand, Green *et al*. (2012) later asserted that this wellbore deformation was 'clearly related' to the largest induced earthquake but provided no indication of how. However, Green *et al*. (2012) also noted that wellbore deformation is quite common in shale plays, as others (e.g. Dusseault *et al*. 2001) have previously reported, and often occurs independently of induced seismicity, thus raising the possibility that these phenomena might not necessarily have been causally related. The starting points for the present study are the recognition, first, that the wellbore deformation occurred within a subhorizontal weak zone that appears to be the updip continuation of the seismogenic fault (Figs 3, 4; see, also, below) and, second, that the induced seismicity occurred south of the PH1 well (Westaway 2016a; Fig. 1) at a greater distance than one would expect from the likely dimensions of the induced fracture that might be predicted following each of the fracking stages, given the volumes of fluid injected (Tables N1 and N2). These aspects will inform the development of the resulting conceptual model, which will be used to assess the stress perturbations that resulted from the fluid injection.

Figure 3 here: 1980s seismic section
Figure 4 here: section through 3D seismic survey

The present study is thus largely concerned with calculating pressure variations in the fluid injected into the PH1 well during the five fracking stages in 2011, and developing a conceptual model for how

these variations caused the induced seismicity and wellbore deformation. As Green *et al.* (2012) have discussed, three previous attempts at such an analysis have been made: by the PH1 well operator, Cuadrilla (but not been placed in the public domain); by G Frac Technologies (also not placed in the public domain); and by de Pater & Pellicer (2011). According to Green *et al.* (2012), the Cuadrilla analysis produced results that differ significantly from the other two. The de Pater & Pellicer (2011) analysis (results summarized in Table N2) will serve as a benchmark for comparison with the present analysis. As Green *et al.* (2012) noted, 'incorrectly analysed stress data will lead to a misunderstanding of the in-situ stress and leakoff mechanisms, so that subsequent jobs are incorrectly designed'. To anticipate the present conclusions, it would now indeed appear that the PH1 dataset has hitherto been analysed incorrectly. As will be explained in more detail below, the most important aspect would seem to be the dataset from the 'mini-frac' ahead of fracking stage 2, which yielded an estimate of the minimum principal stress at the injection depth that was much too high. As a result, fluid was injected at much too high a pressure during the main stage 2 frack, which 'opened' hydraulic pathways and led to the induced seismicity.

It is indeed noted that much of the data pertaining to the PH1 case study has not (? yet) been placed in the public domain. Before the present work was undertaken, efforts were made to secure release of data that would have strengthened the conclusions, as well as saving a great deal of time by avoiding having to 'reverse engineer' published outputs, for example digitizing diagrams to recover numerical information. It has, however, been necessary to make the best use of the incomplete information available. Hitherto, various other difficulties have also hampered attempts to establish a satisfactory working hypothesis or conceptual model for the PH1 induced seismicity and geomechanics, including inconsistencies, mistakes and unwarranted claims in published outputs. For example, the statements by de Pater & Baisch (2011) that similar induced seismicity has a probability of re-occurrence of one instance for every 10,000 wells fracked, and that no significantly larger induced earthquake is feasible, are open to question (e.g. Westaway & Younger 2014; Westaway 2016a). The Clarke *et al.* (2014) analysis of this induced seismicity also contains some bad mistakes, corrections having subsequently been published (e.g. Westaway 2016a). Another difficulty concerns the stratigraphy penetrated in the PH1 well. It has belatedly emerged (e.g. Clarke 2016) that this was incorrectly determined at the time of the project. The corrected stratigraphy was released in 2015 through Release Agents who handle UK onshore petrophysical data, although such access does not permit reuse of such data in academic publications. Until this amended stratigraphy is published one is obliged to continue using the older, incorrect version. A final issue, recognized for the first time in the present study, concerns the local stress field. Recent works (e.g. Westaway 2015, 2016a) have taken as definitive the seemingly clear summary description of this by Cuadrilla (2014). However, it has since emerged that this version contains invalid numerical results, due to making incorrect use of outputs from de Pater & Baisch (2011) (see below). This aspect will thus be revisited, so corrected values can form the basis of continuing research.

Many conclusions reached in previous reports on the PH1 case study are indeed contradictory (see below). Much of this work was carried out by specialist consultants who, whilst knowledgeable in their own field, seem to have not been entirely familiar with the study region, including known issues such as its high differential stress (Fig. 5). Such information, which will be familiar to other readers, is briefly summarized here, with a more detailed synthesis in the supplementary material. Likewise, although many fracking specialists will be aware of the underlying body of theory (for instance, as incorporated into industry standard software packages such as FRACPRO), this material will be unfamiliar to a wider audience so will likewise be summarized in the supplementary material. The opportunity will also be taken to clarify some aspects and add to this body of theory. As will become clear, some aspects of the de Pater & Pellicer (2011) analysis require amendment. Rather than using packaged software, the necessary re-analysis will involve transparent analytic calculations based on first principles, harmonized with the resulting conceptual model.

Detailed background information on the PH1 study locality, including its structural setting and the regional state of stress, is contained in the supplementary material. A brief summary of the key points is provided here, including Table N1 and Figs. 3, 4, and 5.

Table N1 here: summary information for the Preese Hall-1 well
Figure 5 here: Stratigraphic column and stress data

Figure 3 depicts a seismic section, dating from the 1980s, through the PH1 site (see Fig. 1 for location). It thus provides an indication of the data available prior to the PH1 project. Figure 4 depicts a published excerpt from the 3-D seismic survey shot in 2012, indicating what is known regarding the local structure now. A steep fault with a component of downthrow to the east is recognizable in Fig. 4, just east of the PH1 well track, from offsets of seismic reflectors, at depths of $\geq$~2650 m (TVD). This fault might project NNE as Fault 2 in Fig. 3; see Westaway (2016a) for more detailed discussion of the correlation between these seismic sections. However, it is clear that this fault does not continue upward with constant dip, there being no offsets of seismic reflectors in line with it at depths of <~2600 m (Fig. 4). It is thus inferred that the fault flattens upward to a subhorizontal dip at a depth of ~2600 m, around the depth where disrupted stratigraphy is evident in Fig. 4 and wellbore deformation occurred in the PH1 well (e.g., Baker Hughes, 2011; Harper, 2011). As already noted, the presence of this subhorizontal zone of disrupted stratigraphy, or zone of weakness, at ~2550-2590 m depth (TVD) - within the depth range of fluid injection (Table N1) – plays a key role in the proposed conceptual model for why the PH1 project 'went wrong'. High net pressure of fracking fluid will be shown sufficient to have 'opened' this structure, resulting in horizontal migration of fracking fluid. The supplementary material discusses the nature of this zone, which bears upon how widespread similar structural complexities are likely to be, and thus what impact they might have on any future UK shale gas industry.

It is evident that at Preese Hall the maximum and minimum principal stresses are horizontal, being designated as σ_H and σ_h, with the intermediate principal stress vertical, designated by σ_V (Fig. 5(b)). However, the azimuths of these horizontal principal stresses have proved contentious, not least given the evidence that these orientations vary vertically, so differ between the Bowland Shale and younger formations (Fig. 5). These complexities are discussed, in relation to the regional context of high differential stress, in the supplementary material. The present study follows Westaway (2016a) by adopting as the best evidence for the stress field orientation in the Bowland Shale the dataset of borehole breakouts and drilling-induced tensile fractures from Harper (2011). Westaway (2016a) thus determined a mean azimuth for σ_H of 187$\pm$3° ($\pm$2s) or N7$\pm$3°E-S7$\pm$3°W ($\pm$2s). Since hydraulic fractures develop in the plane perpendicular to the minimum principal stress, it is expected that these propagated away from the PH1 well in the vertical plane oriented N7$\pm$3°E-S7$\pm$3°W ($\pm$2s) (Fig. 1).

Since the present analysis requires principal stress magnitudes at many depths, these have been determined (for TVD $\geq$2400 m, covering most of the analysis) as curves of best fit through the numerical integrals depicted in Fig. 5(b). Gently curving parabolas, matching the slight vertical variations in stress gradients identified by de Pater & Baisch (2011), are fitted thus:

$$\sigma_H \quad = \quad 63257 + 28.054 \, (z_T - 2400) + 0.00022992 \, (z_T - 2400)^2 \, , \qquad (1)$$

$$\sigma_V \quad = \quad 54270 + 23.901 \, (z_T - 2400) + 0.00027830 \, (z_T - 2400)^2 \, , \qquad (2)$$

and

$$\sigma_h \qquad = \qquad 39200 + 16.923 \, (z_T - 2400) + 0.00034100 \, (z_T - 2400)^2 \,, \qquad (3)$$

with z_T in metres (TVD) and principal stresses in kilopascals.

The ~23.9 kPa m^{-1} vertical stress gradient (equation (2)), is less than one might expect if σ_V equates to the weight of overburden (cf. McGarr & Gay 1978). Given the typical density of the Bowland Shale (e.g. Baker Hughes 2011) a vertical stress gradient of ~2620 kg m^{-3} × g or ~25.7 kPa m^{-1}, ~8% larger, might be expected. However, vertical stress is widely observed to differ from the weight of overburden by up to ~30%, either above or below (e.g. McGarr & Gay 1978). As many authors (e.g. Cosgrove 2001) have noted, σ_V will equal the weight of overburden in a rock mass that has not experienced any horizontal components of strain. However, the faulting, folding and tilting evident within the Bowland Shale at Preese Hall (Figs. 3, 4) indicate horizontal components of strain. There is thus no reason to expect σ_V to precisely equal the weight of overburden in this locality.

The present analysis also requires conversion to true vertical depth (TVD) of data (e.g., depths of well casing perforations; Table N1) that have been reported in terms of measured depth (MD) in the deviated PH1 well. A formula to represent the well track both in plan view and in cross-section has thus been devised, to approximate for modelling purposes various depictions by de Pater & Baisch (2011) and Clarke *et al*. (2014) of this deviated well, to illustrate the results of the present study. In summary, at 2400 m depth (TVD) the model well passes 99.753 m east of and 4.987 m south of the wellhead. At depths $\geq$2400 m (TVD) it is assumed to plunge at 62° at an azimuth of 114°. At depths (TVD) $z_T \geq$2400 m, z_T and measured depth (MD), z_M, therefore interrelate thus:

$$z_T \qquad = \qquad 2400 + (z_M - 2417.388) \times \sin(62°) \,. \qquad (4)$$

Previous analyses of the Preese Hall case study

Many reports have been written on the PH1 case study: those in the public domain include Baisch & Vörös (2011), Baker Hughes (2011), de Pater & Baisch (2011), de Pater & Pellicer (2011), Harper (2011), and Green *et al*. (2012); others have not been made public. Notwithstanding this quantity of material, there has been no published discussion of a range of topics. For example, there has been no publication of any reported estimation, prior to the fracking taking place, of the expected dimensions of the induced fracture networks. It is thus unclear whether it was expected that fracture height growth would be constrained by overlying or underlying rock layers or would instead be governed by the volumes of fluid injected. There is also no evidence of any consideration before the fracking proceeded of potential consequences of the high differential stress $\Delta\sigma$ in the study region, or of interactions between induced fractures and faults. The latter point was potentially significant since the existing seismic reflection data show several faults in close proximity (Fig. 3). It is also unclear whether the evidence from the PH1 well of high $\Delta\sigma$ at depth (Fig. 5(b)) was reported ahead of the decision to proceed with the fracking, nor whether it had been appreciated that the combination of circumstances (fracking fluid at high net pressure [see below], high $\Delta\sigma$, and a fault in close proximity) was a potentially 'risky' combination (cf. Figs 3, 4, 5(b)). Although (before the PH1 microearthquake sequence) no earthquake large enough to be felt had been induced as a result of fracking for shale gas, the potential effect of fluid injection as a cause of anthropogenic earthquakes was already well known (e.g. Nicholson & Wesson 1990; Davis & Frohlich 1993; McGarr *et al*. 2002), many case studies having been documented (e.g. Raleigh *et al*. 1976; Herrmann *et al*. 1981; Seeber *et al*. 2004; Majer *et al*. 2007).

As was noted above, the only previous public-domain analysis to link PH1 fluid injection pressure variations with their geomechanical consequences has been by de Pater & Pellicer (2011). This work used the software package FRACPRO (Carbo Ceramics Inc., Houston, Texas), but many of the model

parameters have not been disclosed. Along with the lack of sensitivity analysis, this makes it difficult to have confidence in the robustness of this modelling. Furthermore, most of the predicted pressure variations do not match those of the bottom hole pressure (BHP) (calculated from well head pressure, WHP) well, indeed raising the possibility that many other solutions (not presented) might fit the underlying data equally well (or equally badly). This modelling also omits some essential physical aspects, notably whether or not the fluid pressure exceeded σ_V. Notwithstanding the lengthy discussion of this topic by de Pater & Pellicer (2011), their modelling thus sheds no light on whether the fluid pressure could open horizontal zones of weakness enabling fluid to flow horizontally.

Table N2 here: De Pater and Pellicer results

Several aspects of this warrant attention. The first is the analysis by de Pater & Pellicer (2011) of the minimum principal stress (or 'fracture closure pressure', p_C, in fracking terminology). Rather than being based on subsurface measurements (as in the present study), this is determined from variations in WHP during the mini-frac preceding each 'main frac'. These authors calculated the resulting 'G-functions' (cf. Nolte & Smith 1981) for the pressure variations estimated at the injection point (i.e., for the corresponding variations in BHP), then analysed these G-functions using an industry-standard 'rule of thumb', the 'tangent method', to obtain p_C. However, recent work, notably by McClure *et al*. (2016), indicates that this method can produce incorrect estimates for p_C, including values that are much too high; these authors thus advocate their alternative 'fracture-compliance method'. Rather than revisiting either of these methods or any other industry 'rules of thumb' (discussed, e.g., by McClure *et al*. 2015, 2016), the present analysis will be based on minimum principal stress values calculated for each depth of injection using equation (3). Table N1 compares these values with those used by de Pater & Pellicer (2011).

A second issue concerns the great diversity of geomechanical interpretations that have been proposed. For example, Harper (2011) placed great emphasis on thin interbedding of shale and other lithologies at PH1, even though the Bowland Shale is well known to be homogenous across larger scales. Harper (2011) also reported that many bedding planes are fractured and show signs of shear displacement. He, indeed, asserted that these planes were permeable and enabled fracking fluid to flow through the Bowland Shale. These discontinuities were also discussed in some detail by de Pater & Baisch (2011), although no clear conclusions were reached by these authors regarding their role in the sequence of events in 2011 (for example, whether significant flow through them might have occurred). Although more recent work (e.g. Zhang & Li 2016; Rutter & Mecklenburgh 2017) suggests that shear discontinuities in shale, such as these, will in general be impermeable, the impression created by the PH1 studies (especially that by Green *et al*. 2012; see below) is, on the contrary, that flow along bedding planes in the Bowland Shale is an established process and causes the bulk permeability of this rock to be orders-of-magnitude higher than the expected matrix permeability. A second geomechanical issue concerns the geometry of the wellbore relative to any seismogenic fault. Baisch & Vörös (2011) argued that at ~2600 m depth the wellbore cut directly through the seismogenic fault plane, which they assumed had a SW strike and a 60° dip to the NW, so fluid was injected directly into the fault. However, this geometry is not supported by abundant evidence now available, such as the earthquake focal mechanism and the epicentral locations to the south of the well (Fig. 1). de Pater & Pellicer (2011) also inferred that the fluid was probably injected into the fault via the wellbore, fluid flowing from each depth of injection through the well annulus (inferred to have been incompletely cemented) to reach the fault-wellbore intersection. These authors also raised as another possibility (which they did not favour) that the fluid might have reached the fault via opened bedding planes, although no analysis of this mechanism was presented. However, neither of these possibilities was incorporated into their analysis using FRACPRO; clearly, if either of them occurred, this numerical modelling (being based on a different set of assumptions)

would have been invalidated. Conversely, Green *et al*. (2012) favoured the possibility that the fluid indeed reached the fault via opened bedding planes, although once again no analysis was presented to establish feasibility. Notably, these latter authors envisaged that most of the fluid was injected subhorizontally, opening bedding planes, implying that the de Pater & Pellicer (2011) analysis, predicting the development of extensive vertical fracture sets governed by the orientation of the present-day stress field (Table N2), was incorrect.

A third, related, issue concerns the role of leak-off and the dimensions of the resulting induced fractures. de Pater & Pellicer (2011) noted the rapid pressure decline following the small-volume 'mini-frac' fluid injections into the PH1 well and concluded that these probably related to escape of fluid into fissures or opening of bedding planes, indeed implying a bulk permeability for the Bowland Shale many orders-of-magnitude larger than might reasonably be expected. On the other hand, they modelled subsequent 'main frac' development using a nominal 0.1 μD (~10^{-19} m^2) permeability, representative of shale (cf. Heller *et al*. 2014), but were unable to resolve this evident contradiction. The FRACPRO modelling by de Pater & Pellicer (2011) estimates that fracture growth took up typically about half the injected 'main frac' fluid volume (Table N2), consistent with very low permeability. de Pater & Pellicer (2011) presented solutions assuming the development of a single fracture set or ten parallel fractures fed by leakage through 'opened' bedding planes. It was not explained where the idea to model en echelon fractures originated, as one would usually expect such a geometry under low differential stress (cf Gale *et al*. 2007), not in the present study region with its high differential stress (see Fig. 5 and the supplementary material). Moreover, if leakage had indeed occurred in this manner, involving opening of many bedding planes, one would expect to see a correlation between the volume lost by leakage and fracture height, but no such correlation is evident (Table N2). In the present author's view, the most likely explanation for the rapid 'mini-frac' pressure declines is that fluid injected during 'mini-fracs' escaped through the incompletely cemented well annulus (cf. de Pater & Pellicer 2011). Conversely, during the 'main frac' injections, when proppant was injected, this pathway became blocked and induced fractures were created.

The publication by Clarke *et al*. (2014) of the seismic section in Fig. 4 shed some light on the above issues, especially after Westaway (2016a) created this more clearly labelled version indicating how it relates to the local stratigraphy. Thus, circa 2600 m depth (TVD) a zone of deformed stratigraphy including thinning indicative of a component of top-to-the-west shear is evident. Its depth range corresponds to that of the PH1 wellbore deformation (e.g. Harper 2011), also roughly coinciding with a zone of particularly weak rock, characterized by an atypically low Young's modulus (see Fig. 3.2 of Harper 2011). A steep fault, consistent in orientation with the seismogenic fault plane inferred in Westaway's (2016a) focal mechanism for the induced seismicity, is present nearby (Fig. 4), although this is not observed at shallower depths. Westaway (2016c) thus proposed that this fault may flatten upward into the zone of deformed stratigraphy. If so, the observed wellbore deformation is simply explicable as a consequence of aseismic deformation of the surroundings to the coseismic slip, even though the patch of fault that slipped was hundreds of metres south of this seismic section (Fig. 1). The extant modelling of the height growth of the PH1 induced fractures (Table N2) indicates that several of these intersected this weak zone. The possibility thus arises that the properties of this atypical weak zone, rather than those of the Bowland Shale as a whole, might be responsible for the sequence of events that led to the induced seismicity. This possibility is thus worth exploring; for example, it offers the potential to supersede some of the more contentious ideas that emerged in the succession of reports in 2011-2012, such as the notion that fluid flow along bedding planes is widespread within the Bowland Shale, giving it bulk permeability orders-of-magnitude higher than its expected matrix permeability. From the point of view of the geomechanics, the nature of the 'flat' is immaterial: whether it is indeed a subhorizontal updip continuation of the fault, or a zone of rock that has been deformed and weakened for other reasons,

for example due to a Carboniferous-era palaeo-landslide (cf. Harper 2011), or simply an atypical localized zone of non-cohesive bedding planes.

Fluid injection

The present analysis requires the variations in pressure of the injected fluid at each point of injection. These BHP values were not measured so have to be calculated from other information, including measurements of WHP, as is explained in section 3 of the supplementary material. The calculations of BHP from WHP by de Pater & Pellicer (2011) (used by de Pater & Baisch 2011) were evidently based on the same general method, but no details have been provided other than the results presented graphically (Figs 6(a), 7(a)). The purpose of this analysis, as part of the present study, is so values of σ_h, from equation (3), can be subtracted from the calculated BHP values, to determine the net pressure p_o of the injected fluid at its injection point, as a starting point for predicting hydraulic fracture development (see below, also section 4 of the supplementary material). Notwithstanding the same method having been used, there are many differences in detail between the present predictions of BHP (Figs 6(b)(c), 7(b)(c)) and those reported by de Pater & Baisch (2011) (Figs. 6(a)(ii), 7(a)(ii)). However, as a first approximation the two sets of results are similar, confirming the commonality of approach, notwithstanding the instances (discussed in section 3 of the supplementary material) where some essential parameter values have had to be estimated, the definitive information being unavailable. By the end of each stage of injection, substantial sets of induced fractures evidently developed; their dimensions determined by de Pater & Pellicer (2011) are listed in Table N2, for comparison with the revised estimates made later in the present study.

Figure 6 here: Analysis of fracking stage 1
Figure 7 here: Analysis of fracking stage 2

A key observation is that when the well was 'shut in' after the stage 1 injection, circa 14:40 on 28 March 2011, BHP peaked at ~60 MPa and then declined over several hours; as already noted, this indicates low permeability within the Bowland Shale (cf. de Pater & Pellicer 2011). Likewise, when the well was 'shut in' at the end of the stage 2 injection, BHP again experienced a progressive decline. However, compared with stage 1, this pressure decline was significantly faster, lasting ~90 minutes rather than the ~3 hour duration following stage 1 (compare Figs 6(c) and 7(c)). de Pater & Pellicer (2011) attributed this difference to leakage of fracking fluid into the seismogenic fault following stage 2, whereas no hydraulic connection with this fault existed during or after stage 1, so this earlier pressure decline involved only slow distributed leakage of fluid into the surrounding impermeable shale; this reasonable inference is supported by the present analysis.

For fracking stage 1 (Fig. 6), the significant differences in detail include, first, that the present prediction makes all three 'spikes' in BHP, at times of low injection rate, comparable in magnitude, ~60 MPa, whereas de Pater & Baisch (2011) predicted successively larger values. Second, it is predicted that with steady injection rates, BHP remained relatively stable, at ~46-49 MPa, whereas de Pater & Baisch (2011) depicted a progressive increase. No explanation for these differences is apparent. It is nonetheless noted that a variation in BHP more akin to that predicted by de Pater & Baisch (2011) would result if the proppant concentration were much higher. As a check on this aspect, 101 tonnes of proppant were injected during stage 1 (Table N1). Given the 11568 barrels (1839 m^3) of fluid, this gives a typical concentration of ~0.46 pounds per gallon (ppg), consistent with Fig. 6(a). Confidence, thus, exists that the present analysis has used the correct proppant density variations. For fracking stage 2 there are again significant differences in detail, likewise not readily explicable. As before, the proppant density has been checked; de Pater & Baisch (2011) reported 117 tonnes injected during stage 2, along with 14120 barrels (2245 m^3) of fluid, giving a typical concentration of ~0.43 ppg, consistent with Fig. 7(a). The present analysis again indicates that while the injection rate was held steady, BHP remained relatively stable, typically ≥60 MPa, peaking at ~66

MPa. Unlike for stage 1, no major BHP spike occurred at the end of injection; this was a result of the gradual reductions in injection rate and WHP, rather than the more abrupt reductions at the end of stage 1. Overall, the present analysis indicates typical BHP ~15-20 MPa higher during stage 2 than during stage 1.

Strictly speaking, the fluid pressure in the vicinity of the injection point, which acts to hold an induced fracture open during injection, will be somewhat less than the BHP, due to the effect of 'perforation friction', the constriction of the flow into the fracture through the relatively narrow perforations in the well casing. de Pater & Baisch (2011) mentioned that their analysis included this effect. However, this cannot be replicated here because the dimensions of the perforations at PH1 have not been made available. Perforation friction typically causes pressure drops in the range ~25-300 psi (~0.2-2 MPa) (e.g. Behrmann $et\ al$. 2000; Jennings 2008) so its effect will be small compared with the variations in BHP noted above. Most of the calculations to be presented for PH1 anyway relate to conditions at the end of phases of injection, when the injected fluid is stationary, so this effect will tend to zero.

As already noted, the purpose of the above calculations of BHP is to facilitate calculation of the net pressure p_o at the injection point, since this parameter has a major effect on induced fracture development (see section 4 of the supplementary material). de Pater & Pellicer (2011) determined the typical and peak net pressure as ~1500 psi (i.e., ~10 MPa) and ~2700 psi (~19 MPa) during fracking stage 1 and as ~1500 psi (i.e., ~10 MPa) and ~2200 psi (~15 MPa) during stage 2. They thus inferred high net pressure during both these fracking stages, but predicted higher peak values during stage 1, which resulted in no induced seismicity, than during stage 2, which was accompanied and followed by induced seismicity. Clarke $et\ al$. (2014) have also previously discussed relations between BHP variations and induced seismicity, but it is apparent that their graph illustrating this point (their Fig. 3) shows WHP but is labelled 'BHP' by mistake. Their discussion of this topic should thus be disregarded (cf. Westaway 2016a). The present calculations indicate, on the contrary, that during most of the stage 2 injection BHP exceeded σ_h by ~15-20 MPa, whereas during stage 1 BHP seldom exceeded σ_h by >3-4 MPa. Indeed, as is discussed in section 3 of the supplementary material, one is obliged to assume very low-friction conditions (smooth wellbore; low-viscosity fluid) to avoid the prediction of zero or negative net pressure during stage 1. The present revised calculations thus indicate much higher typical net pressure during stage 2 than during stage 1, thus establishing a clear correlation between high net pressure and induced seismicity that (although evident elsewhere; e.g. Majer $et\ al$. 2007; Häring $et\ al$. 2008; Deichmann & Giardini 2009) has hitherto gone unrecognized for PH1.

Hydraulic fracturing

The science of fracture mechanics was pioneered at the University of Glasgow by Sir William Rankine (e.g. Rankine 1843, 1858). Subsequent refinements to general theory include the works of Griffith (1921, 1924), Sneddon (1951), Eshelby (1957), and Irwin (1957). Modelling of hydraulic fracture development has since become an extensive field, including the emergence of 'industry standard' software packages such as the aforementioned FRACPRO, significant contributions or syntheses including the works by Nolte & Smith (1981), Brady $et\ al$. (1992), Barree $et\ al$. (2005), Adachi $et\ al$. (2007), Rahman & Rahman (2010), Fisher & Warpinski (2012), Flewelling $et\ al$. (2013), Detournay (2016), and Ma $et\ al$. (2016). In addition to outputs related to shale gas, modelling of hydraulic fracturing for the development of geothermal energy resources is nowadays also technically mature (e.g. Zimmermann $et\ al$. 2010; Yoon $et\ al$. 2014; Blöcher $et\ al$. 2016; Hofmann $et\ al$. 2016). As with any modelling, one needs to strike a balance between avoiding making the task so complicated that it is intractable, and avoiding simplifying assumptions that invalidate essential aspects of the underlying physics. Indeed, much of this cited literature assumes constant fluid pressure within any fracture, which is not in general valid in a region such as Britain where the horizontal minimum

principal stress (Fig. 5(b)) causes fractures (in any mechanically isotropic rock formation) to develop in vertical planes. Much of it is also geared towards U.S. experience of thin shale deposits, where stronger rocks above and below thin 'pay zones' force boundary conditions to the fracture development, and is thus likewise inappropriate in the Bowland Shale, given its great thickness (Fig. 5(a)).

The set of coupled equations to be solved in such analysis is set out in section 4 of the supplementary material. In modern theoretical-fracture-mechanics terminology (e.g. Detournay 2016), the resulting model is an example of a general class known as a 'K-model' or 'K-solution'. It describes the 'quasi-static' situation at the end of fluid injection, without specifying how the fracture developed to reach this solution. The model is defined in terms of horizontal and vertical coordinates, x and y, measured in the fracture plane, and fracture width w, measured perpendicular to this vertical plane. The shear modulus μ and Poisson's ratio ν of the rock encompassing the fracture and the volume of fluid injected, V, are specified. The model determines the fracture dimensions (height H, half-length L, and maximum width w_o) incorporating the vertical gradient in fluid pressure p_F within the fracture, which is expressed using the parameter K (the difference between the vertical gradients of σ_h and of p_F). It also incorporates the effect of net pressure (specified using the parameter M, the ratio of the net pressure at the vertical midpoint of the fracture, at y=0, to the minimum value of $P_o \equiv K \times H/4$ necessary to hold open a fracture of height H) on the dimensions and shape of the fracture, including on its aspect ratio $C \equiv L/H$, on the depth of the base of the fracture, and on the vertical position y_o (measured above the fracture mid-point at y=0) of the maximum fracture width w_o. In this context, 'minimum pressure conditions' means zero net pressure at the injection point, so M=1 and y_o=H/4, placing the base of the fracture at the injection point and the fracture widest three quarters of the way up between this base and its top. The model predicts C=2 so $L \equiv 2 \times H$ under these end member conditions, for which fracture growth only occurs upwards from the injection point. Conversely, with M>1, fracture growth will occur downwards from the injection point (also sideways), as well as upwards. Under high net pressure M>>1 and the fracture is predicted to be equidimensional, with length $2 \times L$ equal to H so C=0.5, and $y_o \rightarrow 0$, placing the mid-point of the fracture at the injection point.

Strictly speaking, the underlying idea of equating the volumes of the fracture and of the fluid injected (e.g. Fisher & Warpinski 2012) is not precisely accurate, because as the fracture propagates the fluid front will lag behind the fracture front. However, as the distance is between these fronts is small, this approximation has no significant consequences (e.g. Adachi et al. 2007; Detournay 2016). In general, the volume of fluid injected will also exceed the fracture volume because some of the fluid leaks off into the surrounding rock mass. The predictions by de Pater & Pellicer (2011) of fracture volumes typically about half of the volumes of fluid injected at PH1 (Table N2) arise as a result. However, the de Pater & Pellicer (2011) analysis arguably assumed too high a permeability for the Bowland Shale; if lower permeability were to be assumed the leak-off would be less and fracture volume would grow closer to that of the fluid injected. Their nominal 0.1 μD value exceeds measurements in Bowland Shale from the Irlam-1 (or Ince Moss) borehole near Manchester, including ~0.04 μD at an effective confining pressure of 60 MPa (Rutter & Mecklenburgh 2017) and 0.03 μD (iGas 2014). As discussed in section 1 of the supplementary material, even lower permeability might be anticipated at PH1 given the different sedimentary facies. However, given that the fracture dimensions (H and L) depend on the fourth root of the fracture volume (see section 4 of the supplementary material), 50% leak-off will only reduce these dimensions by ~16%. With the measured lower permeability, this reduction will be closer to ~5%. It is thus anticipated that leak-off into the bulk of the Bowland Shale will have less effect on the modelled fracture dimensions than other uncertainties, such as those in elastic properties (e.g. in μ and ν). As a result, bulk leak-off is omitted from the present analysis, although leak-off via the 'opened' flat into the seismogenic fault is considered explicitly.

Based on Fig. 4 and given the preceding discussion (and the supporting details in the supplementary material), the fault that adjoins the PH1 well is modelled as a flat at 2580 m depth passing via a zone of uniform curvature (with radius 200 m) into a planar fault with a 75° dip. The strike and dip of this steep part of the fault are chosen as 030° and 75° to match the seismogenic fault plane determined by Westaway (2016a) (Fig. 1). It is noted, however, that there is some question regarding whether the PH1 well track has been correctly positioned on the seismic section in Fig. 4, since the dips of the beds depicted do not match those measured when the well was logged (cf. Kingdon 2016; Westaway 2016d; Table N1). There may thus be uncertainty of >100 m in the positioning of the well relative to the fault (cf. Westaway 2016a), implying similar uncertainty for the model well track relative to the model fault in the depictions of results that follow. As already noted, the wellbore deformation occurred across a ~50 m wide zone of distributed deformation, so cannot be represented precisely by a localized 'flat' at any particular depth.

A representative Mohr circle for PH1 is illustrated in Fig. 8, and demontrates a key point for this locality: the differential stress is so high that only a small increment in fluid pressure above hydrostatic would be sufficient to bring critically-oriented faults to the standard Coulomb condition for shear failure, i.e., for slip in induced earthquakes. However, the fault at Preese Hall differs from this critical orientation by ~20°, so a higher fluid pressure is required to make it slip. Moreover, the relatively simple graphical Mohr technique is best suited to analyzing deformation in planes parallel to principal stresses, rather than deformation in any general plane. The possibility of tensile or shear failure on the 'flat' or any other part of the fault will be investigated assuming this Coulomb condition, adopting the vector-geometry-based approach explained in section 5 of the supplementary material, in lieu of Mohr circle analysis. The Coulomb failure parameter Φ will thus be determined, where $\Phi<0$ denotes stability and $\Phi=0$ shear or tensile instability. The value of Φ in any plane through any point depends on the normal stress σ_n, shear stress τ, fluid pressure p_F, and coefficient of (internal) friction c at the point. Such problems can be solved instead using trigonometry (cf. Bott 1959; Jaeger 1964; Hackston & Rutter 2016), but the vector method adopted here is more straightforward.

Figure 8 here: Preese Hall Mohr circle

Fracking stage 1
Using the physical properties dataset compiled in the supplementary material, an ensemble is considered with μ 10-20 GPa and ν 0.15-0.30. As previously discussed (Fig. 6), fluid injection during fracking stage 1 occurred at (or near) minimum pressure conditions. The resulting predictions (Table N3) range from ~310 to ~390 m for fracture height H and ~8-12 mm for w_o. Under the assumed minimum pressure conditions, C=2, so the predicted fracture length will be will be four times H. The end-members of this ensemble are illustrated in Fig 9, the lower bounds to μ and ν giving the smallest H (Fig. 9(a) and (b)) and vice-versa (Fig. 9(c) and (d)). Thus, the stiffer the rock is (i.e., the higher μ is) the less easily the wall rocks around the fracture can 'bend', so the fracture will be narrower, and thus has to grow taller and longer, to contain a given volume of fluid.

Table N3 here: Modelling results for fracking stage 1
Figure 9 here: stage 1 end-members

Comparison of Fig. 9(a) and (b) with Fig. 9(c) and (d) indicates a range of likely characteristics for all other physically plausible models of PH1 fracking stage 1. The volume of fluid injected was such that any plausible model fracture must have intersected the model 'flat'. The southward component of fracture propagation also means that the fault-fracture intersection will include localities where the fault is beginning to steepen (assuming, of course, that it maintains the same assumed ramp-flat

geometry south of the PH1 well), the intersection being expected to reach somewhat steeper parts of the model fault for the larger fracture in Fig. 9(c) and (d) than for that in Fig. 9(a) and (b). Since fracking stage 1 did not induce any seismicity, it follows that nowhere along these predicted fault-fracture intersections did Φ reach zero. It is now considered how this was possible.

Based on Fig. 6, both P_F and σ_h at the injection point, at ~2667 m depth (Table N1), can be taken as ~43.8 MPa. Given its gradient of ~9.8 kPa m^{-1}, the fluid pressure will have decreased upward to the 2580 m nominal depth of the 'flat', ~87 m shallower, by ~0.9 MPa to ~42.9 MPa. If the 'flat' is assumed precisely horizontal then σ_n across it will equal σ_V, which equation (2) gives as ~58.6 MPa at 2580 m depth. The horizontal model 'flat' is in the plane of two principal stresses, so the shear stress τ on it will be zero. Hence, since $p_F<\sigma_n$, Φ will have been <0 regardless of the value of c for this 'flat' (e.g., Φ will be circa -15.7 MPa × 0.6 or circa -9.4 MPa for c=0.6, a representative value for faults worldwide). Φ will thus also be <0 if the 'flat' has a gentle dip, rather than being horizontal; its plane would no longer be parallel to the horizontal principal stresses but the shear stress across it would be small.

Figure 10 here: Coulomb failure analysis

Given the vertical variations in the principal stresses (equations (1) to (3)) and the geometry of the model fault, Φ can be calculated at any other depth (Fig. 10) for any assumed value of c. Thus, with c=0.6, Φ is predicted to reach zero at 2612 m depth. Reducing c to 0.5 or increasing it to 0.7 would alter this threshold between 2604 and 2623 m. However, the model fault is cut by the model fracture down to 2623 m depth in Fig. 9(b) and slightly deeper, 2635 m, in Fig. 9(d). The modelling thus predicts that across a small patch of the fault near the southern end of the fracture created in stage 1, fluid entered the fault at sufficient pressure to cause slip. However, if this were so, stage 1 would have resulted in induced seismicity, which it did not. Evidently, this model is thus 'not quite right', but small adjustments to many of its parameters (the strike or dip or position of the fault, stress tensor elements or their vertical gradients, elastic moduli, fluid pressure at the injection point, etc.) would be sufficient to preclude this. It follows that the actual induced fracture created by stage 1 must have come very close to bringing part of the actual fault to the condition for shear failure. Presumably, the real fracture developing southward from the injection point only intersected the fault at depths that were shallow enough for Φ<0. Nonetheless, given the sensitivity of this modelling to small changes in many parameters, analyses relating to future operations should use the most accurate data possible.

Fracking stage 2
As Fig. 7 indicates, fluid injection during fracking stage 2 occurred in two parts, with a ~3 hour interval for equipment repair when the well was 'shut in'. As previously discussed, the calculations indicate that during both parts of this process the net pressure was ~15±5 MPa at the depth of injection, p_F having reached ~60 MPa for much of the duration (Fig. 7), unlike the near-minimum-pressure injection during stage 1 (Fig. 6). Prior to the shutdown for repair, ~1200 m^3 of fluid had been injected, comprising the 94 m^3 'mini-frac' plus ~1106 m^3 during the 'main frac'; the former quantity is taken from Table N1 and the latter from digitization of the injection history in Fig. 7(c).

This first part of the stage 2 injection is thus modelled assuming V=1200 m^3 at a ~17 MPa net pressure, based on the BHP of ~60 MPa (Fig. 7(c)), given that σ_h at the injection depth was ~42.8 MPa (equation (3)). The resulting expected fracture height would instead have been ~200 m under minimum pressure conditions, with typical net pressure ~100 m × K or ~0.72 MPa. The 'excess-pressure ratio', M was thus ~17 MPa / ~0.72 MPa or ~24. Furthermore, since the fracture was under high net pressure, roughly equidimensional shape is expected (i.e., C ~0.5), with y_o ~0.02×H.

Figure 11 here: Geometry of the stage 2 fracture at the end of part 1 of the injection

Figure 11 shows the resulting predicted fracture geometry. The smaller dimensions than predicted for stage 1 (Fig. 9) are primarily because the high net pressure requires much greater width. Although this induced fracture was thus much too small to reach any part of the model fault with a significant dip, it was large enough to cut upward into the 'flat'. Given the vertical pressure and stress gradients, σ_V was ~58.58 MPa and p_F ~59.68 MPa at 2580 m depth. So, for c=0.6, Φ=+0.66 MPa on the 'flat', implying that a patch of it had become unstable, the injected fluid thus having sufficient pressure – just – to cause this destabilization. Assuming a horizontal geometry, with this 'flat' in the plane of σ_H and σ_h, thus at zero shear stress (see above), the 'flat' would have failed in effective tension. However, if the 'flat' had nonzero dip then, given the resulting component of shear stress, the 'flat' would thus have failed in 'mixed mode' or 'hybrid mode'. If this process occurred co-seismically, an earthquake involving both tensile and shear components would thus be expected, such events having been documented elsewhere (e.g. Ramsey & Chester 2004; Fojtíková *et al.* 2010; Busetti *et al.* 2014). However, as no seismographs were in place locally at this stage, there are no data that might demonstrate the focal mechanism geometry that could confirm this mode of origin for the first microearthquake of the PH1 sequence.

This initial induced earthquake occurred shortly before the end of this first part of the stage 2 fluid injection, at 10:43 on 31 March 2011 (Fig. 7(b) and (c)); according to Galloway (2012) it had M_L 0.6. Using standard theory (e.g. Westaway & Younger 2014) its seismic moment M_o was ~9×10^9 N m. Faults typically slip with displacement-to-length ratio, k, ~10^{-5} to ~10^{-4}. Again using standard theory (e.g. Westaway & Younger 2014), with a 10 GPa shear modulus, one can estimate ~1.4 mm of slip on a patch of fault with radius ~14 m if k=10^{-4}. If k=10^{-5}, ~0.3 mm of slip on a patch of fault with radius ~30 m can be estimated. Comparison of Fig. 9 with Fig. 11 indicates that the injection points for fracking stages 1 and 2 were ~28 m apart along the section line. Since these sections are oriented at 67° to the induced fracture planes, these planes developed ~28 m × sin(67°) or ~26 m apart. Once a patch of the 'flat' of radius greater than this value had opened (or slipped in shear, or failed in 'hybrid' mode) as a result of the first induced earthquake, fluid injected through the stage 2 well perforations would have been free to flow into the fracture already created during stage 1. From this point onward, the development of the fracture network is less readily predictable. Nonetheless, some (arguably, most; see below) of the fluid subsequently injected is expected to have flowed into the fracture already created during stage 1. To explore this possibility, it is noted from Fig. 7(c) that by the time of the first induced earthquake ~982 m^3 of fluid had been injected during the stage 2 'main frac', plus the 94 m^3 from the 'mini-frac', giving a total of ~1076 m^3. Fig. 12 illustrates the geometry of the stage 2 fracture thus predicted at this time.

Figure 12 here: Geometry of the stage 2 fracture at the time of the first induced earthquake

As noted above, the development of the fracture network later during fracking stage 2 is less readily predictable. Nonetheless, at the time when the stage 1 and stage 2 fractures became interconnected, that from stage 1 was larger. The stress intensity at its tip was greater, making it more readily able to grow, from which it may be inferred that most of the subsequent fluid injection contributed to enlarging it, rather than enlarging the fracture initiated during stage 2. Nonetheless, some of the injected fluid might instead have enlarged the stage 2 fracture and, given the high net pressure of this fluid (Fig. 7(c)), with Φ ~0 along the 'flat', some of it will have contributed to 'opening' more of this 'flat'. One may nonetheless consider the hypothetical end member case where all the fluid subsequently injected during stage 2 ended up in the fracture created during stage 1. If so, the volume of this fracture at the end of stage 2 can be estimated as the total volume injected during stages 1 and 2 minus ~1076 m^3 (see above), or ~3232 m^3. Furthermore, when the well was 'shut in' at the end of stage 2 the net pressure (at the stage 2 injection point) is predicted

to have gradually decreased towards zero (Fig. 7(c)). Given the interconnection between the stage 1 and stage 2 fractures, the same pressure is expected at the same depth in the stage 1 fracture, with the pressure at the somewhat greater depth of injection for stage 1 also close to σ_h at this depth (Fig. 6(c)). The dimensions of the stage 1 fracture at this time can therefore be estimated assuming the minimum pressure configuration for a volume of ~3232 m^3. Table N4 lists these dimensions for different μ and ν values; Figure 13 depicts the predicted end members.

Table N4 here: Modelling results for the stage 1 fracture at the end of fracking stage 2
Figure 13 here: stage 2 solutions

Comparison of Fig. 13 with Fig. 9 indicates that, regardless of choices for μ and ν, or, indeed, V, the stage 1 fracture grew significantly as a result of the additional fluid injected into it during stage 2. Given the prediction that at the end of stage 1 this fracture was already close to intersecting the steep part of the fault, it is evident that the enlargement during stage 2 resulted in such an intersection developing. This fault-fracture intersection is predicted to have reached 2635 m depth in Fig. 13 (b), increasing to 2641 m in Fig. 13 (d) in which the fracture is larger. At both these depths Φ is predicted (from the ambient stress state and fluid pressure) to have been well above 0 (Fig. 10), indicating that shear failure would be expected. Indeed, shear failure would have occurred sometime earlier, when during the course of its growth the fracture reached the fault at a somewhat shallower depth but with the fluid in it at a higher pressure (given the progressive pressure decline after 'shut in'; cf. Fig. 7(c)).

Given the above reasoning and the seismicity depicted in Fig. 7(b) and (c), it is inferred that the first induced earthquake on the steep part of the fault was that depicted at 17:31 on 31 March, which had M_L=0.5 (Galloway, 2012), at a late stage during the pressure decline after 'shut in'. It is suggested that the sequence of later earthquakes, culminating in the largest, at 02:34 on 1 April (M_L=2.3; Galloway 2012), likewise occurred on patches of the steep part of the fault in close proximity. Slip during each event presumably enlarged the patch of fault that fluid could enter and stressed patches of the fault adjoining that which slipped (a process analysed in some detail by others, e.g. Rutqvist *et al*. 2013, analysis that is thus omitted here), thereby facilitating slip in the next earthquake, until the coupled system stabilized with Φ<0 everywhere on the fault. The other earthquakes depicted in Fig. 7(c) had origin times between 14:17 and 16:03 on 31 March, with M_L between 0.2 and 1.4, the largest individual event (M_L=1.4) having occurred at 14:19 (Galloway 2012). These events all occurred while the fracture network was under high net pressure during the second part of the stage 2 injection (Fig. 7(c)). This high net pressure would have meant that at the time the stage 1 fracture was enlarging mainly by widening, rather than developing increased height, so would not yet have reached the fault. It is thus inferred that these events occurred on the 'flat' and 'opened' more of it by tensile and/or hybrid failure. The stage 1 induced fracture could only reach the steep part of the fault later, as a result of the pressure reduction following 'shut-in', when its shape is predicted have changed, as it evolved to become narrower but higher and longer as a result of the stress redistribution accompanying the pressure reduction. Using the same calculation procedure as before, the M_L 1.4 event had M_o ~1.4×10^{11} N m and involved a patch of fault with radius ~36 m slipping by ~3.6 mm if k=10^{-4}, or with radius ~76 m slipping by ~0.8 mm if k=10^{-5}. This event would thus have 'opened' the 'flat' over a sufficient area to include points in the planes of the fractures that developed during the later fracking stages 3 and 4 (Figs 13(b) and (d); see, also, below). The M_L 2.3 event had M_o ~3.2×10^{12} N m, and involved a patch of fault with radius ~100 m slipping by ~10 mm if k=10^{-4}, or with radius ~220 m slipping by ~2.2 mm if k=10^{-5} (cf. Westaway & Younger 2014). The expected location of this rupture, at the fault-fracture intersection, is ~700 m SSE of the PH1 wellhead (Figs 13(a) and (c)), near the location determined by Westaway (2016a) from arrival times of seismic waves (Fig. 1). Since the distance between this hypocentre and the wellbore exceeds the dimensions of the patch of fault that slipped, it is inferred that the wellbore

deformation (Fig. 4) was not caused directly by the co-seismic slip. It was evidently a consequence of aseismic deformation in the surroundings to the patch of fault that slipped co-seismically, thus affecting the 'flat' even though the largest earthquake occurred on the steep part of the fault.

The internal consistency of this analysis may be tested by comparing Westaway's (2016a) focal mechanism for the induced seismicity with the optimum orientation for cosesimic slip predicted from the stress state. Westaway's (2016a) solution has strike 030°, dip 75°, and rake -20°, with a P-axis plunging at 24.62° towards azimuth 346.96° or N14.04°W and a T-axis plunging at 2.90° towards 078.29° or N78.29°E. Its null axis plunges at 65.19° towards 174.58° or S5.42°E and its slip vector plunges at 19.29° towards 035.38° or N35.38°E. Using the method explained in section 5 of the supplementary material, and with the vertical variations in principal stresses given by equations (1) to (3) (i.e., neglecting any changes to the state of stress caused by preceding earthquakes), the results listed in Table N5 are calculated for induced earthquakes at a range of plausible assumed depths. This comparison reveals a high degree of consistency, confirming that the model scenario is internally consistent. The few degrees of mismatch evidently mean that the orientation of this focal mechanism and/or the numerical values used to describe the stress state are slightly 'out' relative to one another. Once again, the lack of definitive data, which might have enabled this mismatch to be reconciled, is noted. It is also noted in passing that none of the other published focal mechanism solutions for the PH1 induced seismicity comes close to consistency with the orientation predicted from the state of stress. Indeed, as Westaway (2016a) pointed out, some of them are inconsistent with the basic constraint (cf. McKenzie 1969) that the maximum and minimum principal stresses must lie, respectively, within dilatational and compressional quadrants of a focal mechanism.

Table N5 here: focal mechanism orientations from the stress analysis

Fracking stages 3, 4 and 5
No attempt is made here to analyse in detail fracking stages 3, 4 or 5; data analogous to that in Figs 6(a) and 7(a) has been unavailable (the pressure data series for these fracking stages depicted by de Pater & Pellicer 2011 are not amenable to digitization). It is nonetheless summarized here how activity during these stages is inferred to have interacted with the fracture network created during stages 1 and 2. The stage 3 injection is depicted in Fig. 13 at a nominal depth of 2541 m (Table N1). Although this is ~40 m above the idealized depiction of the 'flat', it adjoins the zone of wellbore deformation and, given the likelihood of some downward propagation of the stage 3 fracture, it is to be expected that this fracture intersected the 'flat'. This provides a natural explanation for one curious characteristic of stage 3, that the volume of flowback was more than double the volume of fluid injected (Table N1). It is suggested that by intersecting the patch of the 'flat' that had been 'opened' during stage 2, the stage 3 fracture effectively 'tapped' some of the fluid that had been injected during stages 1 and 2 and remained within the interconnected fracture network thus created. Indeed, the observation that flowback occurred even before the stage 3 'mini-frac' took place (Table N1), presumably immediately after the well casing was perforated, suggests that the stage 3 injection point was interconnected with the previously 'opened' patch of the 'flat'.

de Pater & Baisch (2011) illustrated the injection procedure during stage 4 in their Fig. 27, reporting the WHP after conditions stabilized following shut-in after this injection as ~19.0 MPa, giving a BHP of ~43.1 MPa (Table N1). This injection began circa 12:30 on 27 May 2011 when their calculated BHP was ~7000 psi (~48.3 MPa). The BHP rose gradually thereafter, reaching ~7600 psi (~52.4 MPa) as injection ended circa 14:40. The first induced earthquake, of M_L -1.0 (the lower detection threshold being due to local seismograph stations operating; cf. Fig. 1) occurred at 13:56 (Galloway 2012), when the BHP was ~7400 psi or ~51.0 MPa (de Pater & Baisch 2011). BHP then gradually declined to ~6300 psi (~43.4 MPa) by circa 18:40, as the well was 'shut in' and flowback occurred. Induced seismicity continued during the latter stages of injection and during 'shut in', culminating in the

second largest event in the sequence, at 00:48 on 27 May, of M_L 1.5 (Galloway 2012). All these values for BHP are rather higher than σ_h at the ~2456 m depth (TVD) of injection, which equation (3) gives as ~40.1 MPa. The net pressure in the hydraulic fracture network during stage 4 was thus significant, although not as high as during stage 2.

Figure 14 here: Analysis of stage 4

The first induced earthquake during stage 4 occurred after roughly three quarters of the 'main frac' injection, estimated as ~1200 m^3 (cf. Table N1). Adding the 80 m^3 from the preceding 'mini-frac' gives a total of ~1280 m^3. Figure 14 shows the predicted geometry of the stage 4 induced fracture at this time, calculated for μ=10 GPa and ν=0.15, the smallest values considered. It is thus probable that the downward component of fracture growth, resulting from the net pressure, had reached 2535 m depth by the time of this earthquake. With μ=20 GPa and ν=0.30, the largest values considered, the fracture is predicted to have reached 2556 m. Although it thus fell short of the nominal 2580 m depth of the 'flat', it may well have reached the actual zone of wellbore deformation below ~2550 m (TVD). It is thus inferred that the first induced earthquake, at 13:56 on 27 May 2011, marked when the growing fracture breached into this subhorizontal zone. As already discussed, σ_V at the nominal 2580 m depth of the 'flat' was ~58.6 MPa (equation (2)). The pressure at this depth inside the induced fracture can be estimated as the ~51.0 MPa BHP plus the effect of the hydrostatic pressure gradient over the 80 m of extra depth, or ~51.8 MPa. The 'flat' is again assumed horizontal so, as before, σ_n=σ_V and τ=0; Φ will be <0, the fluid pressure inside the fracture having been too low relative to σ_V to 'open' any part of the 'flat'. It may be recalled, however, that some of the induced seismicity during stage 2 was of sufficient magnitude to have broadened the 'opened' patch of the 'flat' into the vertical plane in which the stage 4 fracture later developed. It is thus inferred that, rather than 'opening' any patch of the 'flat', the first induced earthquake of stage 4 occurred at the instant when the stage 4 fracture breached into this 'flat' from above. If so, this event is expected to have had a tensile or 'hybrid' focal mechanism consistent with creation of a vertical fracture plane oriented perpendicular to σ_h.

Once the stage 4 fracture and the 'flat' became hydraulically connected, the remaining fluid injected during stage 4 would have been able to flow freely via the 'opened' part of the 'flat' into the stage 1 fracture and thus into the steep patch of the fault that had already been breached. From the earlier analysis (Fig. 10), a fluid pressure of ~60.0 MPa was required at the ~2640 m depth where the steep part of the fault was breached, to initiate the sequence of induced earthquakes on it that accompanied and followed stage 2. However, the fluid pressure during stage 4 could not have been as high as this: allowing for the hydrostatic pressure gradient between ~2456 m and ~2640 m depths, it would have been ~54.2 MPa at the end of stage 4 injection (i.e., ~1.8 MPa plus the aforementioned ~52.4 MPa), gradually decreasing to ~44.9 MPa after shut-in. However, in accordance with earlier discussion, the induced seismicity that followed stage 2 would have changed the state of stress in the vicinity of this 'breached' part of the fault. It would have de-stressed the patches of it that had already slipped, thereby increasing the differential stress on adjoining patches of this fault. It is thus inferred that the fluid pressure in these 're-stressed' localities was high enough to induce seismicity given the state of stress at the time, from which it follows that the rest of the seismicity that accompanied or followed the stage 4 injection occurred on steep patches of the fault adjacent to that associated with stage 2.

The stage 5 injection point was so much shallower (Table N1) that downward growth of the resulting induced fracture to the 'flat' is not anticipated. It is thus inferred that the induced seismicity during and after stage 5 occurred because of continued changes in the state of stress of the steep part of the fault (de-stressing patches that had already slipped and re-stressing neighbouring patches; cf. Rutqvist et al., 2013) that had been breached by the fracture network created beforehand. This

includes the event (M_L -0.2) at 08:12 on 2 August 2011 (Galloway 2012). This latter event is significant primarily because at the time the monitoring network was at its best, with four seismographs deployed locally (Fig. 1). Analysis of this particular event has been essential for determining the focal mechanism of earthquakes on the steep patch of the fault (e.g. Westaway 2016a; Fig. 1). This has followed the realization (e.g. de Pater & Baisch 2011) that the seismograms recorded by particular seismographs for different earthquakes (such as those on 27 May and 2 August) are very similar, implying that they occurred in close proximity with the same focal mechanism (see, also, below).

Discussion

To facilitate discussion, the sequence of key events inferred during the PH1 fracking is illustrated in Fig. 15. The essential element underpinning this conceptual model is the realization that the 'flat' at ~2580 m depth was 'opened' initially by the high net pressure during stage 2 of the fracking, and thereafter acted as an interconnection between the induced fractures created during the different fracking stages. Thus, the fracture from stage 1 developed as expected, the fluid having been close to minimum pressure conditions at this time. Although this fracture cut the 'flat' it was not under sufficient pressure to cause tensile failure, i.e., to 'open' a patch of the 'flat'. However, during stage 2 fluid was injected at a significant net pressure, estimated as ~17 MPa. The fluid pressure was now high enough, just, to 'open' a patch of the 'flat', allowing fluid to leak via this 'flat' into the fracture that had been created during stage 1. The latter fracture thus continued to grow, eventually breaching into the steep part of the fault ~700 m SSE of the wellhead and inducing the largest earthquake of this sequence (M_L 2.3). The fractures created during stages 3 and 4 likewise became interconnected with this pre-existing fracture network, the second largest earthquake (M_L 1.5), following stage 4, likewise involving slip on a steep patch of this fault. The model is consistent with the available data and makes predictions regarding other aspects, such as the co-occurrence of different populations of tensile or 'hybrid' induced earthquakes and conventional shearing earthquakes during the sequence. This aspect would be testable had local microseismic monitoring been in place from the outset of the project.

Figure 15 here: conceptual model

There has been much discussion of potential contamination arising from failure of containment of fracking fluid, for example as a result of well integrity issues (e.g. Davies *et al*. 2014; Thorogood & Younger 2015) or as a consequence of fluid migration to shallow depths (e.g. Jackson *et al*. 2013; Birdsell *et al*. 2015). The PH1 case study demonstrates another form of containment failure, whereby fracking fluid migrated into unexpected places as a result of the unforeseen development of interconnections between induced fractures (Fig. 15). This creation of a complex interconnected fracture network resembles what can occur in former mine workings (e.g. Younger 1993; Johnson & Younger 2002; Westaway & Younger 2016). It also bears upon the general issue of where fracking fluid 'goes' following injection (e.g. O'Malley *et al*. 2016).

The conceptual model in Fig. 15 explains a number of hitherto puzzling aspects of the PH1 case study. First, it provides a natural explanation for the wellbore deformation that accompanied the largest of the induced earthquakes, given the geometrical relation between the steep part of the fault on which the largest earthquakes occurred and the 'flat' where the aseismic wellbore deformation was located. This supersedes the previous suggestion (e,g. de Pater & Baisch 2011) that amounted to regarding the co-occurrence of wellbore deformation and induced seismicity as a coincidence. Clarke (2016) has claimed that the notion that this wellbore deformation is mechanically linked to the coseismic slip is 'counter to [the] currently held and accepted understanding of such observations and mechanical causes'; the present analysis strongly suggests otherwise. Second, the geometrical relationship between the induced fracturing and the steep part

of the fault provides a natural explanation for why the induced seismicity was concentrated SSE of the PH1 drilling site, ~700 m away, where Westaway (2016a) located the best documented earthquake in the sequence, that of 2 August 2011 (M_L -0.2). Clarke (2016) has since argued that these co-ordinates do not differ significantly from the Clarke *et al*. (2014) epicentre (also indicated in Fig. 1) when the uncertainties in location procedures are taken into account. However, it now seems evident that a location southward from the PH1 site is to be expected, given the geomechanics, rather than being something to be explained away as an artefact of location uncertainty or error as Clarke (2016) has claimed. Third, the model provides a natural explanation for why the seismograms of different PH1 earthquakes, recorded at different permanent and temporary stations, are so similar, implying that the studied earthquakes all occurred very close together, an observation that was noted by de Pater & Baisch (2011) and has since been discussed by others, including Westaway (2016a). One would not have expected *a priori* this to be so, because it would have been expected at the outset (before it was realized that the induced fractures became interconnected), given the deviation of the well, that the fractures from different fracking stages developed *en echelon*, so an earthquake associated with stage 4 (such as the 27 May 00:48 event) must inevitably have occurred some distance away from one associated with stage 2 (such as the 1 April 02:34 'mainshock'). As Fig. 15 indicates, the close proximity of these hypocentres can now be explained as a consequence of the interconnection of the fractures from the different stages, with both these events having occurred adjacent to the point where the stage 1 fracture became enlarged during stage 2 and thus intersected the steep part of the fault. Fourth, as already noted, the excess of flowback over injection during stage 3 is also explicable as a consequence of the development of an interconnection between the stage 3 fracture and the fracture network created during stages 1 and 2. Finally, as will be discussed in more detail below, the model can account in a natural way for the occurrence of the two largest earthquakes during 'shut-in', rather than during injection: the 1 April 02:34 'mainshock' ~10 hours after the start of 'shut in' following stage 2 and the 27 May 00:48 event ~10 hours after the start of 'shut in' following stage 4 (e.g. de Pater & Baisch 2011), given that during both these phases the injected fluid was under significant net pressure. Theoreticians have tried to explain such time delays in terms of exotic fluid dynamical phenomena (e.g., McClure, 2015). It is now suggested that these delays are explicable as consequences of predictable changes in the size and/or shape of the induced fracture network in response to progressive depressurization during 'shut in'.

Implications for regulation
Following a recommendation by Green *et al*. (2012), in December 2013 the UK authorities issued regulations governing 'fracking', which include specifying the 'red traffic light' threshold of M_L 0.5 for suspension of operations (DECC 2013). Other jurisdictions also use magnitude-based 'red traffic light' thresholds but set much higher. For example, in 2015 the Canadian province of Alberta introduced a threshold of M_L 4.0 (AER 2015), along with a 'yellow traffic light' threshold of M_L 2.0, above which the regulator must be notified but fracking can continue. Operations were thus shut down following the M_L 4.8 Fox Creek, Alberta, earthquake of 12 January 2016 (e.g. CBC 2016), being allowed to resume some months later (e.g. Kent 2016). It would clearly make no sense to adopt a 'red traffic light' threshold as low as M_L 0.5 if the aim were to mitigate the nuisance caused by earthquakes as small as this, since such minor events will cause weaker ground vibrations than many other everyday forms of environmental nuisance and might well not even be felt (Westaway & Younger 2014). On the contrary, the basis of the Green *et al*. (2012) proposal is that a M_L 0.5 microearthquake might be considered a precursor of a larger event, so by shutting down activity the subsequent larger event might be prevented. For example, the argument goes, had this regulation been in force in 2011 the stage 2 injection would have been shut down following the event at 10:43 on 31 March (M_L 0.6), so the 'mainshock' (M_L 2.3) at 02:34 on 1 April would not have occurred.

An essential element hitherto lacking from this regulation is any basis in terms of a cause-and-effect connection between the 'precursory' M_L 0.6 event and the subsequent M_L 2.3 earthquake, which would allow the underlying rationale to be tested. The conceptual model in Fig. 15 now provides the basis for such an investigation. Thus, had the stage 2 injection stopped at 10:43 on 31 March 2011, the volume injected during this stage would have been ~1076 m^3 (see above). If all this volume had joined the 1969 m^3 injected during stage 1, making a total of ~3045 m^3, in the stage 1 fracture, the dimensions of this fracture would have been slightly smaller than those depicted in Fig. 13. If only part of this been ~1076 m^3 volume had entered the stage 1 fracture, then its dimensions would evidently have been slightly smaller still, but still larger than those depicted in Fig. 9. However, given the narrow margins involved in this modelling, it is impossible to say, in either of these circumstances, whether the stage 1 fracture would or would not have grown sufficiently to intersect a steep patch of the fault and induce seismicity there. The possibility thus cannot be ruled out that, even if injection ceased at 10:43 on 31 March 2011, this fracture would have grown sufficiently for this induced seismicity still to have occurred. This realization makes the red traffic light threshold adopted (notwithstanding its low magnitude threshold) of no guaranteed value for mitigating this particular instance of induced seismicity – thus making it of no guaranteed value in general. Fortunately, the DECC (2013) document states that the regulations will be 'subject to review'. It is hoped that the present paper may provide guidance towards more appropriate regulation, to avoid unfairly disadvantaging the new shale gas industry. As Westaway & Younger (2014) pointed out, an existing – and uncontroversial – framework for regulating ground vibration by peak ground velocity has been in place in the UK for decades and could be applied as it stands to induced seismicity, rather than attempting to regulate this form of ground vibration in a way that is inconsistent with others.

Unlike in 2011, microseismic monitoring using a local seismograph network is now a UK regulatory requirement at fracking sites. Had such monitoring been in place in 2011, the locations and focal mechanisms could have been determined for the M_L 0.6 microearthquake at 10:43 on 31 March and the associated activity, including other events that might have occurred around the same time but were below the detection threshold of the permanent seismograph network operating then (Fig. 1). It would thus have been possible to monitor whether the various effects predicted from the conceptual model indeed occurred, including the initial 'opening' of a patch of the 'flat' above the stage 2 injection point (Fig. 15(b)) and the subsequent sideways migration of the seismicity across the 'flat' (Fig. 15(c)). Such observations would have immediately alerted the well operator that something significant had 'gone wrong', so injection could have been terminated. However, as already noted, it is a moot point whether this would have prevented the subsequent M_L 2.3 earthquake. It would nonetheless have been possible to base the decision to shut down injection on a rigorous criterion (i.e. because something unexpected was happening), rather than on the exceedance of an arbitrary magnitude limit (i.e. M_L 0.6 exceeding the M_L 0.5 'red traffic light' threshold).

The present analysis indicates that high net fluid pressure during stage 2 and, to a lesser extent, during stage 4 was the essential cause of the failure of the PH1 project. The issue of regulation of pressure of fracking fluid thus warrants consideration, this parameter being currently unregulated In the UK. The use of excessive fluid pressure during stage 2 appears to have resulted from incorrect analysis (using industry standard software) of the preceding 'mini-frac', leading to overestimation of σ_h at the injection point, thus creating the misapprehension that the high pressure was necessary to hold any induced fracture open. This mis-calculation might have been picked up through the realisation that the analysis of the stage 2 'mini-frac' predicted much larger σ_h than that for stage 1, even though the depth was ~50 m shallower (Table 1). The high net pressure during stage 2 was sufficient to 'open' a patch of the 'flat' above the injection point (Fig. 15(b)); the subsequent difficulties all followed indirectly from this occurrence. Furthermore, had the fluid not previously

been under high net pressure during stage 2, the calculations indicate that no unforeseen consequences would have arisen as a result of the lower net pressure during stage 4. The calculations nonetheless indicate that a narrow margin was involved. Although the fracking fluid was injected at a net pressure of ~17 MPa during stage 2, it is predicted that the Coulomb failure criterion was exceeded by <1 MPa, implying that had the net pressure been ~15 MPa rather than ~17 MPa the induced seismicity would not have occurred. Nonetheless, the ultimate causative factor would seem to have been the uncritical acceptance of results output by the 'mini-frac' analysis software, even though these made no sense.

The idea of mitigating induced seismicity by regulating the pressure of injected fluid is of course not new. It was first demonstrated by Raleigh *et al*. (1976) at Rangely, Colorado, where it was found (and explained using Coulomb failure analysis) that seismicity caused by fluid injection for secondary oil recovery could effectively be 'switched on or off' by pressurizing a reservoir above or below a threshold of 25.7 MPa, 9.5 MPa above the pre-existing fluid pressure. However, the importance of fluid pressure as a causal factor in induced seismicity has not been fully recognized in more recent works. For example, in the Weingarten *et al*. (2015) study of the recent dramatic increase in induced seismicity in the U.S.A., mostly associated with fluid injection for wastewater disposal, no causative effect of fluid pressure could be identified; these authors identified an effect of injection rate and recommended regulating this parameter. However, Weingarten *et al*. (2015) noted that in most U.S. wastewater disposal wells the WHP is no greater than 500 psi or ~3.4 MPa, implying that the associated fluid pressure changes are likely to be comparable in magnitude and thus probably too small to induce seismicity. It should be emphasized that the fluid pressure changes anticipated during fracking for shale gas, as well as for hydraulic fracturing for geothermal purposes, are far greater than the above-mentioned value for wastewater disposal; the resulting different effect of fluid pressure on induced seismicity is thus unsurprising. McGarr *et al*. (2015) encouraged well operators to make public fluid pressure data, to facilitate conceptual model development for induced seismicity. The present study supports this view; without detailed consideration of fluid pressure data (cf. Figs. 6 and 7) the PH1 case study would have remained poorly-understood.

The high net pressure during stage 2 had two adverse consequences, the first having been to 'open' a patch of the 'flat'. In other shale plays, for example the Barnett Shale of Texas, fracking routinely 'opens' pre-existing fractures as well as creating new fractures (e.g. Gale *et al*. 2007), which is considered a 'bonus' to operators as it increases the overall fracture surface from which gas may be extracted. However, for PH1, the consequences of 'opening' the 'flat' were most definitely not beneficial. Westaway (2016a) has suggested that the difference in behaviour might relate to the effect of high $\Delta\sigma$ on the size-distribution of the resulting induced earthquakes (see, also, below). The second adverse consequence was that the fracture is predicted to have continued to grow after the end of injection, while the well was 'shut in', a consequence of the decline in fluid pressure at this stage. It is thus suggested that careful control and monitoring of fracking fluid pressure should be a future regulatory requirement, the aim being to frack under 'minimum pressure' conditions wherever possible, not under sustained high net pressure. If higher pressure is needed (e.g., to fracture through a particularly strong layer of rock), it should be pulsed, not steadily applied, this being a recognized way of mitigating induced seismicity during hydraulic fracturing for geothermal development (e.g. Zimmermann *et al*. 2010). It is also noted that during the stage 1 injection the well was kept close to zero net pressure conditions, but the BHP rose abruptly when injection ended and the well was 'shut in' (Fig. 6). By reducing the injection rate gradually, rather than abruptly, with a corresponding variation in WHP, it should be possible to avoid such a 'pressure spike' and any adverse consequences that might result. Regulation of net pressure and/or abrupt pressure variations has previously been proposed as a measure to mitigate induced seismicity caused by fluid injection in geothermal projects (e.g. Majer *et al*. 2007; Häring *et al*. 2008; Deichmann & Giardini 2009). Such regulation might include specifying workflows for determining fluid pressure, including

procedures for checking unexpected results, before proceeding farther. It is also evident from the foregoing text that the absence of downhole measurements of fluid pressure (and the resulting need to calculate BHP from WHP, thereby introducing uncertainties into the analysis) is a significant cause of uncertainty at PH1. Downhole pressure sensors and loggers are readily available (e.g. Schlumberger 2016); their use could be made another regulatory requirement.

Conclusions

By integrating multiple datasets with relevant theory, covering fluid injection and fracturing, a conceptual model for the PH1 fracture development and induced seismicity has been developed. Key features of this model include the steep fault that has been recognized adjoining this well, which slipped in the largest induced earthquakes, and the presence of a weak, subhorizontal 'flat' within the depth range of the fluid injection, which was 'opened' by this injection. Taking account of the geometry of the fault and the orientation of the local stress field, the model predicts that this induced seismicity was concentrated ~700 m SSE of the PH1 wellhead, in roughly the place where Westaway (2016a) established that this activity was located. A further key observation, critical to explaining the subsequent sequence of events, is the recognition that the fluid injection during stage 2 of the fracking was under a net pressure of ~17 MPa. As a result, this fluid injection 'opened' a patch of the 'flat', establishing a hydraulic connection with the fracture network created during stage 1. Continued fluid injection thus enlarged the latter fracture network, which ultimately extended southward far enough to intersect the steep part of the fault and induce the largest earthquake of the sequence there. Subsequent fluid injection during fracking stages 3 and 4 added to the complexity of this interconnected fracture network, in part because the injection during stage 4 was again under significant net pressure. This model can account for many aspects of the PH1 record, notably how it was possible for the induced fracture network to intersect the seismogenic fault so far from the injection point: the interconnection between fractures meant that the stage 1 fracture continued to grow during stage 2, rather than two separate smaller fractures, isolated from each other, being created. Calculations indicate that, despite the substantial net pressure, the project only 'went wrong' by a narrow margin. Had the net pressure been ~15 MPa rather than ~17 MPa the induced seismicity would not have occurred. The model also predicts that some of the smaller induced earthquakes had tensile or 'hybrid' focal mechanisms; this would have been testable had any seismographs been deployed locally to monitor the activity. From the point of view of the geomechanics, it is immaterial whether the model 'flat' is in reality a subhorizontal updip continuation of the steep seismogenic fault, or a zone of rock that has been deformed and weakened for other reasons, for example due to a Carboniferous-era palaeo-landslide, or simply a zone of non-cohesive bedding planes. The analysis emphasizes the undesirability of injecting fracking fluid under high net pressure in this region, where flat patches of fault and/or subhorizontal structural discontinuities are present.

References

ADACHI, J., SIEBRITS, E., PEIRCE, A. & DESROCHES J. 2007. Computer simulation of hydraulic fractures. *International Journal of Rock Mechanics & Mining Sciences*, **44**, 739–757.

AER 2015. *AER responding to seismic events in the Fox Creek area*. Alberta Energy Regulator, Calgary, Alberta. Available online: https://aer.ca/about-aer/media-centre/news-releases/news-release-2015-02-19 (accessed 21 August 2016)

ANDREWS, I. J. 2013. *The Carboniferous Bowland Shale gas study: geology and resource estimation*. British Geological Survey for Department of Energy and Climate Change, London, 64 pp.

BAISCH, S. & VÖRÖS, R. 2011. *Geomechanical study of Blackpool seismicity*. Report for Cuadrilla Resources, 58 pp. Available online: http://www.cuadrillaresources.com/wp-content/uploads/2012/02/Geomechanical-Study-Appendix-2-2.11.2011.pdf (accessed 30 November 2016)

BAKER HUGHES 2011. *Wellbore failure analysis and geomechanical modelling in the Bowland Shales, Blackpool, UK: preliminary technical report*. Baker Hughes Incorporated, Houston, Texas, 53 pp. Available online: http://www.cuadrillaresources.com/wp-content/uploads/2012/02/Geomechanical-Study-Appendix-1-2.11.2011.pdf (accessed 10 May 2015)

BARREE, R. D., COX, S. A., GILBERT, J. V. & DOBSON, M. L. 2005. Closing the gap: fracture half length from design, buildup, and production analysis. Society of Petroleum Engineers document SPE-84491-PA. *SPE Production & Facilities*, **20** (4), 12 pp. doi: http://dx.doi.org/10.2118/84491-PA

BEHRMANN, L., BROOKS, J.E., FARRANT, S., FAYARD, A., VENKITARAMAN, A., BROWN, A., MICHEL, C., NOORDERMEYER, A., SMITH, P. & UNDERDOWN, D. 2000. Perforating practices that optimize productivity. *Oilfield Review*, **Spring 2000**, 52-74.

BIRDSELL, D. T., RAJARAM, H., DEMPSEY, D. & VISWANATHAN, H. S. 2015. Hydraulic fracturing fluid migration in the subsurface: A review and expanded modeling results. *Water Resources Research*, **51**, 7159–7188.

BLÖCHER, G., REINSCH, T., HENNINGES, J., MILSCH, H., REGENSPURG, S., KUMMEROW, J., FRANCKE, H., KRANZ, S., SAADAT, A., ZIMMERMANN, G. & HUENGES, E. 2016. Hydraulic history and current state of the deep geothermal reservoir Groß Schönebeck. *Geothermics*, **63**, 27–43.

BOTT, M.H.P. 1959. The mechanics of oblique slip faulting. *Geological Magazine*, **96**, 109–117.

BRADY, B., ELBEL, J., MACK, M., MORALES, H., NOLTE, K. & POE, B. 1992. Cracking rock: progress in fracture treatment design. *Oilfield Review*, **October 1992**, 4-17.

CBC 2016. *Fox Creek fracking operation closed indefinitely after earthquake*. Canadian Broadcasting Corporation, Edmonton, Alberta. Available online: http://www.cbc.ca/news/canada/edmonton/fox-creek-fracking-operation-closed-indefinitely-after-earthquake-1.3400605 (accessed 26 August 2016)

CLARKE, H. 2016. *Reply to "Hydraulic fracturing in thick shale basins: problems in identifying faults in the Bowland and Weald Basins, UK" by D.K. Smythe*. Interactive Discussion item SC9, 7 pp. Available online: http://www.solid-earth-discuss.net/se-2015-134/discussion (accessed 3 March 2016)

CLARKE, H., EISNER, L., STYLES, P. & TURNER, P. 2014. Felt seismicity associated with shale gas hydraulic fracturing: The first documented example in Europe. *Geophysical Research Letters*, **41**, 8308–8314.

COSGROVE, J. W. 2001. Hydraulic fracturing during the formation and deformation of a basin: A factor in the dewatering of low-permeability sediments. *AAPG Bulletin*, **85**, 737–748.

CUADRILLA 2014. *Temporary Shale Gas Exploration; Preston New Road, Lancashire; Environmental Statement, Appendix L – Induced Seismicity*. Cuadrilla Bowland Ltd., Lichfield, 140 pp. Available online: http://planningregister.lancashire.gov.uk/Attachments/6586/PNR_ES_Vol2_Appndx L_Induced Seismicity.pdf (accessed 9.03.15).

DAVIES, R. J., ALMOND, S., WARD, R. S., JACKSON, R. B., ADAMS, C., WORRALL, F., HERRINGSHAW, L. G., GLUYAS, J. G. & WHITEHEAD, M. A. 2014. Oil and gas wells and their integrity: Implications for shale and unconventional resource exploitation. *Marine and Petroleum Geology*, **56**, 239–254.

DAVIES, R., FOULGER, G., BINDLEY, A. & STYLES, P. 2013. Induced seismicity and hydraulic fracturing for the recovery of hydrocarbons. *Marine and Petroleum Geology*, **45**, 171-185.

DAVIS, S. D. & FROHLICH, C. 1993. Did (or will) fluid injection cause earthquakes? Criteria for a rational assessment. *Seismological Research Letters*, **64**, 207–224.

DE PATER, C. J. & BAISCH, S. 2011. *Geomechanical study of Bowland Shale seismicity: synthesis report*. Cuadrilla Resources Ltd., Lichfield, 71 pp. Available online: http://www.rijksoverheid.nl/bestanden/documenten-en-publicaties/rapporten/2011/11/04/rapport-geomechanical-study-of-bowland-shale-seismicity/rapport-geomechanical-study-of-bowland-shale-seismicity.pdf (accessed 5 August 2015)

DE PATER, C. J. & PELLICER, M. 2011. *Geomechanical Study of Bowland Shale Seismicity – Fracture Geometry and Injection Mechanism: Final Report for Cuadrilla Resources*. StrataGen Delft BV, Delft, The Netherlands, 48 pp. Available online: http://www.cuadrillaresources.com/wp-content/uploads/2012/02/Geomechanical-Study-Appendix-4-2.11.2011.pdf (accessed 31 October 2016)

DECC 2013. *Onshore oil and gas exploration in the UK: regulation and best practice*. Department of Energy and Climate Change, 49 pp. Available online: https://www.gov.uk/government/uploads/system/uploads/attachment_data/file/265988/Onshore_UK_oil_and_gas_exploration_England_Dec13_contents.pdf (accessed 10 May 2014)

DEICHMANN, N. & GIARDINI, D. 2009. Earthquakes induced by the stimulation of an enhanced geothermal system below Basel (Switzerland). *Seismological Research Letters*, **80**, 784–798.

DETOURNAY, E. 2016. Mechanics of hydraulic fractures. *Annual Review of Fluid Mechanics*, **48**, 311–339.

DUSSEAULT, M. B., BRUNO, M. S. & BARRERA, J. 2001. Casing shear: causes, cases, cures. Paper SPE 72060-PA. *SPE Drilling & Completion*, **16** (2), 98-107.

ESHELBY, J.D. 1957. The determination of the elastic field of an ellipsoidal inclusion, and related problems. *Proceedings of the Royal Society of London, Series A*, **241**, 376-396.

FISHER, K. & WARPINSKI, N. 2012. Hydraulic-fracture-height growth: Real data. *SPE Production & Operations*, **27**, 8–19.

FLEWELLING, S. A., TYMCHAK, M. P. & WARPINSKI, N. 2013. Hydraulic fracture height limits and fault interactions in tight oil and gas formations. *Geophysical Research Letters*, **40**, 3602–3606.

FOJTÍKOVÁ, L., VAVRYČUK, V., CIPICAR, A. & MADARÁS, J. 2010. Focal mechanisms of micro-earthquakes in the Dobrá Voda seismoactive area in the Malé Karpaty Mts. (Little Carpathians), Slovakia. *Tectonophysics*, **492**, 213–229.

GALE, J. F. W., REED, R. M. & HOLDER, J. 2007. Natural fractures in the Barnett Shale and their importance for hydraulic fracture treatments. *AAPG Bulletin*, **91**, 603–622.

GALLOWAY, D. D. 2012. *Bulletin of British Earthquakes 2011*. British Geological Survey Internal Report, OR/12/041. British Geological Survey, Edinburgh, 46 pp. Available online: http://www.earthquakes.bgs.ac.uk/publications/bulletins/Eqbull2011.pdf (accessed 8 March 2015).

GREEN, C. A., STYLES, P. & BAPTIE, B. J. 2012. *Preese Hall shale gas fracturing: review & recommendations for induced seismic mitigation*. UK Government Department of Energy and Climate Change, London, 26 pp. Available online: https://www.gov.uk/government/uploads/system/uploads/attachment_data/file/48330/5055-preese-hall-shale-gas-fracturing-review-and-recomm.pdf (accessed 3 January 2014)

GRIFFITH, A. A. 1921. The phenomena of rupture and flow in solids. *Philosophical Transactions of the Royal Society of London, Series A*, **221**, 163–198.

GRIFFITH, A. A. 1924. *The theory of rupture*. In: BIEZENO, C. B. & BURGERS, J. M. (eds), Proceedings of the First International Congress of Applied Mechanics, Delft, The Netherlands. Technische Boekhandel en Drukkerij, Delft, The Netherlands, pp. 55–63.

HACKSTON, A. & RUTTER, E. 2016. The Mohr–Coulomb criterion for intact rock strength and friction – a re-evaluation and consideration of failure under polyaxial stresses. *Solid Earth*, **7**, 493–508. doi: 10.5194/se-7-493-2016

HÄRING, M. O., SCHANZ, U., LADNER, F. & DYER, B. C. 2008. Characterization of the Basel 1 enhanced geothermal system. *Geothermics*, **37**, 469–495.

HARPER, T. R. 2011. *Well Preese Hall-1: The mechanism of induced seismicity*. Geosphere Ltd., Beaworthy, Devon, 67 pp. Available online: http://www.cuadrillaresources.com/wp-content/uploads/2012/06/Geosphere-Final-Report.pdf (accessed 17 October 2015)

HELLER, R., VERMYLEN, J. & ZOBACK, M. 2014. Experimental investigation of matrix permeability of gas shales. *AAPG Bulletin*, **98**, 975–995.

HERRMANN, R. B., PARK, S.-K. & WANG, C.-Y. 1981. The Denver earthquakes of 1967–1968. *Bulletin of the Seismological Society of America*, **71**, 731–745.

HITZMAN, M. W., CLARKE, D. D., DETOURNAY, E., DIETERICH, J. H., DILLON, D. K., GREEN, S. J., HABIGER, R. M., McGUIRE, R. K., MITCHELL, J. K., SHEMETA, J. E. & SMITH, J. L. 2013. *Induced seismicity potential in energy technologies*. The National Academies Press, Washington, D.C., 262 pp. Available online: http://www.nap.edu/catalog/13355/induced-seismicity-potential-in-energy-technologies (accessed 24 August 2016)

HOFMANN, H., BABADAGLI, T., YOON JEOUNG SEOK, BLÖCHER, G. & ZIMMERMANN, G. 2016. A hybrid discrete/finite element modeling study of complex hydraulic fracture development for enhanced geothermal systems (EGS) in granitic basements. *Geothermics*, **64**, 362–381.

IGAS, 2014. *Executive summary of Barton Moss well results*. iGas Energy plc, London, 6 pp. Available online: www.igasplc.com/media/10895/barton-moss-results.pdf (accessed 1 December 2016)

IRWIN, G. 1957. Analysis of stresses and strains near the end of a crack traversing a plate. *Journal of Applied Mechanics*, **24**, 361–364.

JACKSON, R., GORODY, A., MAYER, B., ROY, J., RYAN, M. & VAN STEMPVOORT, D. 2013. Groundwater protection and unconventional gas extraction: The critical need for field-based hydrogeological research. *Groundwater*, **51**, 488–510.

JAEGER, J. C. 1964. *Elasticity, fracture and flow*. Methuen and Co., London, 212 pp.

JENNINGS, A. R., JR. 2008. *Comments concerning limited entry treatment applications*. Enhanced Well Stimulation, Inc., Whitehouse, Texas. Available online: http://www.ewstim.com/limitedentry.asp (accessed 1 December 2016)

KENT, G. 2016. *Alberta regulator allows fracking to resume after quake near Fox Creek*. The Edmonton Journal, Edmonton, Alberta. Available online: http://edmontonjournal.com/business/energy/alberta-regulator-allows-fracking-to-resume-after-quake-near-fox-creek (accessed 26 August 2016)

KINGDON, A. 2016. *Comment on use of data and figures in Smythe paper*. Interactive Discussion item SC15, 5 pp. Available online: http://www.solid-earth-discuss.net/se-2015-134/discussion (accessed 31 March 2016)

JOHNSON, K. L. & YOUNGER, P. L. 2002. Hydrogeological and geochemical consequences of the abandonment of Frazer's Grove carbonate hosted Pb/Zn fluorspar mine, North Pennines, UK. In: YOUNGER, P. L. & ROBINS, N. S. (eds), *Mine Water Hydrogeology and Geochemistry*. Geological Society, London, Special Publications, 198, 347-363.

MA SHOU, GUO JIANCHUN, LI LIANCHONG, XIA YINGJIE & YANG TAO 2016. Experimental and numerical study on fracture propagation near open-hole horizontal well under hydraulic pressure. *European Journal of Environmental and Civil Engineering*, **20**, 412–430.

McCLURE, M. W. 2015. Generation of large postinjection-induced seismic events by backflow from dead-end faults and fractures. *Geophysical Research Letters*, **42**, 6647–6654.

McCLURE, M. W., BABAZADEH, M., SHIOZAWA, S. & HUANG JIAN 2015. *Fully coupled hydromechanical simulation of hydraulic fracturing in three-dimensional discrete fracture networks*. SPE Hydraulic Fracturing Technology Conference, The Woodlands, Texas, 3–5 February 2015. SPE paper 173354-MS, 26 pp.

McCLURE, M. W., JUNG, H., CRAMER, D. D. & SHARMA, M. M., 2016. The fracture-compliance method for picking closure pressure from diagnostic fracture-injection tests. *SPE Journal*, **21** (04), 1321-1339.

McGarr, A., Bekins, B., Burkardt, N., Dewey, J., Earle, P., Ellsworth, W., Ge, S., Hickman, S., Holland, A., Majer, E., Rubinstein, J. & Sheehan, A. 2015. Coping with earthquakes induced by fluid injection. *Science*, **347**, 830-831.

McGarr, A. & Gay, N. C. 1978. State of stress in the Earth's crust. *Annual Reviews of Earth and Planetary Science*, **6**, 405-436.

McGarr, A., Simpson, D. & Seeber, L. 2002. Case histories of induced and triggered seismicity. *International Handbook of Earthquake and Engineering Seismology*, **81A**, 647–661.

McKenzie, D. P. 1969. The relationship between fault plane solutions for earthquakes and the directions of the principal stresses. *Bulletin of the Seismological Society of America*, **59**, 591-601.

Majer, E., Baria, R., Stark, M., Oates, S., Bommer, J., Smith, B. & Asanuma, H. 2007. Induced seismicity associated with enhanced geothermal systems. *Geothermics*, **36**, 185–222.

Maxwell, S. C. 2011. What does microseismic tell us about hydraulic fracture deformation? *CSEG Recorder*, **36** (8), 30-45.

Maxwell, S. C., Zhang, F. & Damjanac, B. 2015. Geomechanical modelling of induced seismicity resulting from hydraulic fracturing. *The Leading Edge*, **34**, 678-683.

Nicholson, C. & Wesson, R. L. 1990. Earthquake hazard associated with deep well injection - a report to the U.S. Environmental Protection Agency. *U.S. Geological Survey Bulletin* **1951**, 74 pp.

Nolte, K. G. & Smith, M. B. 1981. Interpretation of fracturing pressures. SPE paper 8297-PA. *SPE Journal of Petroleum Technology*, **33**, 1767-1775.

O'Malley, D., Karra, S., Currier, R. P., Makedonska, N., Hyman, J. D. & Viswanathan, H. S. 2016 Where does water go during hydraulic fracturing? *Groundwater*, **54**, 488–497.

O'Toole, T., Verdon, J. P., Woodhouse, J. H. & Kendall, J. M. 2013. *Induced seismicity at Preese Hall, UK—A review*. 75th EAGE Conference and Exhibition incorporating SPE EUROPEC 2013, London. Extended abstract, 5 pp, doi: 10.3997/2214-4609.20130011. Available online: http://www.earthdoc.org/publication/publicationdetails/?publication=68869 (accessed 27 March 2015)

Rahman, M. M. & Rahman, M. K. 2010. A review of hydraulic fracture models and development of an improved pseudo-3D model for stimulating tight oil/gas sand. *Energy Sources, Part A*, **32**, 1416–1436.

Raleigh, C. B., Healy, J. H. & Bredehoeft, J. D. 1976. An experiment in earthquake control at Rangely, Colorado. *Science*, **191**, 1230-1237.

Ramsey, J. M. & Chester, F. M. 2004. Hybrid fracture and the transition from extension fracture to shear fracture. *Nature*, **428**, 63–66.

Rankine, W. J. M. 1843. On the causes of the unexpected breakage of the journals of railway axles, and on the means of preventing such accidents by observing the law of continuity in their construction. *Minutes of the Proceedings of the Institution of Civil Engineers*, **2**, 105-107.

Rankine, W. J. M. 1858. *A Manual of Applied Mechanics*. Richard Griffin and Company, Glasgow, 640 pp.

Rutqvist, J., Rinaldi, A. P., Cappa, F. & Moridis, G. J. 2013. Modeling of fault reactivation and induced seismicity during hydraulic fracturing of shale-gas reservoirs. *Journal of Petroleum Science and Engineering*, **107**, 31–44.

Rutter, E. H. & Mecklenburgh, J. 2017. Hydraulic conductivity of bedding-parallel cracks in shale as a function of shear and normal stress. In: Rutter, E. H., Mecklenburgh, J. & Taylor, K. G. (eds) Geomechanical and Petrophysical Properties of Mudrocks. Geological Society, London, Special Publication 454, http://doi.org/10.1144/SP454.

Schlumberger 2016. *Signature Quartz Gauges: Reliable, accurate pressure measurements in any environment*. Schlumberger Limited, Willemstad, Curaçao, the Netherlands. Available online: https://www.slb.com/~/media/Files/testing/.../pressure/signature_quartz_gauge_ps.pdf (accessed 21 August 2016)

Seeber, L., Armbruster, J. & Kim, W.-Y. 2004. A fluid-injection-triggered earthquake sequence in Ashtabula, Ohio: Implications for seismogenesis in stable continental regions. *Bulletin of the Seismological Society of America*, **94**, 76–87.

Smythe, D.K. 2015. *The insolence of office*. Available online: http://www.davidsmythe.org/professional/insolence.html (accessed 3 February 2016)

Sneddon, I. N. 1951. *Fourier Transforms*. McGraw-Hill, New York, 542 pp.

Thorogood, J. L. & Younger, P. L. 2015. Discussion of "Oil and gas wells and their integrity: Implications for shale and unconventional resource exploitation" by R.J. Davies, S. Almond, R.S., Ward, R.B. Jackson, C. Adams, F. Worrall, L.G. Herringshaw, J.G. Gluyas and M.A. Whitehead. (Marine and Petroleum Geology 2014). *Marine and Petroleum Geology*, **59**, 671-673.

Weingarten, M., Ge, S., Godt, J. W., Bekins, B. A. & Rubinstein, J. L. 2015. High-rate injection is associated with the increase in U.S. mid-continent seismicity. *Science*, **348**, 1336-1340.

Westaway, R. 2015. Induced seismicity. In: Kaden, D. & Rose, T. L. (eds), *Environmental and Health Issues in Unconventional Oil and Gas Development*. Elsevier, Amsterdam, pp. 175-210.

Westaway, R. 2016a. The importance of characterizing uncertainty in controversial geoscience applications: induced seismicity associated with hydraulic fracturing for shale gas in northwest England. *Proceedings of the Geologists' Association*, **127**, 1–17.

Westaway, R. 2016b. *Diversity of stratigraphic interpretations for the Preese Hall-1 well and surroundings*. Interactive Discussion item SC12, 10 pp. Available online: http://www.solid-earth-discuss.net/se-2015-134/discussion (accessed 26 June 2016)

Westaway, R. 2016c. *Some additional thoughts on Preese Hall*. Solid Earth Discussions, Interactive Discussion item SC10, 9 pp. Available online: http://www.solid-earth-discuss.net/se-2015-134/discussion (accessed 13 August 2016)

Westaway, R. 2016d. *Preese Hall-1 bedding dip*. Solid Earth Discussions, Interactive Discussion item SC17, 4 pp. Available online: http://www.solid-earth-discuss.net/se-2015-134/discussion (accessed 9 August 2016)

Westaway, R. & Younger, P. L. 2014. Quantification of potential macroseismic effects of the induced seismicity that might result from hydraulic fracturing for shale gas exploitation in the UK. *Quarterly Journal of Engineering Geology and Hydrogeology*, **47**, 333–350.

Westaway, R. & Younger, P. L. 2016. Unravelling the relative contributions of climate change and ground disturbance to subsurface temperature perturbations: Case studies from Tyneside, UK. *Geothermics*, **64**, 490–515.

Yoon Jeoung Seok, Zang, A. & Stephansson, O. 2014. Numerical investigation on optimized stimulation of intact and naturally fractured deep geothermal reservoirs using hydro-mechanical coupled discrete particles joints model. *Geothermics*, **52**, 165–184.

Younger, P. L. 1993. Possible environmental impact of the closure of two collieries in County Durham. *Water and Environment Journal*, **7**, 521–531.

Zhang Zhaobin & Li Xiao 2016. The shear mechanisms of natural fractures during the hydraulic stimulation of shale gas reservoirs. *Materials*, **9**, 713, 14 pp. doi: 10.3390/ma9090713

Zimmermann, G., Moeck, I. & Blöcher, G. 2010. Cyclic waterfrac stimulation to develop an enhanced geothermal system (EGS)—conceptual design and experimental results. *Geothermics*, **39**, 59-69.

Table N1: Details of the Preese Hall-1 well – on a separate sheet

Table N2: Summary of the de Pater and Pellicer (2011) analysis – on a separate sheet

Table N3: Analysis of fracking stage 1

μ (GPa)	ν	E (GPa)	H (m)	w_o (mm)
10	0.15	23.0	313.4	12.4
10	0.2	24.0	318.2	12.1
10	0.25	25.0	323.4	11.7
10	0.3	26.0	329.0	11.3
15	0.15	34.5	346.9	10.1
15	0.2	36.0	352.2	9.8
15	0.25	37.5	357.9	9.5
15	0.3	39.0	364.1	9.2
20	0.15	46.0	372.7	8.8
20	0.2	48.0	378.4	8.5
20	0.25	50.0	384.6	8.3
20	0.3	52.0	391.3	8.0

Calculations of fracture height H and maximum fracture width w_o assume the listed values of shear modulus μ and Poisson's ratio ν, along with V=1969 m^3 (Table N1). It is also assumed that fracture growth occurred under zero net pressure conditions at the injection point, from which it follows that C=2, so L=2×H, and with K=7.2 kPa m^{-1}. H and w_o are calculated using the procedure explained in section 4 of the supplementary material. Values of Young's modulus E are calculated from μ and ν.

Table N4: Analysis of the final configuration of the stage 1 fracture

μ (GPa)	ν	E (GPa)	H (m)	w_o (mm)
10	0.15	23.0	354.8	15.9
10	0.2	24.0	360.2	15.5
10	0.25	25.0	366.1	15.0
10	0.3	26.0	372.4	14.4
15	0.15	34.5	392.6	13.0
15	0.2	36.0	398.6	12.6
15	0.25	37.5	405.1	12.2
15	0.3	39.0	412.2	11.8
20	0.15	46.0	421.9	11.3
20	0.2	48.0	428.4	10.9
20	0.25	50.0	435.3	10.6
20	0.3	52.0	442.9	10.2

This Table lists sets of parameters describing the final dimensions of the fracture that originally developed during stage 1, after it became interconnected with that which developed during the initial part of stage 2 and thus ended up containing much of the fluid volume injected during stage 2. Calculations of fracture height H and maximum fracture width w_o assume the listed values of shear modulus μ and Poisson's ratio ν, along with V=3232 m^3 (see text). Calculation procedures, assumed pressure conditions, and assumed values of other parameters, are the same as for Table N3.

Table N5: Focal mechanism orientation predictions from stress analysis

_____

	Null axis		Slip vector	
Depth (m)	Plunge (°)	Azimuth (°)	Plunge (°)	Azimuth (°)
2600	60.90	181.23	24.32	36.95
2650	60.95	181.15	24.26	36.93
2700	61.01	181.08	24.19	36.91
2750	61.06	181.01	24.13	36.89
2800	61.11	180.95	24.07	36.88
2850	61.16	180.88	24.02	36.86

This table lists predicted orientations of focal mechanisms of induced earthquakes occurring on patches of fault with strike 030° and dip 75°, given the ambient stress field at Preese Hall (as described by equations (1) to (3)), for a plausible range of focal depths. The calculation procedure is explained in section 5 of the supplementary material. The model fault is extrapolated with planar orientation to shallower depths than those depicted in Figs 9, 11, 12, and 13, for the purpose of these calculations. The actual fault may have sharper curvature than depicted and so may attain a 75° dip at a shallower depth than depicted.

Figure 1. Map of the Preese Hall-1 well and its surroundings, from Fig. 1 of Westaway (2016a), modified after Fig. 1 of Clarke *et al*. (2014), showing the planform of this deviated well (BGS inventory code SD33NE38; wellhead at British National Grid co-ordinates SD 37531 36627), temporary local seismograph stations, epicentral locations for induced earthquakes, and the positions of the adjacent Thistleton-1 (BGS inventory code SD33NE17; co-ordinates SD 39760 37000) and Elswick 1 (BGS inventory code SD43NW15; co-ordinates SD 42380 36965) wells and of the cross-sections in Figs 3 and 4. The epicentral locations determined by BGS (Galloway, 2012) for the 1 April 2011 and 27 May 2011 events and by O'Toole *et al*. (2013) for the latter event are also shown. The Westaway (2016a) epicentral co-ordinates for the 2 August 2011 event have been drawn with nominal error bars indicating uncertainties of 100 m, except that pointing north has been extended in recognition of the fact (evident for reasons discussed by Westaway 2016a) that this location is subject to significant systematic error and probably lies well north or NNW of the co-ordinates marked. Crosses labelled 1, 2 and 3 mark the points where faults 1-3 in Fig. 3 intersect the line of this seismic section at the top of the Clitheroe Limestone Formation (the dual symbols for faults 1 and 2 mark the footwall and hanging-wall cutoffs). The geometry of the seismogenic fault inferred by Clarke *et al*. (2014) (Fig. 4) is depicted at a depth of 2930 m. That inferred in the present study is depicted at a depth of 2740 m (Fig. 4), projected SSW for ~500 m assuming a N30°E-S30°W strike, and ornamented to indicate both the polarity of the overall fault offset and the inferred sense of coseismic slip in 2011. The induced fractures are depicted as emanating at a N7°E-S7°W azimuth (see the main text) from a notional point near the bottom of the PH1 well. The fracture length depicted is ~300 m, rather less than is now considered reasonable in the light of the present study. Westaway (2016a) concluded that the probable true location of the induced seismicity is at the intersection of this induced fracture trend with his projection of the fault line, most likely several hundred metres south or SSE of the PH1 wellhead. 'Beach ball' diagram in bottom left is a standard representation of Westaway's (2016a) solution for the focal mechanism orientation of the induced seismicity, with strike 030°, dip 75°, and rake -20°. It is drawn as a standard equal area projection of the lower hemisphere of the focal sphere, with compressional quadrants shaded. The axes of the solution are labelled using standard symbols, the U-axis coinciding with the slip vector as the 030°-striking nodal plane is thought to be the fault plane. Westaway (2016a) discussed comparisons between this solution and the works of others, although this task was not straightforward because not everyone has followed the standard conventions for display of focal mechanisms, so it is not entirely clear what some published diagrams actually mean. Inset shows location, along with a selection of the permanent seismograph stations (none closer than ~80 km; see Galloway 2012 for further details) that recorded the largest PH1 microearthquake on 1 April 2011 and the sites from which *in situ* stress measurements are discussed (B, Burton-in-Kendal; S, Sellafield).

Figure 2. Map of shale gas resource areas in northern/central England, modified after Fig. 43 of Andrews (2013), showing the boundary of the study area for this resource assessment. This map indicates the resource identified in those parts of the specified rock formations that are inferred to be mature for gas generation (vitrinite reflectance parameter R_o >1.1%) and deeper than a depth threshold, which was set by Andrews (2013) at 1524 m (i.e., 5000 ft) below the land surface in onshore areas and 1524 m below sea level in offshore areas. The principal cities in this study region are indicated thus: LS, Leeds; L, Liverpool; M, Manchester; NG, Nottingham; and S, Sheffield. The resource areas depicted are located within, clockwise from the northeast, the Cleveland, Gainsborough/Edale, Widmerpool, Cheshire, Bowland and Harrogate basins; + symbol marks the position of the PH1 well (cf. Fig. 1). Inset shows location.

Figure 3. Excerpt from an east-west seismic section from seismic line GC83-352, with shot points of standard 12.5 m spacing, passing ~400 m north of the Preese Hall-1 well, modified from Fig. 7 of de Pater & Baisch (2011). See Fig. 1 for location; projected to this section-line, the Thistleton-1 well is 2134 m east of the PH1 well and 2503 m west of the Elswick-1 well. Symbols identifying stratigraphic boundaries are keyed to Fig. 5(a). Interpreted faults labelled 'Type A' only occur within the Carboniferous sedimentary section whereas the less numerous 'Type B' faults pass upwards across the Variscan Unconformity (at the base of the Collyhurst Sandstone Formation – CS; Fig. 5(a)). Three 'Type A' faults are labelled 1-3 to facilitate discussion. Please refer to Fig. 5(a) caption regarding interpretation of stratigraphic boundaries beneath the Variscan Unconformity.

Figure 4. Excerpt from Fig. 4 of Clarke *et al*. (2014), modified after Fig. 4 of Westaway (2016a), showing a subset (rendered here as a vertical section oriented west-east) of the results of the 3-D seismic reflection survey undertaken in 2012 in the vicinity of the PH1 well. See Fig. 1 for presumed location. The section has been ornamented consistent with Fig. 5(a), using data from de Pater & Baisch (2011). The labelling is from the original Figure by Clarke *et al*. (2014), so cannot be removed; it evidently obscures much detail. Depths of well perforations for fracking stage 2 are quoted both as Measured Depth (MD) and as True Vertical Depth (TVD), and are consistent with Table N1 and the schematic depiction in Fig. 5(a). The zone of wellbore deformation between depths of ~2552 and ~2593 m (TVD) is depicted as a white section of the well track. Also depicted are the Clarke *et al*. (2014) hypocentre (open semicircle), which is mislocated (Westaway 2016a), and what they described as a 'simplified' depiction of their inferred seismogenic fault plane. The revised hypocentre, from Westaway (2016a), is south of this section plane (Fig. 1), so is not shown here. The focal mechanism orientation (Fig. 1) indicates that the fault plane at depths of >~2600 m was steeper than depicted by Clarke *et al*. (2014) although the upper part of their fault plane is drawn in roughly the right place. It is inferred (see main text) that at shallower depths this fault flattens in to the zone of wellbore deformation (see the supplementary material for details). Please refer to Fig. 5(a) caption regarding interpretation of stratigraphic boundaries beneath the Variscan Unconformity.

Figure 5. **(a)** Summary stratigraphic column for the PH1 well, modified from Fig. 3 of de Pater & Baisch (2011), along with the depths of the perforations for the five frack stages, from their Fig. 11 (see also Table N1). It is noted in passing that, while the present manuscript was in preparation, it became apparent that considerable uncertainty exists regarding the published depiction of stratigraphic and structural data pertaining to this well (Westaway, 2016a). Furthermore, new information pertaining to these issues was made public by Clarke (2016) and Kingdon (2016) as part of a wider online discussion. It thus became apparent that the depiction of the stratigraphy in this Figure is contradicted by biostratigraphic evidence and is thus incorrect: the rocks deeper than ~2000 m in reality represent the upper part of the Bowland Shale Formation, including interbedded limestone beds that had previously been mistaken for older formations. Subsequent checking by Westaway (2016b) established that, although it had not been made public at the time, the 'correct' stratigraphy had been known to the British Geological Survey for some time and was incorporated into the Andrews (2013) publication (cf. Fig. 2). The summary depiction of the shale gas resource in the present Fig. 2(b) thus requires no revision. **(b)** *In situ* stress measurements as a function of depth in the PH1 well. The data depicted are the maximum and minimum horizontal stresses, σ_H and σ_h, and the vertical stress σ_V. Calculated by numerical integration of graphs in Fig. 20 of de Pater & Baisch (2011), also showing the extrapolation curves from equations (1) to (3). Open symbols denote the (incorrect) principal stress values calculated by Cuadrilla (2014) at ~2440 m depth, for comparison. Also shown is the hydrostatic variation in pore fluid pressure, p_F, based on a pressure gradient of 0.446 psi per foot or ~10.1 kPa m^{-1}, from de Pater & Baisch (2011), which is consistent with a fluid density of ~1030 kg m^{-3}. Vertical bars labelled B and H denote the depth ranges of the *in situ* stress measurements by Baker Hughes (2011) and Harper (2011), respectively.

Figure 6. Analysis of the fluid injection during PH1 fracking stage 1. (a) Summary data, redrawn from Fig. 21 of de Pater & Baisch (2011). Note the use of non-systematic units of measurement: panel (i) depicts (upper trace) the measured well head pressure (WHP; in pounds per square inch, psi) and (lower trace) the measured density of proppant being injected (ρ_P; in pounds per gallon, ppg); panel (ii) depicts (upper trace) the bottom hole pressure (BHP) calculated from the other inputs (also in psi) and (lower trace) the measured injection rate (Q; in barrels per minute, bpm); (b) Digitizations of the variations in WHP, Q and ρ_P, from (a), likewise displayed using non-systematic units to facilitate comparison, together with estimates of σ_h BHP at the depth of injection. Calculations have been carried out as explained in section 3 of the supplementary material, using the following parameter values: $\Delta L=z_M=2720$ m, $\Delta Z=z_T=2667$ m, $\sigma_h=43.75$ MPa, D=127.3 mm, f=0.012, and g=9.81 m s^{-2}, with ρ equal to the density of water (1000 kg m^{-3} plus the density of the proppant present within each part of the borehole at each time step). Note the mismatch between the present set of calculated BHP values and those reported by de Pater & Baisch (2011). Right hand tick denotes the fluid pressure after 'shut in', from Table N1, included as a test of consistency of digitization. (c) The same data as in (b), displayed in SI units. (d) Key to parts (b) and (c).

Figure 7. Analysis of the fluid injection during PH1 fracking stage 2. (a) Summary data, redrawn from Fig. 22 of de Pater & Baisch (2011), displayed consistent with Fig. 6(a). (b) Digitizations of the variations in WHP, Q and ρ_P, from (a), and estimates of σ_h and BHP at the depth of injection. Calculations and display format are the same as for Fig. 6 except for use of the following parameter values: $\Delta L=z_M=2659$ m, $\Delta Z=z_T=2613$ m, and $\sigma_h=42.83$ MPa. Timings of induced earthquakes, from Fig. 25 of de Pater & Baisch (2011), are also shown. Note, once again, the mismatch between the present set of calculated values for BHP and those reported by de Pater & Baisch (2011). (c) The same data as in (b), displayed in SI units. (d) Key to parts (b) and (c).

Figure 8. Simple two-dimensional conceptual model for the state of stress in relation to the PH1 induced seismicity. This modified Mohr Circle construction (modified for reasons discussed in section 5 of the supplementary material) illustrates the state of stress at 2600 m depth (TVD) in the PH1 well (from Fig. 5(b)) relative to the condition for shear failure on an optimally-oriented vertical strike-slip fault. σ_H, σ_V and σ_h denote the principal stresses, 68.88, 59.06 and 42.60 MPa, respectively, calculated using equations (1) to (3) (cf. Fig. 5(b)). σ_M, the mean of σ_H and σ_h, is 55.74 MPa; P_L, the lithostatic pressure ($\sigma_H+\sigma_V+\sigma_h$)/3, is 56.85 MPa; and P_h, the initial fluid pressure, if hydrostatic (Fig. 5(b)), is 25.51 MPa. Dashed sloping line illustrates the frictional condition for slip, for a fault with a coefficient of friction, c, 0.6. The bold sloping line is constructed assuming the same coefficient of friction but that injection of fracking fluid raises the pressure within the fault above P_H by 15% of the difference between P_h and P_L, or to $P_F=30.21$ MPa. This line now touches the Mohr circle, making the fault frictionally unstable and thus able to slip in an induced earthquake. The optimum fault orientation to which this calculation applies (T in Mohr circle space, displaced to T' by the pressure increase) is at an angle of (90° − arctan(c))/2 or ~29.52° to the minimum principal stress, i.e., at azimuth 037° or N37°E for left-lateral slip or 337° or N23°W for right-lateral slip on vertical faults. This diagram supersedes a version published previously (Fig. 3(d) of Westaway 2015; Fig. 6 of Westaway 2016a), which was based on wrong information reported by Cuadrilla (2014) regarding the magnitudes of the principal stresses (see Fig. 5(b), also section 2 of the supplementary material).

Figure 9. Graphical description of the interaction between the model fault and the model fracture induced by PH1 fracking stage 1. The solutions depicted represent minimum-pressure conditions, corresponding (a) and (b) to the first row of Table N3, with μ=10 GPa and ν=0.15, indicating the smallest of the model fractures created, and (c) and (d) to the last row of Table N3, with μ=20 GPa and ν=0.30, indicating the largest of the model fractures created. Other parameter values are as discussed in the text. The model fault is illustrated in the plan views (a) and (c) as a series of structure contours at 20 m intervals, between 2580 m and 3100 m depths (TVD), with contours at multiples of 100 m in darker ornament (and with the 2580 m contour repeated at either end of the model 'flat' at this depth), and in the cross sections (b) and (d) as thick curved lines. These cross sections are oriented N60°W-S60°E along the line depicted in (a) and (c), with the induced fracture projected onto this section line from either side.

Figure 10. Analysis of the condition for shear failure for the model fault in Fig. 9 (also for Fig. 13). The principal stresses, fluid pressure and dip of the model fault are assumed to vary with depth as described in the text, and c is taken as 0.6. At each depth σ_n, τ, and Φ are calculated using the method set out in section 5 of the supplementary material. See text for discussion.

Figure 11. Graphical description of the interaction between the model fault and the model fracture induced by PH1 fracking stage 2, using the same display format as Fig. 9. The calculations relate to the time when fluid injection was suspended at the end of phase 1 of stage 2. Calculations assume the following parameter values, discussed in the text: V=1200 m³; K=7.2 kPa m⁻¹; μ=10 GPa; ν=0.15; σ_3=42.82 MPa at the injection point where the BHP was 60.0 MPa, roughly consistent with M=24; and C=1 so H=2L and the induced fracture is assumed to be circular. The calculation yields H=176.9 m; for M=24, y_o is ~0.02×H so the model fracture is positioned with its mid-point 4 m above the injection point. **(a)** Plan view. **(b)** Cross section oriented N60°W-S60°E along the line depicted in (a).

Figure 12. Graphical description of the interaction between the model fault and the model fracture induced by PH1 fracking stage 2, using the same display format as Fig. 9. The calculations relate to the origin time of the first induced earthquake during stage 2 which, it is suggested, marks the time when this induced fracture breached upward into the 'flat'. Calculations assume the same parameter values as Fig. 11 except for V=1076 m³; the calculation yields H=172.2 m. **(a)** Plan view. **(b)** Cross section oriented N60°W-S60°E along the line depicted in (a).

Figure 13. Graphical description of the interaction between the model fault and the model fracture during 'shut in' at the end of PH1 fracking stage 2, using the same format as in Fig. 9. The solutions depicted represent minimum-pressure conditions, corresponding (a) and (b) to the first row of Table N4, with μ=10 GPa and ν=0.15, indicating the smallest of the model fractures created, and (c) and (d) to the last row of Table N4, with μ=20 GPa and ν=0.30, indicating the largest of the model fractures created. Other parameter values are as discussed in the text.

Figure 14. Graphical description of the interaction between the model fault and the model fracture induced by PH1 fracking stage 4, using the same display format as Fig. 9. The calculations relate to the point when the first induced earthquake during stage 4 occurred which, it is suggested, marked the point in time when this induced fracture breached downward into the 'flat'. Calculations assume the following parameter values, discussed in the text: V=1280 m³; K=7.2 kPa m⁻¹; μ=10 GPa; ν=0.15; σ_3=40.15 MPa at the injection point where the BHP is 51.0 MPa, roughly consistent with M=15; and C=2 so H=L. The calculation yields H=170.1 m; for M=15, y_o is ~0.033×H so the model fracture is positioned with its mid-point 6 m above the injection point. **(a)** Plan view. **(b)** Cross section oriented N60°W-S60°E along the line depicted in (a).

Figure 15. Schematic conceptual model, not to scale (although with horizontal exaggeration), for PH1 fracture development and induced seismicity. These cross-sections are oriented N60°W-S60°E left to right, perpendicular to the strike of the seismogenic fault. Features that are not parallel to the section plane (such as the network of induced fractures) are projected into this plane, schematically, with their shapes distorted by foreshortening. Features that are behind the section plane, as viewed from S30°W, are omitted to avoid clutter. **(a)** The fracture that developed during fracking stage 1 cut across the 'flat' above the injection point but did not 'open' any of it as the fluid pressure was too low, the fluid not being under significant net pressure. The fracture also grew horizontally, its growth to the southward bringing it close to, but not reaching, the steep part of the fault. **(b)** Early in fracking stage 2 the induced fracture likewise grew upward towards the 'flat' above the injection point. Because the fluid at this time was under significant net pressure, this induced fracture also grew downward (not shown). When the fracture reached the 'flat', the fluid pressure was so high it 'opened' a patch of it, this event being marked by the first induced seismicity to occur. **(c)** As the initial patch of the 'flat' to be 'opened' included the point where the stage 1 induced fracture cut across the 'flat', fluid under high net pressure was able to flow into this fracture from the stage 2 induced fracture. As a result of this continued injection, the fracture originally created during stage 1 continued to grow. The high net pressure fluid entering the 'flat' 'opened' successively larger patches of it, in association with more induced earthquakes. **(d)** During 'shut in' following the stage 2 fluid injection, the fluid pressure gradually reduced and the fracture originally created during stage 1 continued to grow, ultimately intersecting the steep part of the fault south of the PH1 site. The fluid pressure was high enough to induce slip on a patch of this steep part of the fault, including the largest induced earthquake (M_L 2.3) in the sequence. **(e)** The injection point during stage 3 was at a very similar depth to the 'flat' and adjoined the patch of it that had already been 'opened' during stage 2. As a result, the interconnected fracture network created during stages 1 and 2 was open to the surface, facilitating the large volume of flowback that occurred during this stage. **(f)** The fluid was again under significant net pressure during fracking stage 4, so early during this stage the induced fracture grew downward, towards the 'flat' below the injection point, as well as upward (not shown). The patch of the 'flat' beneath the injection point had already been 'opened' by the fluid injection during stage 2. The breaching of this fracture into the 'flat' was accompanied by the first induced seismicity during stage 4. **(g)** As soon as the breaching described in (f) had occurred, the high net pressure fluid being injected was able to flow along the 'opened' patch of the 'flat' and into the fracture network created during fracking stages 1 and 2. After 'shut-in', the fluid pressure gradually declined and the fracture network adjusted. Movement of fluid into the 'opened' patch of the steep part of the fault resulted in continued induced seismicity, including the second largest event of the sequence (M_L 1.5) early on 27 May. **(h)** After the end of fluid injection (indeed, after the PH1 well was plugged and abandoned) the complex interconnected fracture network created by the combination of fracking stages 1, 2 and 4 continued to exist. Continuing fluid movements or pressure changes in the 'opened' patch of the steep part of the fault resulted in occasional induced earthquakes, including the event (M_L -0.2) on 2 August.
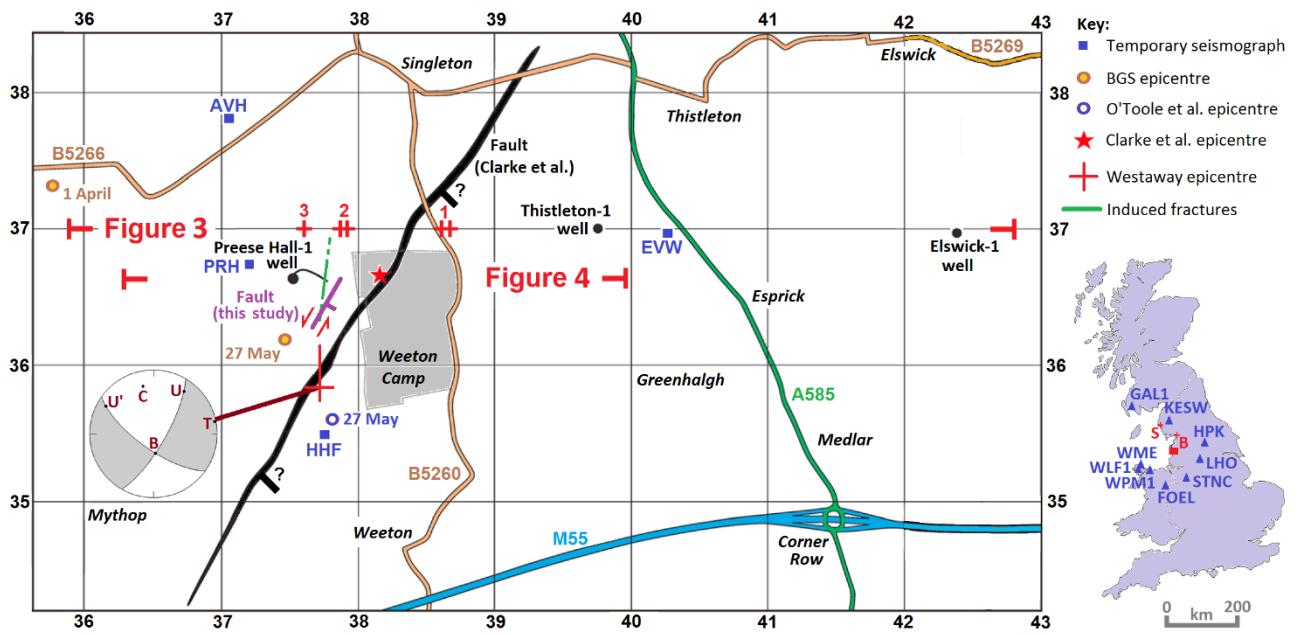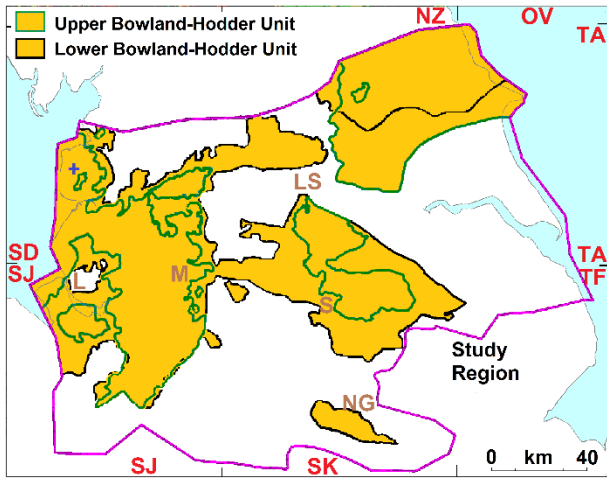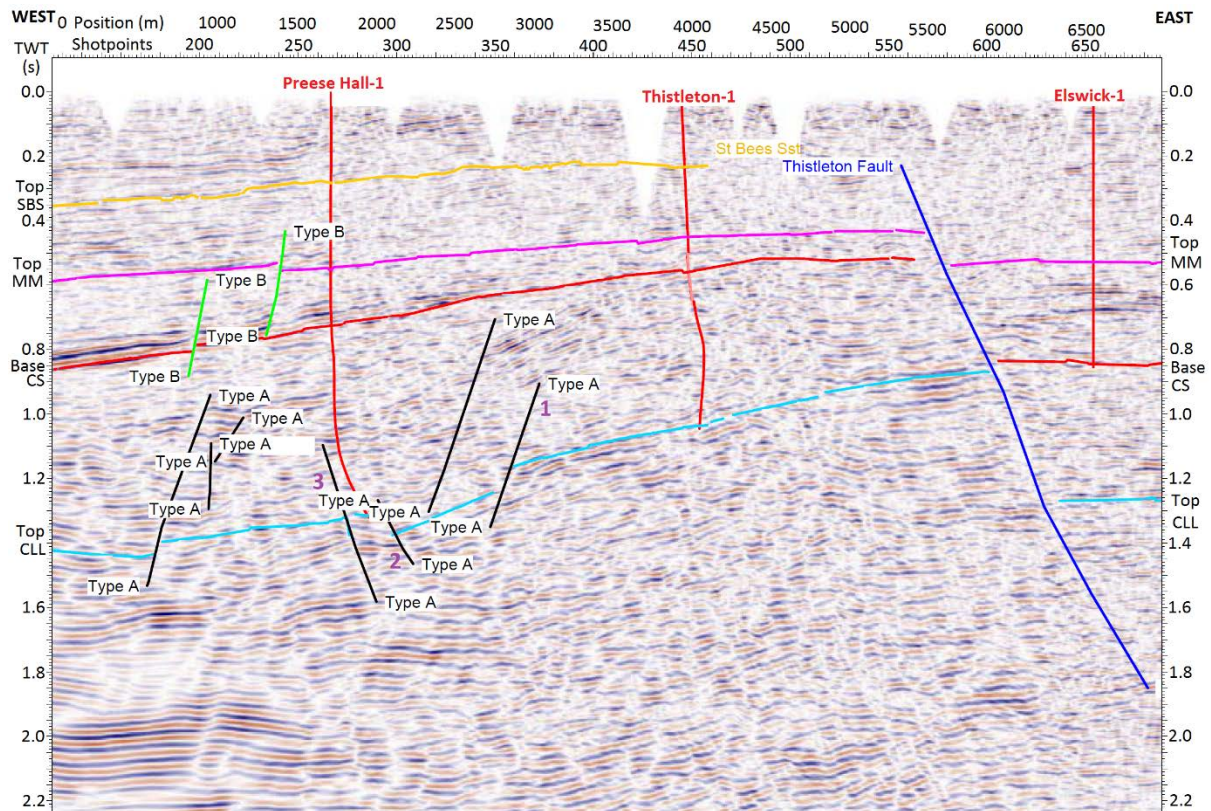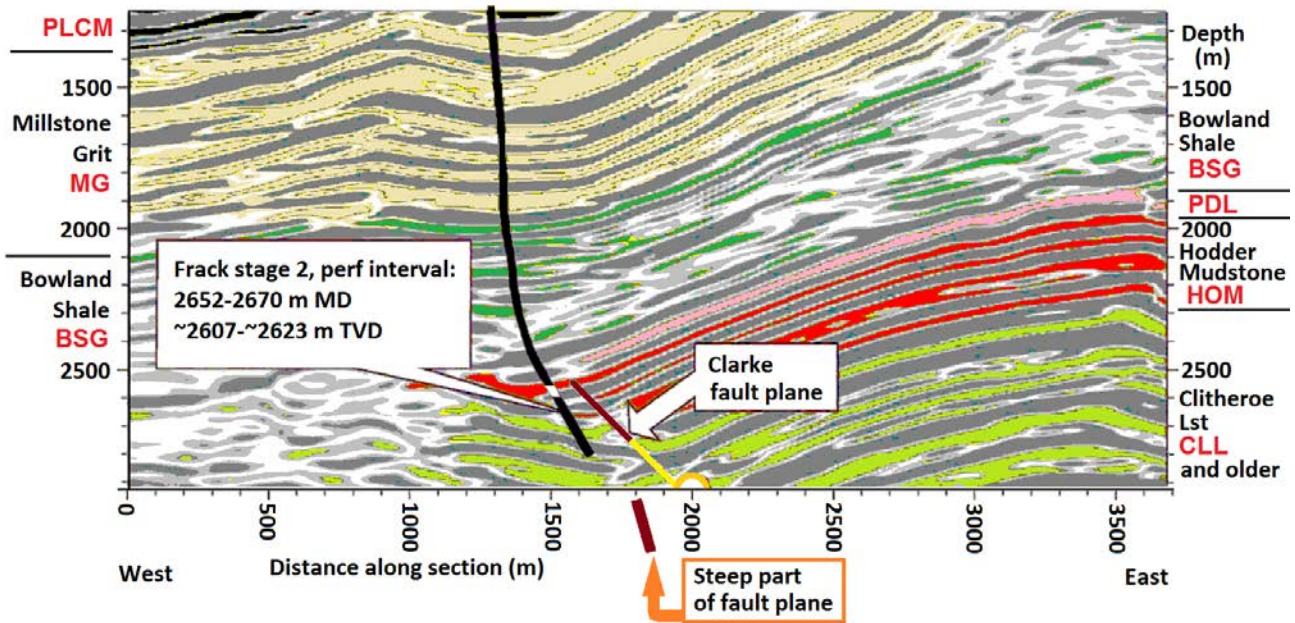
Figure 1

Figure 2

Figure 3

Figure 4
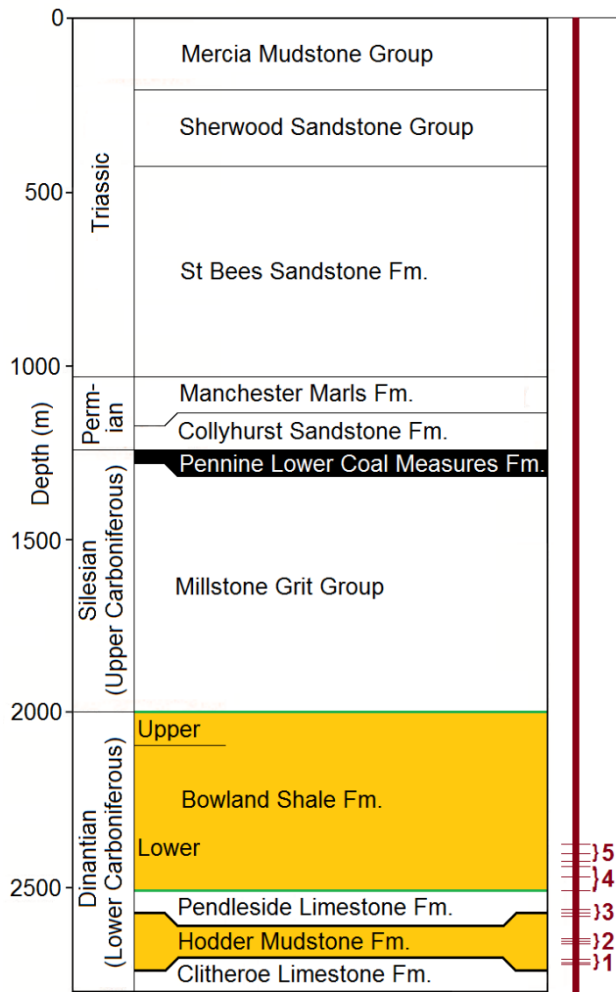
(a)

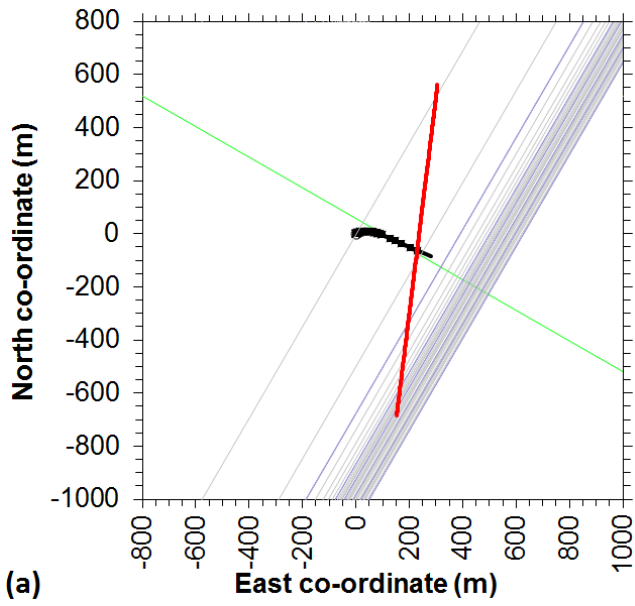Figure 5

(b)
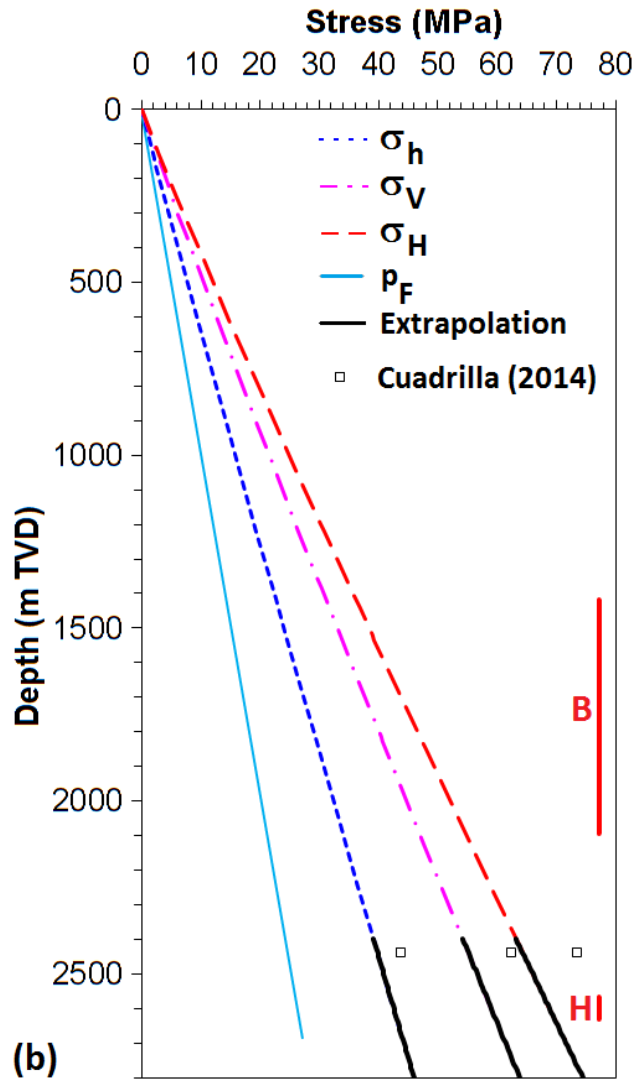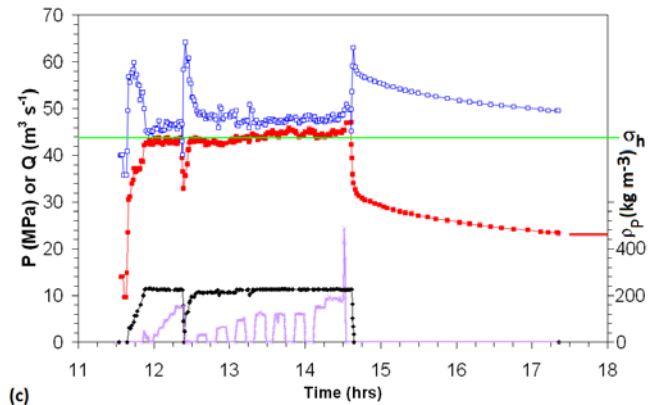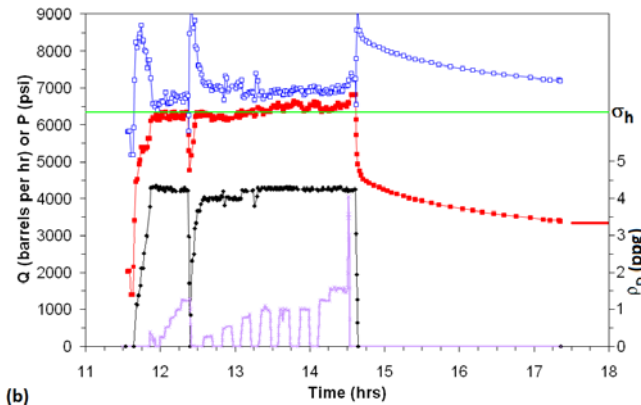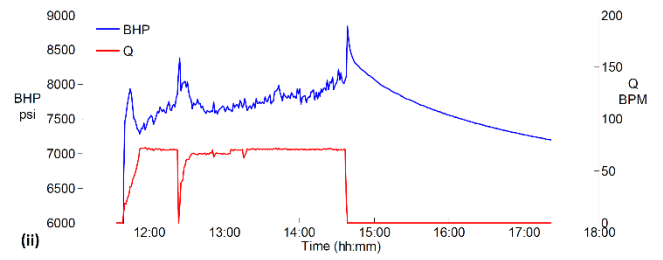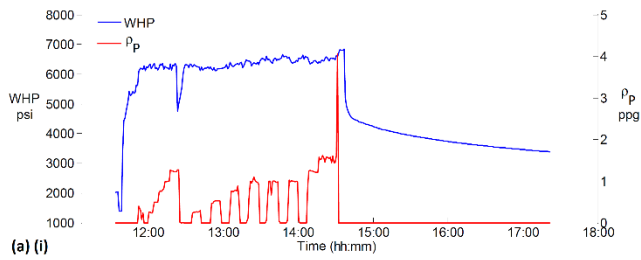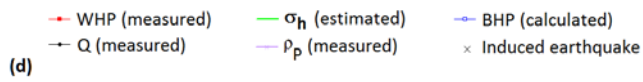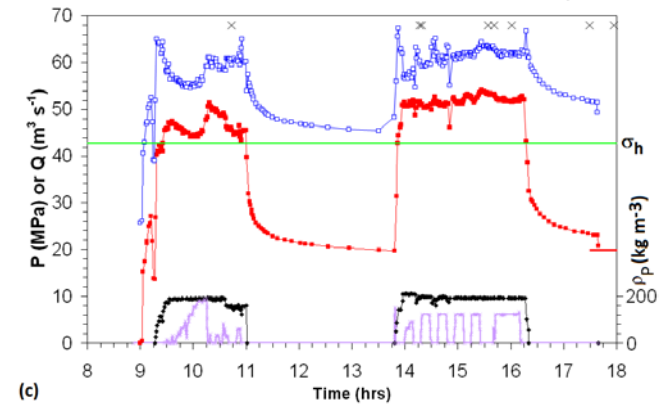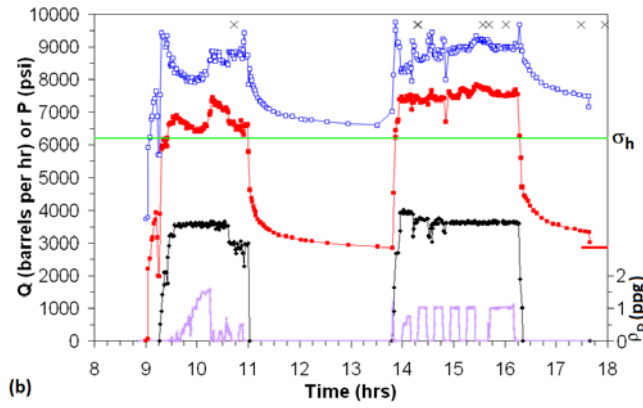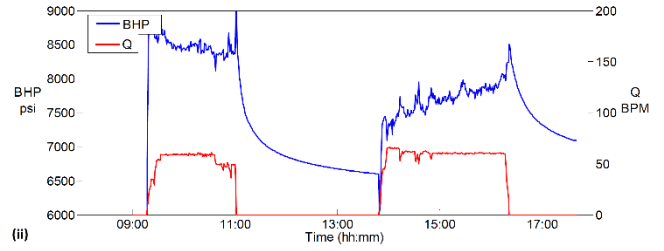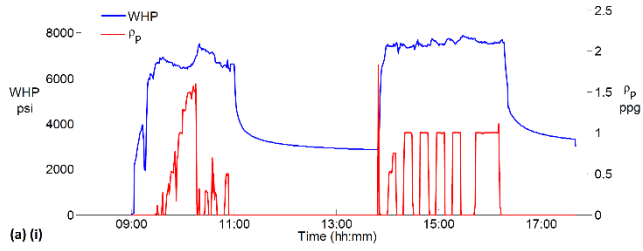
Figure 6

Figure 7

Figure 8

(a) **(b)** **(c)** **(d)**

Figure 9

Figure 10

(a)

(b)

Figure 11

(a)

(b)

Figure 12

(a)

(b)

(c)

(d)

Figure 13

(a)

(b)

Figure 14

(a) Late in fracking stage 1

(b) Early in fracking stage 2

(c) Part-way through stage 2

(d) Late in fracking stage 2

(e) During fracking stage 3

(f) Early in fracking stage 4

(g) Late in fracking stage 4

(h) Final configuration

Key:
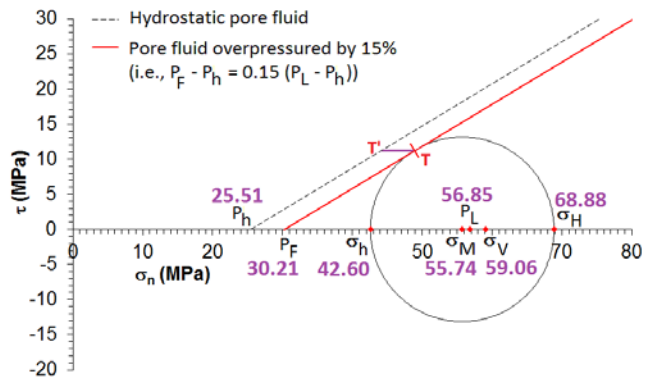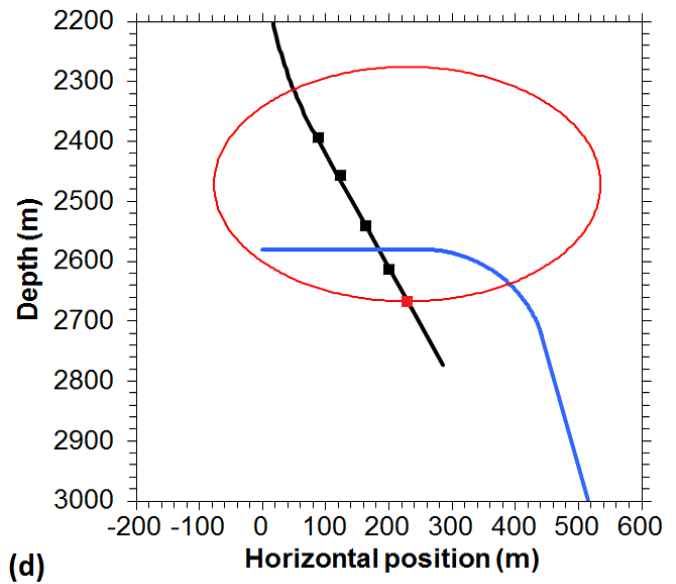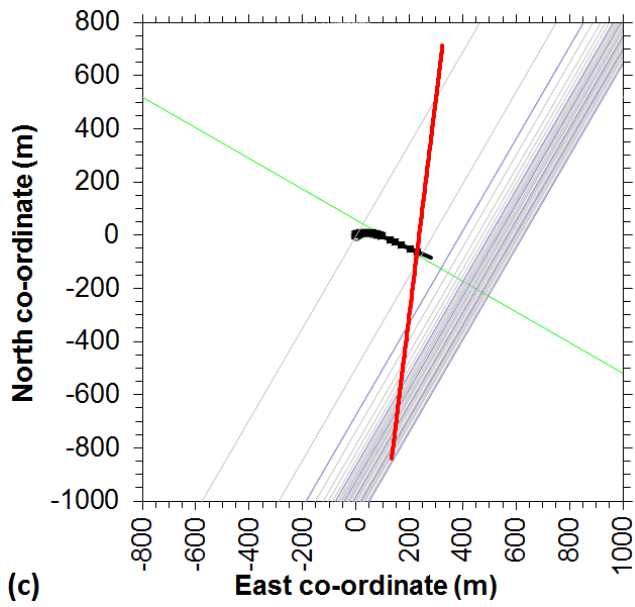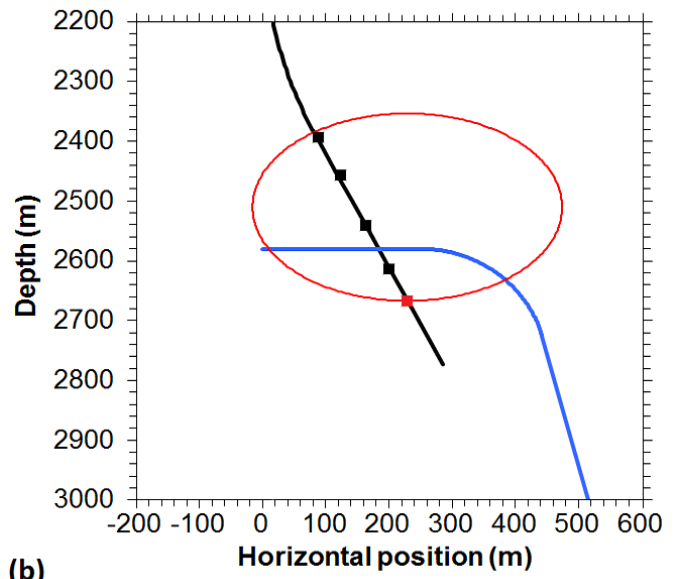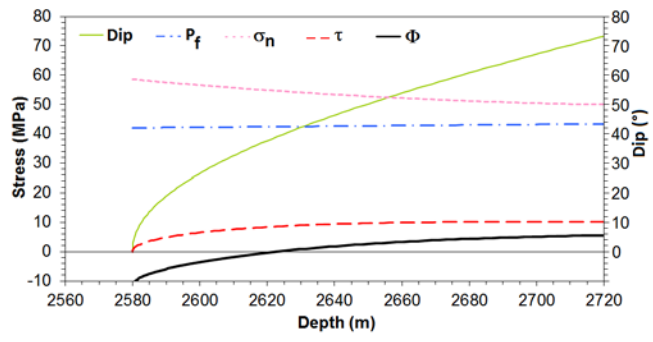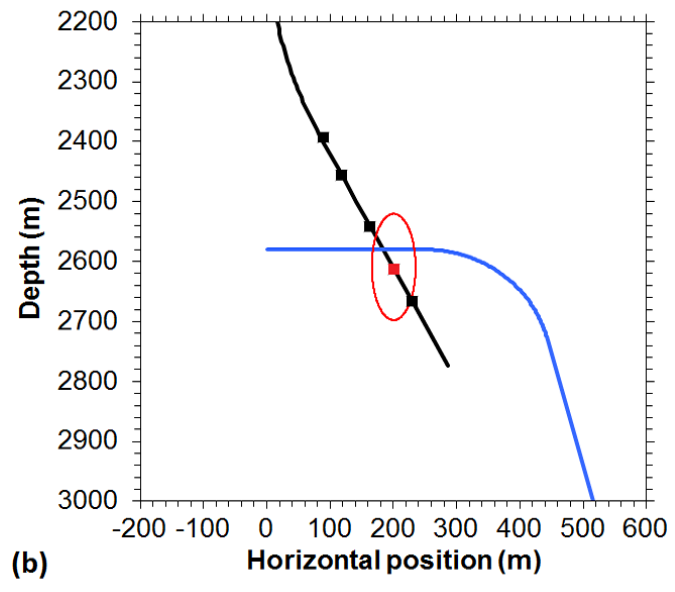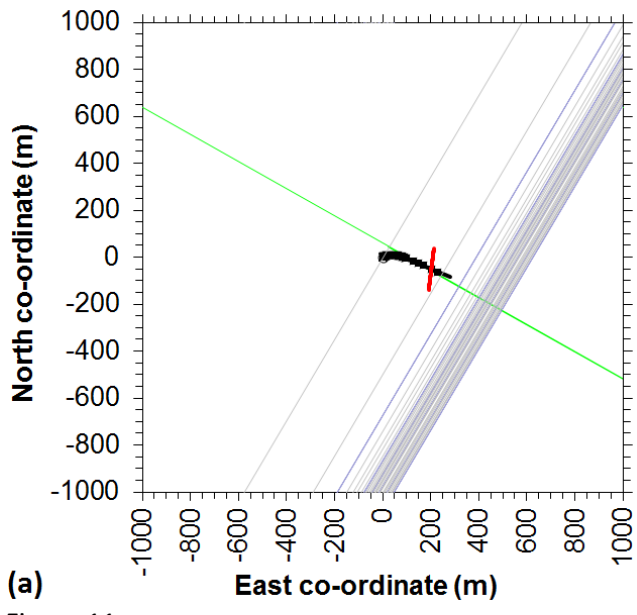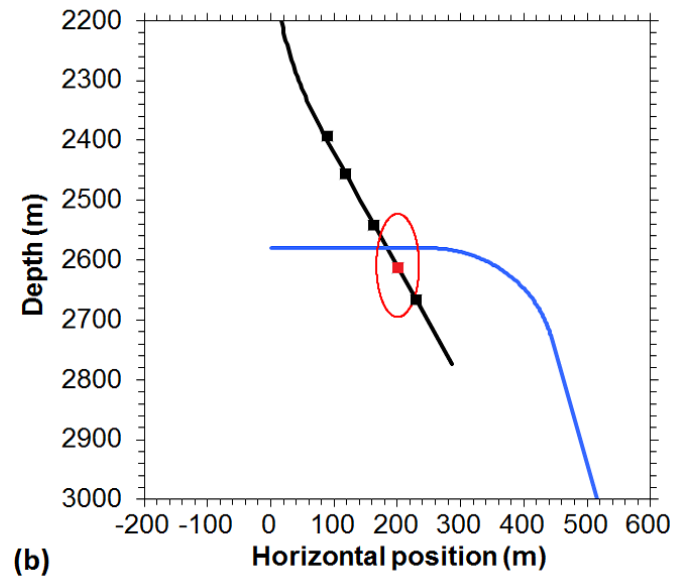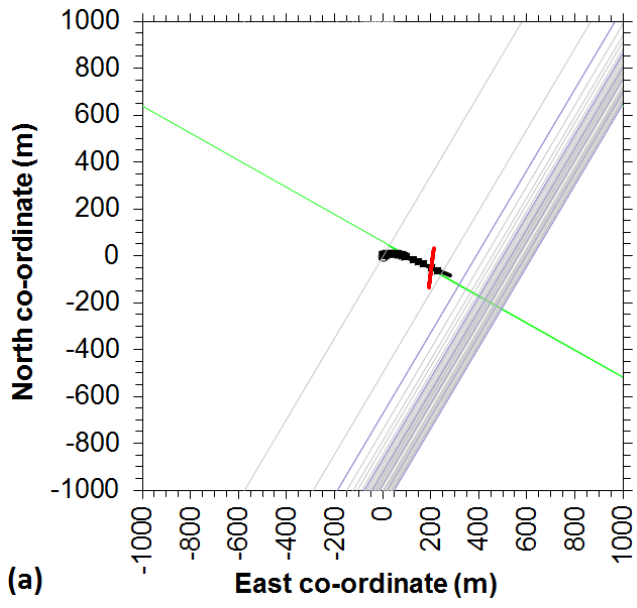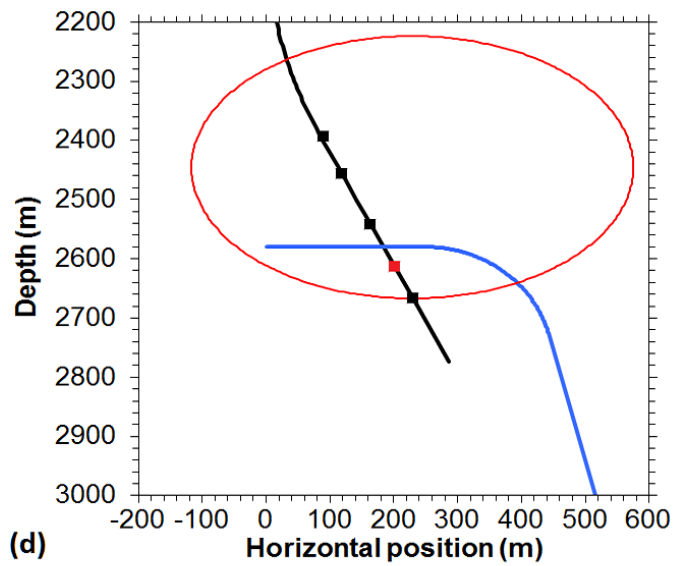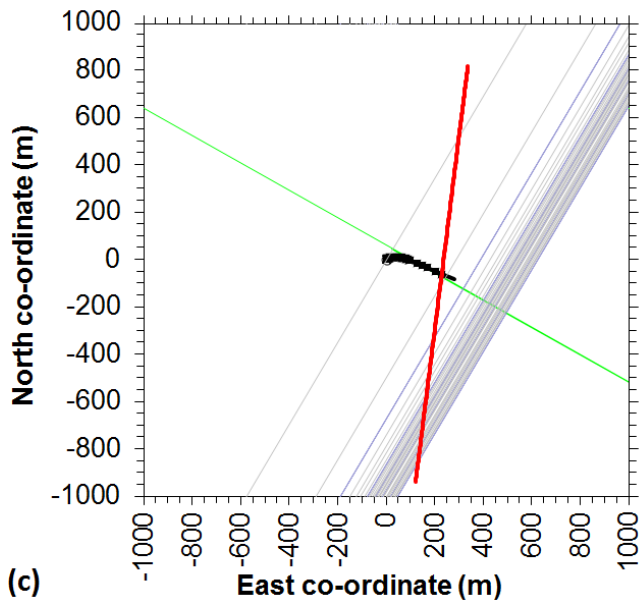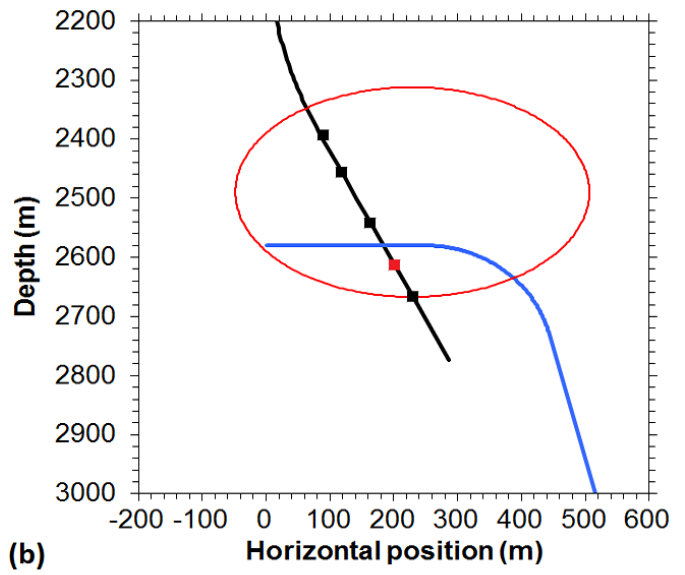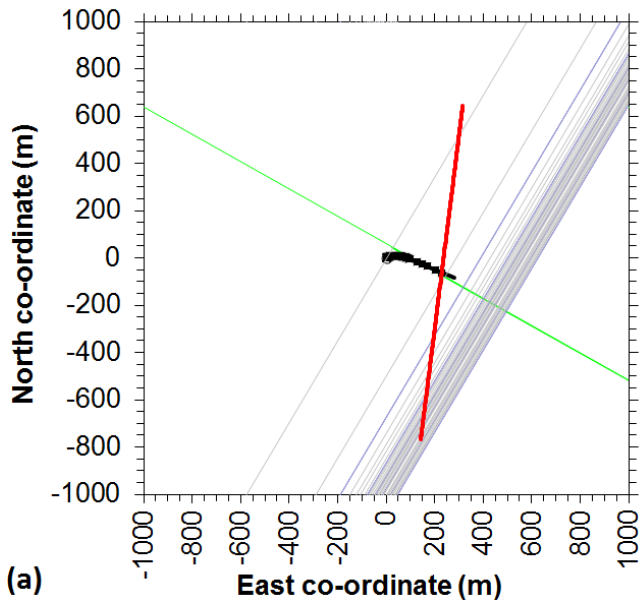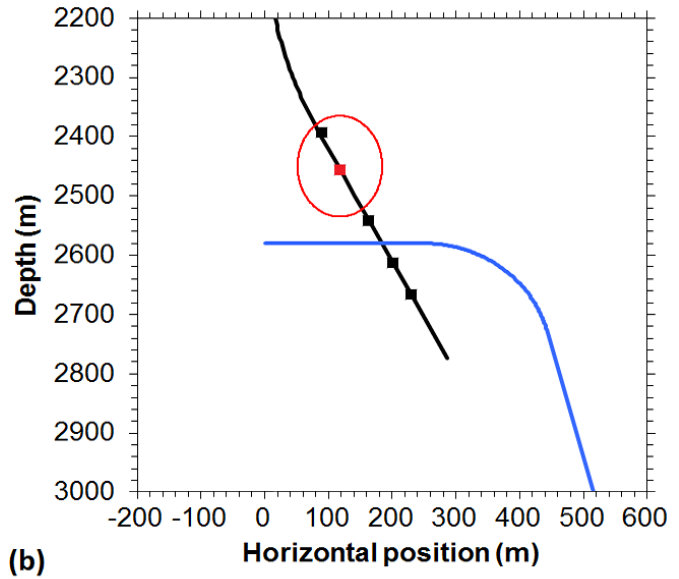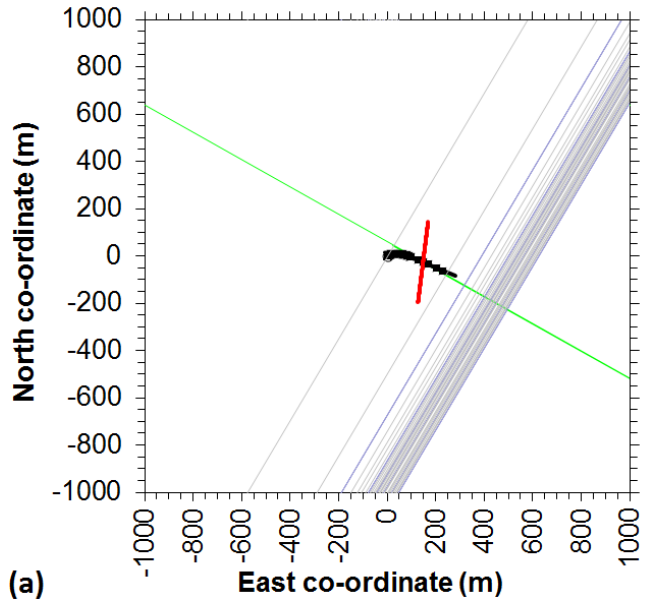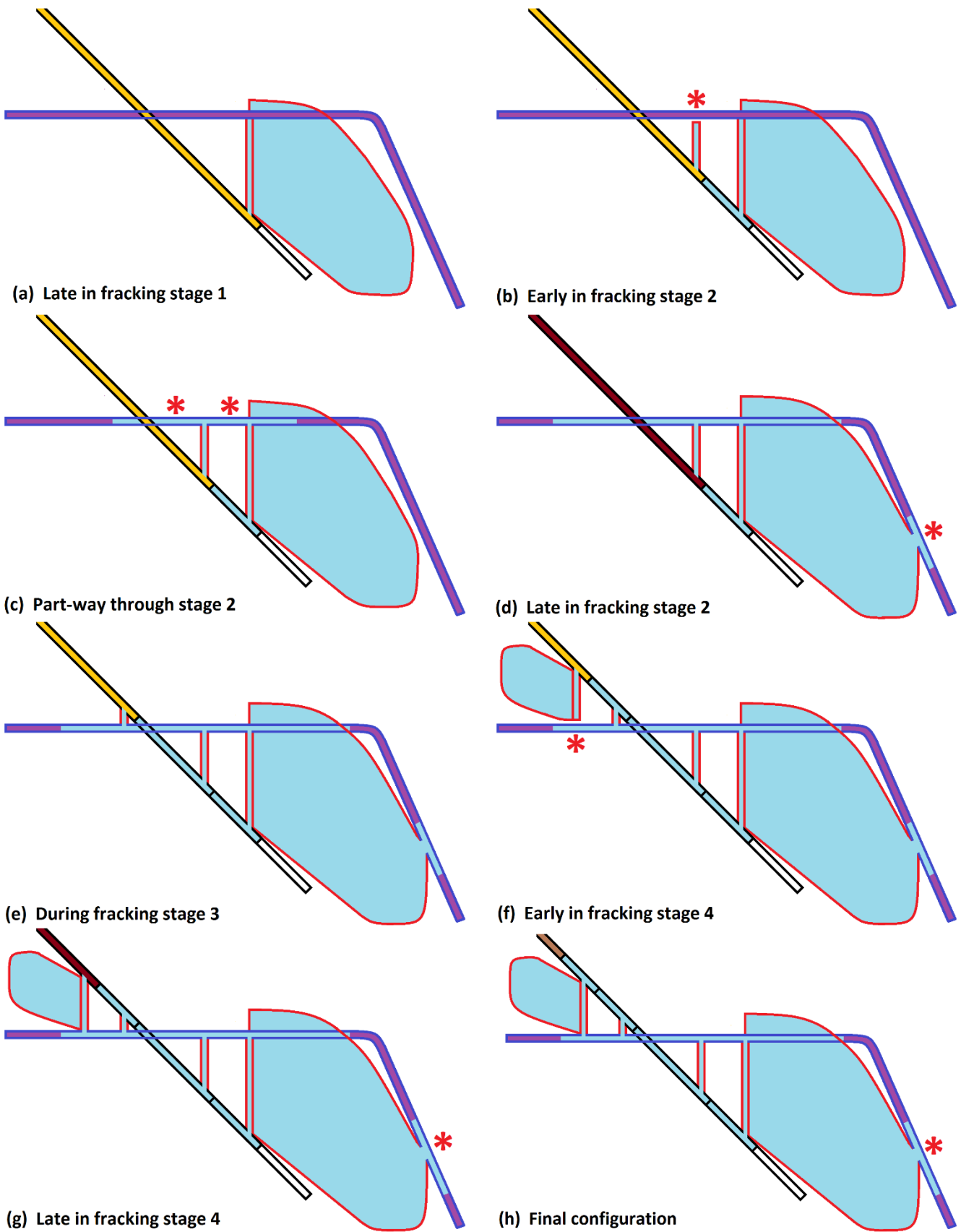
- 'Intact' patch of fault
- Patch of fault 'opened up' by fluid injection
- Induced fracture in cross section
- Induced fracture in side view
- Induced seismicity
- Well open for fluid injection
- Well hydraulically interconnected with fracture network
- Bridge plug
- Well 'shut in'
- Well plugged and abandoned
- Isolated end section of well

(i) Key

Figure 15

Table 1: Details of the Preese Hall-1 well

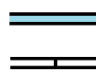| Fracking stage		1	2	3	4	5
Date [1]		28 March	31 March	9 April	26 May	27 May
Perforation cluster 1 (ft MD) [2]		8841-8850	8700-8709	8420-8429	8020-8029	7810-7819
(m MD) [3]		2695-2697	2652-2655	2566-2569	2444-2447	2380-2383
Perforation cluster 2 (ft MD) [2]		8930-8939	8730-8739	8450-8459	8120-8129	7900-7909
(m MD) [3]		2721-2725	2661-2664	2576-2578	2475-2478	2408-2411
Perforation cluster 3 (ft MD) [2]		8942-8951	8750-8759	8480-8489	8250-8259	7970-7979
(m MD) [3]		2726-2728	2667-2670	2585-2587	2515-2517	2429-2432
Plug depth	(ft MD) [4]	8991	8810	8495	8300	8000
	(m MD) [3]	2740	2685	2589	2530	2438
	(m TVD) [5]	2685	2636	2552	2499	2418
Injection depth	(ft MD) [6]	~8925	~8725	~8455	~8140	~7730
	(m MD) [3]	~2720	~2659	~2577	~2481	~2410
	(m TVD) [5]	~2667	~2613	~2541	~2456	~2393
Dip [7]		65±3°	39±2°	35±2°	61±5°	30±2°
Downdip azimuth [7]		N62°W±4°	N62°W±4°	N67°W±3°	N64°W±5°	N75°W±3°
Injection time [8]		11:40-14:40	09:15-16:15	NR	12:00-14:40	11:15-15:50
Flowback time [8]		NA	NA	NR	15:10-18:25	16:00-36:00
WHP (psi) [9]		3331	2871	301	2758	34
WHP (MPa) [3]		23.0	19.8	2.1	19.0	0.2
BHP (MPa) [10]		49.2	45.5	27.1	43.1	23.2
CP (MPa) [11]		44.1	49.8	44.5	NA	47.8
V_{I1} (bbl) [2][12]		817	590	254	502	280
V_{I2} (bbl) [2][13]		11568	14120	4777	10088	9590
V_I total (m^3) [3][14]		1969	2339	800	1684	1569
V_F total (bbl) [15]		0	0	11266	676	9600
V_F total (m^3) [15]		0	0	1791	108	1526
Proppant (10^3 kg) [2]		101	117	52	82	111
Seismicity induced? [16]		No	Yes	No	Yes	No

MD and TVD denote 'measured depth' and 'true vertical depth'. WHP and BHP denote 'well head pressure' and 'bottom hole pressure'. Notes:

[1] From Table 3 of de Pater and Baisch (2011).

[2] Depths of perforation clusters, volumes of fluid, and masses of proppant injected are from Table 2 of de Pater and Baisch (2011). Each perforation cluster consisted of 27 perforations. Note that the perforation clusters were much farther apart for fracking stages 4 and 5 than for the others.

[3] Conversions to S.I. units are from the present study.

[4] Before each fracking stage a bridge plug was inserted in the well below the depths of perforation for that stage, but above the depths perforated during previous stages, to ensure the fluid injected reached the correct perforations. Details are from Fig. 11 of de Pater and Baisch (2011). The casing shoe at the well bottom was set at 9085 ft or 2769 m (MD), below the stage 1 bridge plug.

[5] Estimated using our model for deviation of the wellbore (cf. Fig. #6), using equation (5) for points deeper than 2400 m TVD.

[6] This row lists representative averages of the depths of the perforation clusters for each fracking stage.

[7] Dip and downdip azimuth data are summarized for the depth range corresponding to the middle perforation cluster, from Table 5.1 of Harper (2011).

[8] Data on times of injection and flowback are from Figs. 21, 22, 26 and 27 of de Pater and Baisch (2011). NR denotes 'not reported' (i.e., we are not aware of any reported record); NA denotes 'not applicable'. Fig. 26 shows flowback from stage 5 still under way at 12:00 on 29 May, at which point the record ends.

[9] Well head pressure after the flowback period, from Fig. 42 of de Pater and Baisch (2011).

[10] Hydrostatic bottom hole pressure for the representative depth (TVD) of injection.

[11] 'Closure pressure' estimated from plot of G × dp/dG for the 'minifrac', by de Pater and Pellicer (2011).

[12] Volume injected during the 'minifrac' preceding the 'main frac'.

[13] Volume injected (including volume of proppant) during the 'main frac'.

[14] Sum of V_{I1} and V_{I2}.

[15] Flowback volumes V_F are from Fig. 42 of de Pater and Baisch (2011). Additional flowback of 4878 bbl or 776 m^3 of fluid occurred before the stage 3 'minifrac' took place.

[16] Stage 2 was followed by the induced earthquakes depicted in Fig. #9 as well as the largest event, at 02:34 on 1 April 2011 (local magnitude M_L 2.3), some 10 hours after the start of shut-in. Stage 4 was followed by other induced earthquakes including the second largest event, at 00:48 on 27 May (M_L 1.5), again ~10 hours after the start of shut-in. Other induced earthquakes occurred during and after stage 5; however, it is impossible to say whether the conditions causing their occurrence resulted from stage 4 or stage 5, given the brief interval between them. Earthquake details are from Galloway (2012).

Table 5: Fracture size from pressure matching using a bi-wing fracture model and a multiple fracture model with 10 branches (lower box).

Stage	z_m	L_o	H_o	W_a	z_1 top depth	base depth	centre shift + = down	V	%V	A
	(m)	(m)	(m)	(mm)	(m)	(m)	(m)	(m^3)		(m^2)

De Pater and Pellicer (2011); ten-fracture model (n=10)

Stage	z_m	L_o	H_o	W_a	z_1 top depth	base depth	centre shift	V	%V	A
1	8917	166	753	1.927	8144	8897	-252			
2	8755	94	210	6.847	8522	8732	1			
3	8495	308	452	0.892	8052	8504	-104			
4	8165	311	577	1.029	7684	8261	-122			
5	7930	384	462	0.931	7623	8085	-12			
1	2717.9	50.6	229.5	48.9	2482.3	2711.8	-76.8	892	45%	182400
2	2668.5	28.7	64.0	173.9	2597.5	2661.5	+0.3	502	21%	28900
3	2589.3	93.9	137.8	22.7	2454.2	2592.0	-31.7	461	58%	203300
4	2488.7	94.8	175.9	26.1	2342.1	2518.0	-37.2	684	41%	261900
5	2417.1	117.0	140.8	23.6	2323.5	2464.3	-3.7	611	39%	258800

De Pater and Pellicer (2011); single-fracture model (n=1)

Stage	z_m	L_o	H_o	W_a	z_1 top depth	base depth	centre shift	V	%V	A
1	8917	380	975	0.484	8018	8993	-268			
2	8755	235	739	1.124	8278	9017	21			
3	8495	607	928	0.187	7705	8633	-213			
4	8165	413	657	0.638	7676	8333	-91			
5	7930	580	757	0.345	7422	8178	-66			
1	2717.9	115.8	297.2	12.3	2443.9	2741.1	-81.7	665	34%	54100
2	2668.5	71.6	225.2	28.5	2523.1	2748.4	+6.4	722	31%	25300
3	2589.3	185.0	282.9	4.7	2348.4	2631.3	-64.9	386	48%	82200
4	2488.7	125.9	200.3	16.2	2339.6	2539.9	-27.7	642	38%	39600
5	2417.1	176.8	230.7	8.8	2262.2	2492.7	-20.1	359	23%	64100

––

Estimated dimensions of the induced fracture sets at Preese Hall, based on Table 5 of de Pater and Pellicer (2011). Parameters are: n, number of parallel fractures that are assumed to have developed; z_m, depth (MD) of the injection point; L_o, half length of the fracture (s); H_o, height of the fracture(s); W_a, average width of each of the fractures; V, estimated total volume of the fracture(s); %V, V expressed as a percentage of the volume of fluid injected (from Table 1); A, estimated total area of the fracture(s). V is calculated as $(n \times \pi/2) \times L_o \times H_o \times W_a$; A is calculated as $(n \times \pi/2) \times L_o \times H_o$, so A=V/ W_a.

; This study; single-fracture model

$V = 16 \times \pi \times Wav \times L \times H$

Integrating induced seismicity with rock mechanics: a conceptual model for the 2011 Preese Hall fracture development and induced seismicity

Rob Westaway

School of Engineering, University of Glasgow,
James Watt (South) Building, Glasgow G12 8QQ, U.K.

e-mail: robert.westaway@glasgow.ac.uk

Supplementary material

Contents:

1. Stratigraphy, structural geology, and rock-mechanical properties

Northern England is formed from a mosaic of Carboniferous sedimentary basins inset into metasedimentary 'basement', which was metamorphosed during the Lower Palaeozoic Caledonian Orogeny (e.g., Fraser et al., 1990; Kirby et al., 2000; Andrews, 2013). These basins underwent extension as a result of Dinantian (Early Carboniferous) tectonics (e.g., Fraser and Gawthorpe, 2003; Waters and Davies, 2006), followed by continued sedimentation during the subsequent 'thermal subsidence' phase of basin development in the Silesian (Late Carboniferous). The region depicted in Fig. 2 thus includes, amongst others, the Bowland, Cheshire, Cleveland, and Gainsborough Basins, all recognized as potential shale gas plays (e.g., Andrews, 2013). This resource is in hemipelagic shale that the British Geological Survey (BGS) has informally named the 'Bowland-Hodder Unit' (Fig. 2). In the Bowland Basin these rocks fall within the established Craven Group (Waters et al., 2011; Andrews, 2013); at Preese Hall the 'Upper Bowland-Hodder Unit' is equivalent to the established Bowland Shale Formation, the 'Lower Bowland-Hodder Unit' corresponding to the established Hodder Mudstone Formation (cf. Fig. 5(a)). Deposited primarily during the Visean stage (but locally also encompassing the late Tournaisian and/or early Namurian) of the Dinantian in relatively deep-water environments in normal-fault hanging-walls, these rocks pass laterally in footwall settings into the more familiar shallow-water carbonate facies that forms much of the outcrop in upland parts of northern England, such as the Yorkshire Dales and the White Peak uplands of Derbyshire (Fig. S1.1).

Thus, in the region covered by Fig. S1.1, the Bowland Basin is bounded to the NE by the South Craven Fault and subparallel North Craven Fault, which separate it from the up-faulted Askrigg Block, and to the southeast by the Pendle Fault, which also delineates the Central Lancashire High in its footwall. The South Craven Fault continues SE as the Morley-Campsall Fault (or Aire Valley Fault), which separates the Gainsborough Basin to the southwest from the Askern-Spitall High to the northeast. The aforementioned Askrigg Block is bounded to the WNW by the Dent Fault and to the NNE by the Stockdale Fault, the hanging-wall of which contains the Stainmore Basin. The latter continues eastward into the Cleveland Basin, bounded to the south by the Flamborough Head - Vale of Pickering Fault Zone with the Market Weighton High in its footwall. The Askrigg Block is underlain by Caledonian granite; this is now thought to date from the Caradocian stage of the Ordovician (e.g., Pharaoh et al., 1997; Millward, 2006), rather than the Devonian age formerly adopted (e.g., Dunham, 1974; Dunham and Wilson, 1985). The Market Weighton High is inferred to also have a granite core from gravity studies (e.g., Bott et al., 1978; Bott, 1988). The relative buoyancy of the granites beneath these
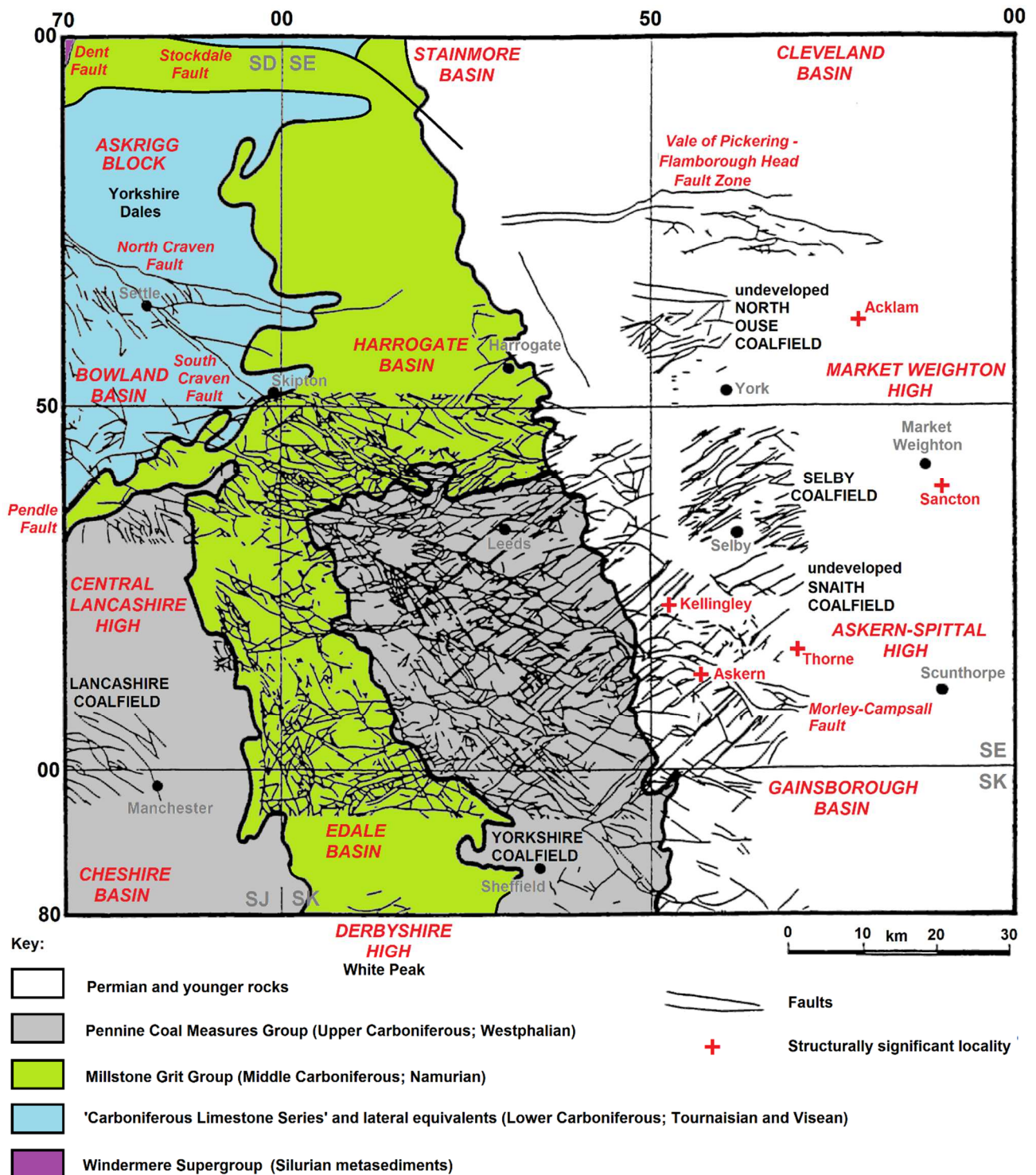
Figure S1.1. *Map of the eastern part of the area in Fig. 2, likewise indexed to the BNG, showing faults and fractures documented primarily as a result of detailed studies related to coal mining. The outcrop boundaries depicted are simplified. The Alston Block is located north of the Stainmore Basin, being bounded to the south by the Butterknowle Fault (e.g., Chadwick et al., 1995; Kimbell et al., 2010). The structural significance of each of the sites marked is explained by British Coal Corporation (1997); for example, Acklam and Sancton mark hinge zones at the northern and southern margins of the Market Weighton High. Kellingley Colliery, one of the sites thus depicted, was also the last deep coal mine in Britain, coal production there having ended in December 2015. Modified from Fig. 2.1(a) of British Coal Corporation (1997).*

and other parts of Britain has long been recognized as a major factor influencing both ancient and active patterns of vertical crustal motion (e.g., Bott, 1988; Waters and Davies, 2006; Westaway, 2017). It is traditional in Britain to associate structural trends with ancient geological events. Thus (e.g., Hills, 1966), a SW-NE orientation is regarded as 'Caledonide' and a NW-SE or 'Charnoid' orientation is associated with the concealed Caledonides beneath eastern England (e.g., Pharaoh et al., 2011). A north-south structural trend is designated as 'Malvernoid' after the Precambrian rocks of the Malvern Hills in west-central England, and a west-east trend as 'Armoricanoid' or Variscan. Although other orientations are also present, the majority of the major structures in Fig. S1.1 strike SW-NE or NW-SE, suggesting that they reflect Carboniferous reactivation of Caledonian-age basement structures (e.g., Waters and Davies, 2006). Any assessment of the conditions that might result in induced seismicity under the present-day stress field (discussed below) must consider this diversity of structural trends, and the associated multiplicity of orientations of potential planes of weakness within the crust.

In addition to these major structures, Figure S1.1 also indicates the density of faults and fractures in this region. Its coverage is uneven, there being much more detail in former coalfields and areas where the coal resource was explored but not exploited. Where no exploration or production of coal has taken place, there is a typical lack of correspondingly detailed investigation. Similar structural detail exists in the former metalliferous mining regions of the Askrigg and Alston Blocks of the central and northern Pennines (e.g., Turner et al., 1995; Fig. S1.1); however, these upthrown Carboniferous footwall blocks are not directly relevant to shale gas prospecting. The case study of the Selby coalfield, developed starting in the 1970s and discussed by British Coal Corporation (1997), is pertinent to demonstrating the influence of structural complexity on resource extraction. Shortly after coal production began in the 1980s, it was realised that this coalfield is pervasively faulted, many faults having throws below resolution limit of 1970s-era seismic reflection surveys. Repeat surveys in the 1990s, with resolution of 2 ms two-way-time or ~3 m of throw, revealed many additional faults (Fig. S1.1); faults with even small throws of this order proved to be severe impediments to the economical operation of coal-cutting machinery. Indeed, this coalfield was shut down completely by 2004 after only 121 million tonnes had been mined from a single seam, the estimated coal reserves being ~400 million tonnes from this seam and ~6000 million tonnes in total.

Despite the main phase of crustal extension in the region having ended circa the end Dinantian, many faults that had been active at this time also offset younger rocks, indicating multiple phases of subsequent minor extension and/or crustal shortening as well as the significant phase of crustal shortening during the Variscan orogeny (e.g., Waters et al., 1994; Kirby et al., 2000; De Paola et al., 2005; Waters and Davies, 2006; Pharaoh et al., 2011). It has long been recognized that coal mine records, such as those summarized in Fig. S1.1, provide much more detail than is available to the petroleum industry from seismic surveys (e.g., British Coal Corporation, 1997); these also provide information regarding the relative chronologies of slip on the different sets of faults in Fig. S1.1. It is thus evident that slip on SW-NE-striking faults was either synchronous with or younger than the youngest slip on the NW-SE-striking Morley-Campsall Fault. Other SW-NE-striking faults are themselves offset by strike-slip displacements on E-W-striking faults, which appear to indicate the most recent phase of slip and indicate a stress field orientation very different from that during the Carboniferous (see below). Similar complexities are evident in parts of northern England to the north of Fig. S1.1; mine records and geophysical surveys indicate that the most recent deformation has involved left-lateral slip on NE-SW-striking faults (e.g., Robson, 1964, 1977; Turner et al., 1995). The disposition of cave levels in the limestone uplands of the Yorkshire Dales (Askrigg Block) and White Peak uplands indicate that, since the start of the Middle Pleistocene, these regions have experienced uplift at ~0.2 mm a^{-1}, faster than in the lowland regions to the east and south (e.g., Westaway, 2009, 2015b, 2017; Bridgland et al., 2014; Westaway et al., 2015). These analyses also indicate correlations between present-day vertical crustal motions and some of the crustal blocks depicted in Fig. S1.1, for example the Cleveland Basin now appears to be uplifting faster than the Market Weighton High farther south. These patterns of progressive vertical crustal motion are also modulated by the transient isostatic effects of multiple cycles of loading and unloading by ice sheets (e.g.,

Bridgland et al., 2010). The abundant evidence now available for widespread active crustal deformation within Britain bears upon how one interprets *in situ* stress data within the crust (see below).

A significant feature of the Preese Hall-1 case study was the deformation to the wellbore noted following the largest of the induced earthquakes (e.g., de Pater and Baisch, 2011). Caliper tool measurements reported by de Pater and Baisch (2011) indicate that this deformation was concentrated between depths (MD) of 8502 and 8626 ft or 2590-2636 m, which correspond to ~2552-2593 m (TVD) (the procedure used in this study for converting between these two measures of depth for this well is explained in the main text); this deformed interval is identified as a white band on the well track in Fig. 4. It occurs within rocks that were thought at the time to be the 'Hodder Mudstone'; this part of the sequence is evidently thinner in the vicinity of the Preese Hall-1 well than elsewhere (Fig. 4), indicating that it has experienced localized deformation. Weak zones sub-parallel to the bedding were indeed recognized in the Preese Hall-1 dataset by de Pater and Baisch (2011) and Harper (2011) and might well have accommodated the observed local thinning by bedding plane slip. Harper (2011) indeed noted that these weak zones make the mechanical properties of this formation anisotropic.
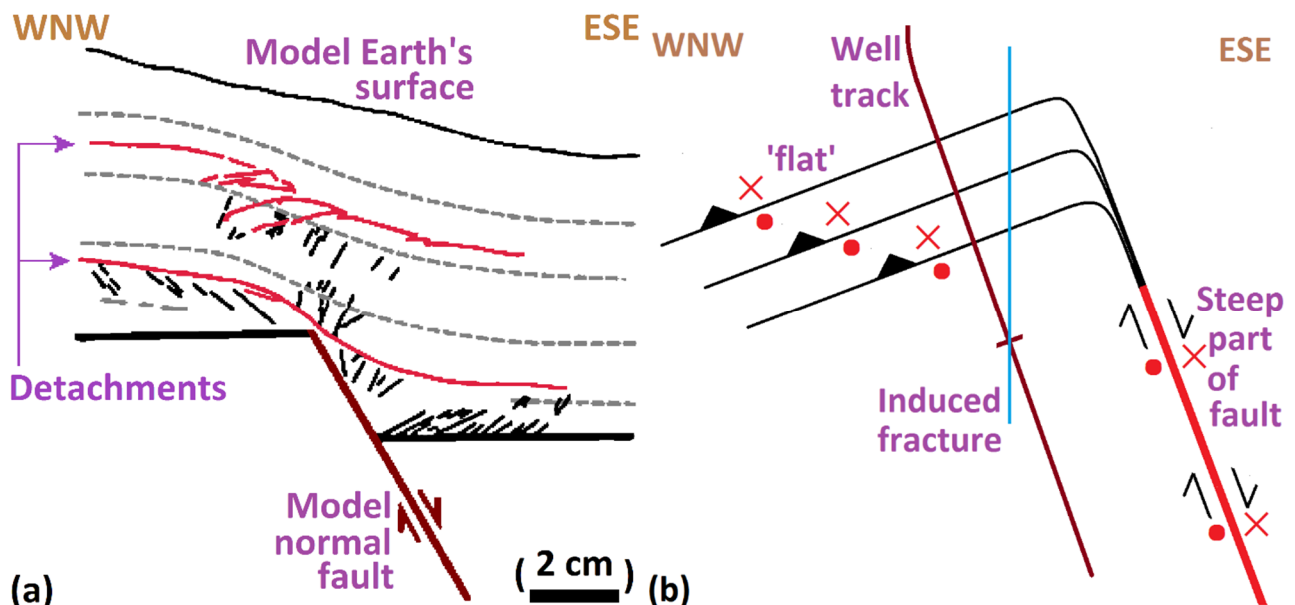

Figure S1.2. *Potential schematic representations, not to scale, but spanning vertical and horizontal distances of up to several hundred metres, of the geometry of faulting associated with the induced seismicity and related wellbore deformation at Preese Hall in 2011. (a) Modified from Fig. 1(b) of Ferrill et al. (2007), based on Fig. 8(f) of Withjack et al. (1990). This diagram, showing development of sub-horizontal 'detachments' with top-to-the-right sense of shear, is based on analogue modelling (at the scale indicated) using a rheologically layered model (with dashed lines denoting 'form lines' within the model, which were horizontal prior to fault slip), in which the detachments were simulated by placing pairs of acetate sheets within the model. Note also the presence in the model of the free surface representing the Earth's surface, which is a requirement for this particular style of deformation to occur. (b) Modified from Fig. 1 of Westaway (2016b); unlike that in (a), this variant does not require an adjacent free surface. The predominant sense of slip on this model fault plane was left-lateral, indicated with dot and cross symbols to denote motions in and out of the section plane, together with a minor component of normal slip, indicated by paired arrows. Curved lines extending from the updip end of the steep part of the fault indicate schematically the 'horsetail splay' or 'contractional imbricate fan' forming the 'flat' at its termination, which is inferred on the basis of the 'bedding plane slip' that caused the deformation to the Preese Hall-1 wellbore. The strike-slip component of motion on the steep part of the fault is thus accommodated by top-to-the-NNE bedding plane slip on this 'flat', again represented by dot and cross symbols, whereas its normal component of slip is accommodated by contraction, perpendicular to the bedding planes, represented by chevron symbols.*

It is shown in the main text that the presence of this subhorizontal zone of disrupted stratigraphy, or zone of weakness, at ~2550-2590 m depth (TVD), is key to understanding why the Preese Hall project 'went wrong'. The calculations indicate that high net pressure of fracking fluid 'opened' this structure, resulting in horizontal migration of fracking fluid. It is thus of interest to consider why this zone is there; this bears, for example, upon the probability of repetition of similar issues during future fracking projects. One possibility, as Harper (2011) has suggested, is that the zone marks a syn-sedimentary submarine landslide, Gawthorpe and Clemmey (1985) having documented such structures elsewhere in the Bowland Shale. However, this would imply that the presence of this zone near a steep normal fault is coincidental, implying that the co-occurrence of coseismic slip and wellbore deformation was, likewise, a coincidence, and thus lacking in wider significance. A second possibility, after Ferrill et al. (2007), is that the zone is a 'detachment', mechanically and geometrically related to slip on the adjacent steep fault, as illustrated in Fig. S1.2(a). However, the Ferrill et al. (2007) scenario requires a free surface (i.e., the Earth's surface) in close proximity, which it is not. Figure S1.2(b) illustrates a variant of this, suggested by Westaway (2016b), in which the subhorizontal 'flat' marks the upward termination of the steep fault in a manner that requires no related deformation at shallower depths and, thus, no adjacent free surface. The inferred geometry resembles a conventional 'horsetail splay' (e.g., Sylvester, 1988) or 'contractional imbricate fan' (e.g., Woodcock and Fischer, 1986) fault termination. From consideration of the magnitude (2.3) and, thus, seismic moment, of the largest Preese Hall induced earthquake, a coseismic displacement of ~10 mm can be estimated (cf. Westaway and Younger, 2014); it is envisaged, in terms of the scheme in Fig. S1.2(b), that beyond the up-dip limit of the steep part of the fault, this shear displacement was partitioned across the various planes of weakness within the 'flat'.

One reason why the possibility that the wellbore deformation was mechanically related to the induced seismicity was not recognized sooner was that the Preese Hall-1 operator (whose views are reflected in the Clarke et al., 2014, paper) located the seismicity well east of the wellbore (Figs 1, 4). This argument was superseded by the realisation of the mistakes in their paper and the resulting adjustment of the position of the seismogenic fault closer to the wellbore, although the patch of it that slipped in the largest induced earthquakes was to the south (Westaway, 2016a; Fig. 1). Another reason was because de Pater and Baisch (2011) were unable to identify a clear conceptual link between the seismogenic fault and the wellbore deformation, notwithstanding the potential links now suggested (Fig. S1.2). Clarke's (2016) comment (cf. Baisch and Vörös, 2011) that 'all of the evidence collected to date supports the observation that the wellbore was within 300 m of a fault but does not intersect it' is therefore debateable, given the clear possibility that the 'flat' in which the wellbore deformation occurred was part of the upward fault termination (Fig. S1.2(b)) or otherwise directly related to this fault (Fig. S1.2(a)). For illustrative purposes within the present work, it will be assumed that this 'flat' is, indeed, the updip termination of the steep fault, in the sense indicated in Fig. S1.2(b). However, from the point of view of the geomechanics, it is immaterial whether it might instead be a 'detachment', related to the fault as in Fig. S1.2(a), or the sole of a submarine palaeo-landslide or a zone of non-cohesive bedding planes that developed for some other reason, coincidentally located near the adjacent fault.

Only limited information is currently available on the mechanical properties of Bowland Shale. Carter and Mills (1974) determined 2-14 GPa for the Young's modulus, 1-8 MPa for the tensile strength S_T and 2-12 MPa for the cohesion S_C, for 24 samples of Middle Carboniferous (Namurian) mudstone from sites in northeast England, which might represent analogues for the Bowland Shale. Harper (2011) summarized results of geomechanical testing of 9 samples of Bowland Shale recovered from the Preese Hall-1 well just below the shallowest perforations for stage 4 of the fracking. These results indicate shear modulus μ 10-20 GPa, bulk modulus 21-52 GPa, and Poisson's ratio ν 0.14-0.30. These elastic moduli are thus rather higher than for Namurian mudstone, suggesting that the latter may not be a good analogue for the Bowland Shale after all (cf. Westaway and Younger, 2014). Harper (2011) also reported the Young's modulus, derived from well logging, for a ~500 m thickness mostly within the Bowland Shale. This varies from ~25-70 GPa, thus broadly consistent with the aforementioned measurements of μ and ν, with a typical value of ~60 GPa; the principal departure from this value, a decrease to ~25-30 GPa, occurs over ~8660-8750 ft (MD) or ~2595-2620 m (TVD)

and coincides with the subhorizontal 'flat' that plays a significant role in the geomechanical model developed in this study. Harper (2011) did not report any measurements of cohesion for 'intact' rock but inferred that pre-existing fractures within the Bowland Shale at Preese Hall are cohesionless (i.e., in the direction parallel to fractures, $S_C=0$), indicating that this shale (unlike many others) does not ever 'bond back together' once fractured. Most recently, Gao et al. (2015) have reported analyses of what they described as 'typical gas shale rocks in northeastern Ohio'. They did not note, however, whether their samples were of the Carboniferous Marcellus Shale or of older (Lower Palaeozoic) shale. They nonetheless determined a typical density of their samples, whose properties were strongly anisotropic, as 2503 kg m^{-3}. Two groups of samples yielded mean values for tensile strength of 7.4 and 9.1 MPa in the direction perpendicular to the bedding, with bedding-parallel values estimated as 300-360 times smaller (i.e., ~0.02-0.03 MPa). Gao et al. (2015) also measured seismic wave velocities (V_P and V_S) but did not derive elastic properties from these. They determined both V_P and V_S for nine samples, but for three of these the V_P/V_S ratios are so low as to require negative values of ν. Discounting these three data, one obtains $V_P/V_S=1.89\pm0.79$ ($\pm1\sigma$) and $\nu=0.27\pm0.15$ ($\pm1\sigma$) for the others, the latter result requiring the standard formula

$$\nu \equiv \frac{(V_P/V_s)^2 - 2}{2(V_P/V_s)^2 - 2}, \tag{S1.01}$$

(e.g., equation (A4) of Westaway and Younger, 2014). Although there is much scatter in these data, the results are nonetheless of some value. Of course, to be ideally useful for the present study, measurements such as these should really be made under conditions that simulate the temperature and state of stress at depth and not under ambient conditions in the laboratory. For comparison, using in situ logging, the typical density of the Bowland Shale at Preese Hall was reported as ~2620 kg m^{-3} in Fig. 2 of Baker Hughes (2011).

Currently, relatively little quantitative information is available on the porosity and permeability of Bowland Shale, although many workers have reported the latter parameter as 'low'. As an example, iGas (2014) reported porosity in the range 1.1-2.6% and typical permeability ~0.03 μD (~3×10^{-20} m^2) for Bowland Shale in their Irlam-1 (or Ince Moss; SJ79NW314) well located (at SJ 73615 97552) west of the city of Manchester (Fig. 2). Rutter and Mecklenburgh (2017) report results of more detailed analysis of the shale from this borehole, including porosity 1.9$\pm$0.4% and pressure-dependent permeability. They demonstrate that permeability decreases with effective confining pressure P_e (the difference between confining pressure and pore pressure), being ~0.1 μD for $P_e=40$ MPa, ~0.04 μD for $P_e=60$ MPa, and ~0.01 μD for $P_e=80$ MPa. One might envisage a similar pressure-dependence of permeability of the shale at Preese Hall, but currently there are no published data to substantiate this. Furthermore, given that the Preese Hall site is in deep marine deposits near the axis of an Early Carboniferous depocentre (e.g., Fraser and Gawthorpe, 2003), whereas the Irlam-1 site is in an intra-basinal shallow-marine 'high' (the 'Holme High') where the sediments are generally coarser-grained (iGas, 2014), lower permeability might be anticipated at Preese Hall.

2. Regional state of stress and its implications

Establishing *in situ* stress is key to determining how close to failure any particular fault is. It is well established that, typically in northern England, the maximum principal stress is roughly north-south, with the minimum principal stress roughly east-west and the intermediate principal stress near-vertical (e.g., Evans and Brereton, 1990; Chadwick et al., 1996; Cartwright, 1997; Baptie, 2010; Heidbach et al., 2010), although quite abrupt local variations are nonetheless apparent. The high differential stress $\Delta\sigma$ measured in the Preese Hall-1 well (Fig. 5(b); see also below) is thus no surprise; high $\Delta\sigma$ has long been apparent in Britain, for example from *in situ* stress measurements in coal mines (e.g., Cartwright, 1997; Mark and Gadde, 2008) and at the former Rosemanowes geothermal energy project site in Cornwall (e.g., Pine and Batchelor, 1984; see also below). It has subsequently been realised that the differential stress is sufficient for major faults, causing localized surface deformation, to be active in various parts of Britain (Westaway et al., 2006; Westaway, 2010; Harding et al., 2012); it was already established that the transient stress field during ice unloading at the end of the last ice age caused large earthquakes (e.g., Ringrose, 1989; Stewart et al., 2001). The Kingdon et al. (2016) synthesis of stress field orientations for northern England, based on borehole image

logs, presents results that are similar to previous works, but does not include the underlying raw data and does not address magnitudes of $\Delta\sigma$.

The 1980s Rosemanowes project, which attempted to extract heat using hydraulic fracturing to create paths for water flow through granite, provides a graphic illustration of the need to consider the local stress field before embarking on subsurface engineering works. As Pine and Batchelor (1984) explained, this granite has a set of joints oriented at azimuths ~N20-30°W-~S20-30°E. The existing literature (e.g., Richardson and Solomon, 1979; Froidevaux et al., 1980) reported that in northern France, earthquake focal mechanisms and a few *in situ* stress measurements indicate that the minimum principal stress is roughly subperpendicular to this joint set in Cornwall. However, it was already known that focal mechanisms only provide a rough indication of stress orientation, because the minimum principal stress can lie anywhere within the compressional quadrant (McKenzie, 1969). Nonetheless, it was felt that the design of the Rosemanowes injection and production wells could proceed, without supporting local *in situ* stress measurements, assuming that the injection would open tensile fractures parallel to the existing joint set. It was subsequently found that the induced fractures developed in a different direction, opening via a combination of tensile and shear deformation. Later measurements established that the present-day minimum principal stress is oriented N40°E-S40°W, thus at ~60-70°, rather than 90°, to the joint set; this mismatch, plus the combination of high $\Delta\sigma$ (representative values, at 2 km depth, are maximum, intermediate and minimum principal stresses 71, 52, and 30 MPa, the intermediate principal stress being vertical), was sufficient to make the project to 'go wrong' (Pine and Batchelor, 1984). Despite attempts at redesign, this project was subsequently abandoned, having never produced useable quantities of thermal water (e.g., Richards et al., 1994; Parker, 1999). Development of geothermal energy in the UK was set back for a generation and the perception was thus created, which persists in some quarters (e.g., King et al., 2015), that it is such an inherently 'risky' technology it has no significant potential role in any future renewable energy mix. It is nonetheless evident that the failure of the Rosemanowes project involved narrow margins; had the actual stress field been oriented a little closer to what had been assumed during the project design, it might have worked, and the U.K. might thus now be a leading nation in geothermal energy. The present analysis demonstrates that the Preese Hall project also 'went wrong' only by a narrow margin; this has only become apparent following detailed calculations regarding the state of stress.

Other *in situ* stress data for Britain have been compiled by GFZ (2015) and illustrated on maps many times (e.g., Chadwick et al., 1996; Baptie, 2010). Some sites indicate very high $\Delta\sigma$, an example being the borehole at Morley Quarry near Shepshed, Leicestershire (~52.76°N ~1.30°W; SK 473 183), where, at 1520 m depth, the maximum and minimum principal stresses have been determined (using hydraulic fracturing) as 50.9 and 18.7 MPa (e.g., Chadwick et al., 1996). The high $\Delta\sigma$, 32.2 MPa, at such a shallow depth can be withstood since the rocks are strongly cohesive, being Precambrian quartzite of the Charnwood Forest inlier. Furthermore, the azimuth of the maximum principal stress at this site is reported as N89°W-S89°E (GFZ, 2015), thus subperpendicular to what is typical for Britain (e.g., Baptie, 2010; Heidbach et al., 2010), thereby demonstrating the irregularity of the local stress field (see below). In summary, the high $\Delta\sigma$ measured at Preese Hall (Fig. 5(b)) is precisely what one expects from the regional context.

Musson (2007) claimed that 'there is no continuing active deformation' in Britain and, therefore, no point in attempting to identify individual active faults. This view seems to be based on the notion that the seismicity of Britain is releasing elastic strain energy that had been stored by ancient crustal deformation processes, with no accumulation of elastic strain energy; each earthquake thus de-stresses a patch of fault and so no further events will occur there. This paper post-dates (but does not cite) the Westaway et al. (2006) discovery of the first onshore active fault in Britain, and was therefore immediately obsolete on publication; this fault has evidently slipped many times during the Holocene, let alone during the Pleistocene, not just in the one historical earthquake associated with it. The older literature on the seismicity of Britain indeed documents many earthquakes large enough to have been felt, which occurred in close proximity to fault zones that are known from the geological record, and evidently each involved slip on one of the faults within the respective

zones. Onshore instances relevant to northern England include (with supporting data from http://www.quakes.bgs.ac.uk/historical/query_eq/): the Wensleydale earthquake (M_L 4.4) of 14 January 1933, for which the epicentre (reported by Rowland, 1933; circa SD 903 894) adjoins the Stockdale Fault; the Skipton earthquake (M_L 4.8) of 30 December 1944, for which the epicentre (reported by Versey, 1948, 1949; circa SD 988 404) adjoins the South Craven Fault; and the Kirkby Stephen earthquake (M_L 4.1) of 9 August 1970, for which the epicentre (reported by Browning and Jacob, 1970; circa NY 792 130) adjoins the intersection of the Pennine, Dent and Butterknowle faults. The latter event, which Browning and Jacob (1970) regarded as the largest (their magnitude 4.9) to have occurred onshore in Britain since magnitude determinations began in 1935, was indeed attributed by these authors to slip on the southern part of the Pennine Fault. Furthermore, the North Sea earthquake of 7 June 1931 (M_L 6.1 according to Musson, 2007) occurred ~100 km east of Flamborough Head (circa TB 243 558 according to Versey, 1939), within the offshore continuation of the Vale of Pickering – Flamborough Head Fault Zone. This fault zone has recently gained recognition as playing a significant role in the active crustal deformation of Britain, since it forms the southern boundary of the part of northern England that is experiencing relatively rapid uplift (Bridgland et al., 2014; Westaway et al., 2015; Westaway, 2017). Contrary to Musson's (2007) stated view, crustal deformation is evidently widespread, at laterally varying rates, across Britain and no doubt both responds to and contributes to the observed variability in the sense of stress.

Although *in situ* stress measurements (including the magnitudes and orientations of the principal stresses) were made in the Preese Hall-1 well before fracking began in 2011 (Fig. 5(b)), nothing has been reported to establish that they were used in any assessment of the consequences of the fracking prior to this taking place. However, notwithstanding the report by Baker Hughes (2011) of the maximum principal stress azimuth N7°W-S7°E at Preese Hall from World Stress Map (WSM) data, recent WSM outputs (e.g., Heidbach et al., 2010) in fact report the maximum principal stress oriented circa N35°W-S35°E in northwest England. Furthermore, the raw WSM data (GFZ, 2015) indicate that such outputs are based on interpolation between sparse data of diverse orientations. Thus, for example, at Burton-in-Kendal in SE Cumbria (circa SD 538 785; ~46 km from Preese Hall to ~N21°E), GFZ (2015) notes a measurement of the maximum principal stress azimuth as N13°E-S13°W. Conversely, at Sellafield in west Cumbria circa NY 054 037; ~75 km from Preese Hall to ~N35°W), GFZ (2015) lists nine measurements of the maximum principal stress azimuth from which Westaway (2016a) determined a mean of 156±6° (±2s) or N24±6°W-S24±6°E (±2s). Thus, the maximum principal stress azimuth varies significantly across this region, making it essential to rely on local measurements from the Preese Hall-1 borehole rather than inferences using data from more distant localities. The view has nonetheless been repeatedly stated (e.g., Müller et al., 1992; Heidbach et al., 2010) that, abrupt local variations being absent, the stress field in Britain is determined by boundary conditions resulting from the motions of adjoining plates. On the contrary, the abruptness of the observed local variations in the stress tensor orientation suggests strongly that this argument is wrong, as might well be expected from the recent analyses (e.g., Westaway et al., 2006; Westaway, 2009, 2010, 2015a, 2016a; Harding et al., 2012) which infer that the stress fields in particular localities depend on local conditions, such as the local isostatic balance between sedimentation and erosion. Future assessments to inform shale gas or other developments should therefore not use the argument that the stress field depends only on plate motions but should instead establish it using local evidence.

Regarding the stress field orientation at Preese Hall, in addition to the aforementioned Baker Hughes (2011) dataset, previous analyses of local measurements have given the maximum principal stress azimuth as ~187 or 188° from drilling-induced tensile fractures (Harper, 2011), with a combined dataset of borehole breakouts and drilling-induced tensile fractures giving 188±16° (Harper, 2011). Westaway (2016a) determined mean values of 176±5° (±2s) or N4±5°W-S4±5°E (±2s) for the Baker Hughes (2011) dataset and of 187±3° (±2s) or N7±3°E-S7±3°W (±2s) for the Harper (2011) dataset. These two estimates therefore differ significantly (at a 95% confidence level). Others (e.g., Roche et al., 2015) have noted that the state of stress elsewhere shows significant vertical variations within stratigraphic sequences in which one formation undergoes fracking. It is thus preferable to adopt, for the purpose of geomechanical analyses of the Preese Hall fracking, the result

based on the Harper (2011) dataset, since these data originated from the depth range where the fracking was undertaken, whereas the Baker Hughes (2011) dataset was from shallower depths (Fig. 5(b)). Since hydraulic fractures develop in any isotropic rock in the plane perpendicular to the minimum principal stress, it is expected that these propagated away from the Preese Hall-1 well in the vertical plane oriented N7$\pm$3°E-S7$\pm$3°W ($\pm$2s) (Fig. 1).

The present analysis also requires magnitudes of the principal stresses at Preese Hall. Cuadrilla (2014, p. 49) reported that at 2440 m depth the maximum, intermediate and minimum principal stresses are 73.4 MPa, 62.2 MPa and 43.6 MPa. These values were taken as definitive by Westaway (2015a, 2016a), since an accompanying diagram (Fig. 12 of Cuadrilla, 2014) gave the impression of a concentration of data from this depth and stated that these data came from de Pater and Baisch (2011). It was thus assumed that this Cuadrilla (2014) diagram was obtained by numerically integrating the graphs of stress gradients in Fig. 20 of de Pater and Baisch (2011). However, it is now evident that the stress 'data' reported by Cuadrilla (2014) are in fact a mixture of measurements and predictions. Moreover, no actual data were reported by de Pater and Baisch (2011) from 2440 m or 8005 ft depth. As far as can now be established, the outputs presented by Cuadrilla (2014), which Westaway (2015a, 2016a) treated as 'data', are indeed predictions obtained by numerically integrating the de Pater and Baisch (2011) stress gradient graphs. These data were plotted by Cuadrilla (2014) at depth intervals of 305 m, not because that is where measurements were made, but because that is 1000 ft, the grid interval on the vertical axis of the original de Pater and Baisch (2011) diagram, implying that Cuadrilla (2014) might not have incorporated into their analysis variations in the stress gradients within these intervals. This supposition was checked by numerically integrating these graphs, thus obtaining Fig. 5(b). It is therefore evident (by comparison with Fig. 2(b) of Westaway, 2016a) that the portrayal of these stress data by Cuadrilla (2014) is indeed incorrect, most likely for the reason outlined above. The present analysis gives best estimates of 64.38 MPa, 55.23 MPa and 39.88 MPa for the maximum, intermediate and minimum principal stresses at 2440 m depth (TVD), rather different values from those reported by Cuadrilla (2014); the corresponding values at 2400 m are 63.26 MPa, 54.27 MPa and 39.20 MPa.

3. Theory for fluid injection

The present analysis requires the variations in pressure of the injected fluid at each point of injection. Calculations are necessary here, as these values of bottom hole pressure (BHP) were not measured but have to be calculated from other information, including measurements of well head pressure (WHP). The magnitude of the minimum principal stress, σ_h, at the appropriate depth, from equation (3) can be subtracted from the calculated BHP to determine the net pressure p_o of the injected fluid at its injection point, as a starting point for the calculations relating to hydraulic fracture development (in section 4 of this supplementary material).

From Lyons et al. (2009, p. 167), or other sources, the pressure drop ΔP in a fluid of density ρ flowing with velocity V along a cylindrical channel of length ΔL, vertical extent ΔZ and diameter D, is given by the continuity equation

$$\Delta P = \pm \rho\, g\, \Delta Z + \frac{f\, \rho\, V^2}{2\, D}\, \Delta L \qquad \text{(S3.01)}$$

where f is the Darcy-Weisbach friction factor for the flow regime and g is the acceleration due to gravity. The $\pm$ sign refers to the vertical component of flow; it is + if upward and − if downward. In the limit of V=0 this equation simplifies to the standard condition for hydrostatic equilibrium; it follows (for a given pressure at the Earth's surface) that the pressure at depth in a fluid that is moving downwards will be less than if the fluid were stationary. The value of f itself depends on the Reynolds Number, Re, of the flow, where

$$Re \equiv \frac{V\, D\, \rho}{\eta} \qquad \text{(S3.02)}$$

η being the (dynamic) viscosity of the fluid. In general, if Re < ~2000, the flow is laminar, whereas at higher Re it is turbulent. For laminar flow, f takes standard values as a function of Re (e.g., McKeon et al., 2004). However, for turbulent flow, f also depends strongly on the roughness of the surface of the cylindrical channel, being markedly higher the rougher this is. Roughness, Λ, is itself defined as

$$\Lambda \equiv \frac{\varepsilon}{D} , \tag{S3.03}$$

where ε is the characteristic height of surface irregularities. For the steel used to manufacture well casing, ε is typically ~0.016 mm (e.g., Wan, 2011, p. 131; Fekete Associates, 2013).

de Pater and Baisch (2011) reported the external diameter of the Preese Hall-1 well casing as 5.5 inches at the depths of injection. The internal diameter, D, is thus estimated as 5 inches or 127.3 mm, assuming a standard specification of casing (Hirschfeldt, 2016). It follows from equation (S3.03) that Λ was ~1.3×10^{-4} for this casing. One may look up f for this value of Λ and any given value of Re on a standard 'Moody Diagram' (Moody, 1944) for input into calculations using equation (S3.01).

To model the variation over time of the density of the material within the well, due to the injection of proppant, the distance between the wellhead and the well-casing perforations has been subdivided into ten sections of equal length. The density of the proppant entering each of these sections at each time step is assumed to apply throughout this section. No attempt has been made to model the effect of self-compression on the density of water, however. From standard theory, this effect $\Delta\rho$ for a change in pressure ΔP can be approximated as

$$\Delta\rho = \frac{\rho_o}{B} \Delta P , \tag{S3.04}$$

where ρ_o is the initial density and B is the bulk modulus of water. Since B is large (2.15 GPa) this effect is small, amounting to 12.3 kg m^{-3} or just over 1% for a pressure increase of 26.5 MPa (corresponding to a depth increase of 2700 m; cf. Fig. 5(a)). The effect of thermal expansion of water, which (for a temperature rise to ~50 °C) will cancel the effect of self-compression, has also not been incorporated.

One expects injection of fracking fluid to be highly turbulent, to keep the proppant in suspension. Preliminary calculations assuming a representative value of η of 10^{-3} Pa s, for water at 20 °C, for representative rates of fluid injection reported by de Pater and Baisch (2011), indicate typical values for Re of ~2×10^6, confirming that the flow was indeed highly turbulent. With Re ~2×10^6 and Λ ~1.3×10^{-4}, the Moody (1944) Diagram indicates f ~0.012. However, calculations on this basis for stage 1 of the PH1 fracking result in BHP lower than the measured minimum principal stress (Fig. 6(b)), which would imply a negative net pressure, implying that that the fluid at depth was insufficiently pressurized to hold a hydraulic fracture open. Since fractures evidently developed (because fluid was injected into the rock mass surrounding the borehole) this combination of parameter values is mutually inconsistent; the data available for stage 1 indicate that f can have been no higher than ~0.01.

Heating of the fluid during injection, lowering its viscosity, might explain this inconsistency. Given the thermal conductivity of the local stratigraphy (Fig. 5(a)) and the regional heat flow (e.g., Downing and Gray, 1986; Rollin, 1995; Busby et al., 2009, 2011), ~80 °C temperatures are expected at the ~2600-2700 m depths of injection. Water is roughly one third as viscous at 80 °C compared with 20 °C (viscosity 0.355×10^{-3} Pa s at 80 °C); from equation (S3.02), Re values of ~6×10^6 might thus result. However, the Moody (1944) Diagram indicates that this would only reduce f from ~0.012 to ~0.0115. A related issue concerns the use of a friction reducer in the PH1 well; this has been reported informally, but no details have been made public. The Moody (1944) Diagram indicates that a perfectly smooth wellbore would have f ~0.0105 for Re=2×10^6 or f ~0.0087 for Re=6×10^6. The latter value is low enough to account for the pressure data; the combination of friction reducer use and heating of the injected fluid can thus account for the inconsistency, predicting a BHP high

enough to maintain a positive net pressure, sufficient to hold a fracture open, given the estimate of σ_h (using equation (3)) at the depth of injection for fracking stage 1 (Table 1).

4. Theory for hydraulic fracturing

The science of fracture mechanics was pioneered at the University of Glasgow by Sir William Rankine (e.g., Rankine, 1843, 1858). Subsequent refinements to general theory include the works of Griffith (1921, 1924), Sneddon (1951), Eshelby (1957), and Irwin (1957). Modelling of the development of hydraulic fractures has since become an extensive field, including the emergence of 'industry standard' procedures and software packages, significant contributions or syntheses including the works by Brady et al. (1992), Barree et al. (2005), Adachi et al. (2007), Rahman and Rahman (2010), Fisher and Warpinski (2012), Flewelling et al. (2013), Detournay (2016), and Ma et al. (2016).

As others (e.g., Fisher and Warpinski, 2012; Westaway and Younger, 2014) have previously discussed, the form of the ideal vertical hydraulic fracture, which develops in an isotropic medium as a consequence of horizontal minimum principal stress, will depend on the parameter K, the difference between the vertical gradient of σ_h, S, and the vertical gradient of fluid pressure (i.e.,

$$K \qquad = \qquad S - \rho g \qquad\qquad\qquad\qquad (S4.01)$$

ρ and g being, again, the density of the fluid and the acceleration due to gravity). A fracture can thus be envisaged as developing with height H between values of the vertical coordinate, y, -H/2 and +H/2, with the net pressure at y=0 designated as P_o. The form of the vertical variation in fracture width, w, in this situation was derived by Fisher and Warpinski (2012) and was analyzed further by Westaway and Younger (2014). However, rather than the rectangular fracture model investigated by Westaway and Younger (2014), the present analysis considers a variant where w tapers with an elliptical profile as a function of horizontal co-ordinate x, between x=0 at the centre-line of the fracture and x=A, its half-length, with half-length likewise tapering elliptically below a maximum at y=0.

There are, however, a number of potential reasons for departure from such idealized behaviour. First, recent investigations (e.g., Chandler et al., 2016) indicate that shales can have anisotropic mechanical properties that can affect the geometry of fracture development. For example, in the Cretaceous Mancos Shale of the western USA, the measured fracture toughness is lower for fractures developing parallel to bedding than for those with other orientations (Chandler et al., 2016). This variability will cause induced fractures to deviate away from the ideal orientation towards a more bedding-parallel orientation. If such variations in properties were to be confirmed as significant for the Bowland Shale, they would imply, given the WNW dip of the local stratigraphy (Fig. 4), that fractures might develop oriented with azimuths rotated somewhat clockwise from the 'ideal' orientation and with upward growth inclined steeply towards the ESE, rather than vertical. This aspect is noted here in passing, there currently bring no published data for the Bowland Shale on which to base an analysis that incorporates such complexity. Second, as many workers have noted, fracture development may be affected by heterogeneity within the stratigraphic column. Existing planes of weakness, such as bedding or pre-existing fractures, may accommodate the upward propagation of induced fractures by shearing. The resulting lateral steps in the induced fracture may well be impermeable, preventing the injected fluid reaching any upward tensile continuation of this induced fracture (e.g., Zhang and Li, 2016) and thus preventing it from propagating upward farther. This is different from the behaviour inferred at Preese Hall by Harper (2011), who suggested that bedding plane shear might occur but it would *increase* the permeability of the bedding-plane-parallel shear fractures and thus result in extensive leakage of fluid into these fractures. However, since the bedding at Preese Hall is inclined (e.g., Table N1; Fig. 4) it is to be expected that any induced fracture will intersect any bedding plane obliquely, rather than at a right-angle. As a result, the bedding plane will be expected to 'open' obliquely (i.e., accommodate a 'hybrid'-mode combination of tensile and shear displacement), providing an interconnection for the injected fluid between the tensile

fractures on either side. It is thus arguable that at this site the vertical growth of fractures will not be limited by this potential mechanism.

The present analysis will thus concern idealized vertical fractures, rather than the more complex geometries that might be envisaged from the above considerations. The width w of such an ideal model fracture can be written (cf. Fisher and Warpinski, 2012) as

$$w(x,y) = \frac{(1-\nu)}{2\,A\,\mu}\,F\,(2\,P_o + K\,y)\,\sqrt{(H^2 - 4\,y^2)}\,\sqrt{(A^2 - x^2)} \qquad (S4.02)$$

where μ and ν are the shear modulus and Poisson's ratio of the rock in which the fracture develops, $A(y)$ is the half-length of the fracture at vertical position y, and F is a scale factor whose value will be determined below. The maximum half-length of the model fracture $A(y=0)$ can be designated as L. The aspect ratio of this model fracture can be expressed using the parameter C, where

$$A(y=0) \equiv L \equiv C\,H, \qquad (S4.03)$$

so

$$A(y) \equiv C\,\sqrt{(H^2 - 4\,y^2)}. \qquad (S4.04)$$

The volume of this model fracture, V, can be expressed as

$$V = \int_{y=-H/2}^{y=H/2} \int_{x=-A(y)}^{x=A(y)} w(x,y)\,dx\,dy; \qquad (S4.05)$$

after many algebraic steps, one obtains

$$V = \frac{\pi\,(1-\nu)\,C\,F\,P_o\,H^3}{3\,\mu}. \qquad (S4.06)$$

As Fisher and Warpinski (2012) pointed out, the minimum net pressure condition for this model fracture to be held open is given by

$$P_o = \frac{K\,H}{4}. \qquad (S4.07)$$

In general, however, the pressure at y=0 might be larger than this, so this condition can be written more generally as

$$P_o = \frac{M\,K\,H}{4}. \qquad (S4.08)$$

where M≥1. Equation (S4.06) can therefore be rewritten using equation (S4.08) as

$$V = \frac{\pi\,(1-\nu)\,C\,F\,M\,K\,H^4}{12\,\mu}. \qquad (S4.09)$$

For an equidimensional (i.e., circular) model fracture of this type, for which C=1/2, one thus obtains

$$V = \frac{\pi\,(1-\nu)\,F\,M\,K\,H^4}{24\,\mu}. \qquad (S4.10)$$

or, using equation (S4.08) and the fact that H=2 L,

$$V = \frac{4\,\pi\,(1-\nu)\,F\,P_o\,L^3}{3\,\mu}. \qquad (S4.11)$$

The vertical position with the greatest width of this model fracture, along its vertical centre-line, can be found by differentiating equation (S4.02) to obtain $\partial w/\partial y$ at x=0 and solving the resulting equation for $\partial w/\partial y=0$. One thus obtains

$$y_o = \frac{-P_o}{2K} + \sqrt{\left(\frac{P_o^2}{4K^2} + \frac{H^2}{8}\right)}, \tag{S4.12}$$

or, using equation (S4.08),

$$y_o = \left[\frac{-1}{8} + \frac{1}{8}\sqrt{(M^2+8)}\right]H. \tag{S4.13}$$

Figure S3.1 illustrates the resulting variation of y_o/H as a function of M. It is thus evident that with M=1 (i.e., with $P_o= K H/4$, the minimum value at which a fracture of the required height can form; Fisher and Warpinski, 2012), $y_o = H/4$. Recalling that its vertical extent spans y=-H/2 to +H/2, this means that the maximum width develops three quarters of the way up the fracture. Conversely, as M→∞, y_o/H→0, meaning that the maximum width develops halfway up the fracture.

The maximum width w_o of the model fracture can be obtained as $w(x=0, y=y_o)$ from equation (S4.02). In the limit of M=1, where P_o=K H / 4 and y_o = H/4 one thus obtains

$$w_o = \frac{3\sqrt{3}(1-v) F K H^2}{16\mu}, \tag{S4.14}$$

whereas in the limit of M→∞, where y_o→0, one obtains

$$w_o = \frac{(1-v) F M K H^2}{4\mu}, \tag{S4.15}$$

giving, for an equidimensional (i.e., circular) fracture, where C=1/2 so H=2 L
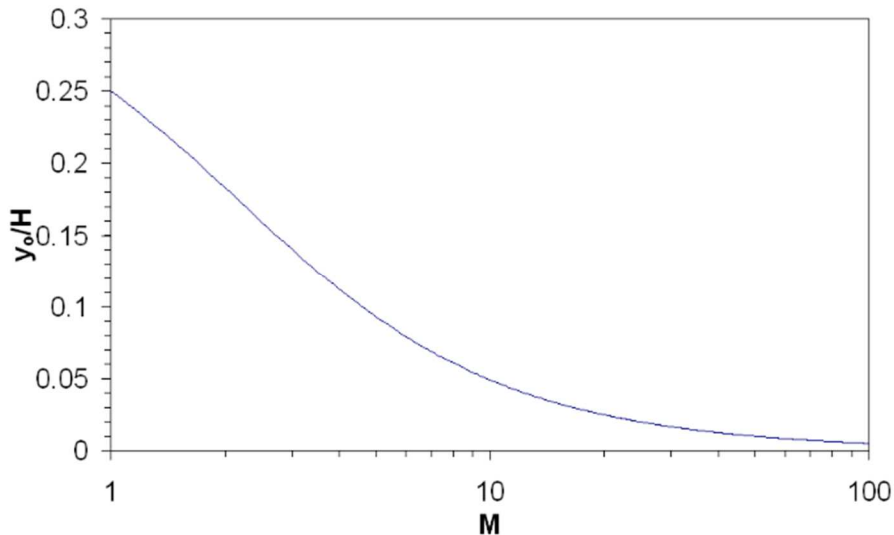
Figure S3.1. *Graph of the relation between y_o/H and M, indicated by equation (S4.13). Here, H denotes the height of a vertical fracture, M denotes the ratio of fluid pressure at y=0 to the minimum value that is able to hold open a vertical fracture of a given H, and y_o is the vertical position (relative to the mid-point of –H/2 at the lower limit and y=+H/2 at the upper limit of the fracture) at which a vertical fracture has maximum width. See text for discussion.*

$$w_o = \frac{2\,(1-\nu)\,F\,P_o\,L}{\mu}, \tag{S4.16}$$

Since M can, in principle, take any value no matter how large, a fracture under significant net pressure can in principle be much wider than a fracture that forms at minimum pressure. However, since the overall volume of the fracture is limited by the fluid available to hold it open (e.g., Fisher and Warpinski, 2012), it follows that a fracture under significant net pressure will be smaller (in terms of H and/or L) than one formed by injection of the same volume of fluid under minimum pressure conditions.

The equidimensional (i.e., circular) case in the limit of M→∞ (such that vertical variations in pressure are small compared with the overall excess pressure) is equivalent to the classical problem of a circular fracture of radius A under uniform net pressure, which was solved by Sneddon (1951; equation 128 on p. 490). As Westaway and Younger (2014) and Westaway (2015a) have discussed, this solution can be written using the present notation as

$$w(r) = \frac{4\,(1-\nu)\,P_o}{\pi\,\mu}\,\sqrt{(L^2 - r^2)}, \tag{S4.17}$$

r being the distance from the centre of the fracture and L being the radius of the fracture, giving

$$w_o \equiv w(r=0) = \frac{4\,(1-\nu)\,P_o\,L}{\pi\,\mu}, \tag{S4.18}$$

and

$$V = \frac{8\,(1-\nu)}{3\,\mu}\,P_o\,L^3. \tag{S4.19}$$

Comparison of equations (S4.16) and (S4.18), or (S4.11) and (S4.19), indicates that F=2/π. Thus, for example, for an equidimensional (i.e., circular) model fracture of this type at minimum pressure one obtains

$$w_o = \frac{3\,\sqrt{3}\,(1-\nu)\,K\,H^2}{8\,\pi\,\mu}, \tag{S4.20}$$

or

$$w_o = \frac{3\,\sqrt{3}\,(1-\nu)\,K\,L^2}{2\,\pi\,\mu}, \tag{S4.21}$$

or

$$w_o = \frac{3\,\sqrt{3}\,(1-\nu)\,P_o\,L}{\pi\,\mu}, \tag{S4.22}$$

with, once again,

$$V = \frac{8\,(1-\nu)\,P_o\,L^3}{3\,\mu}. \tag{S4.23}$$

or

$$V = \frac{4\,(1-\nu)\,K\,L^4}{3\,\mu}. \tag{S4.24}$$

For comparison, the equidimensional (i.e., square) variant of the Westaway and Younger (2014) rectangular fracture model of half-length L, at minimum pressure, specifies

$$w_o = \frac{3 \sqrt{3} (1 - \nu) K L^2}{4 \mu} , \quad \text{(S4.25)}$$

or

$$w_o = \frac{3 \sqrt{3} (1 - \nu) P_o L}{2 \mu} , \quad \text{(S4.26)}$$

(from their equation (A28)), and

$$V = \frac{\pi (1 - \nu) K L^4}{\mu} . \quad \text{(S4.27)}$$

or

$$V = \frac{2 \pi (1 - \nu) P_o L^3}{\mu} . \quad \text{(S4.28)}$$

(from their equation (A32)). For a given set of parameter values, the dimensions of the two models are comparable. Thus, for example, for the same K and L, the circular model has $2/\pi$ or ~0.637 of the maximum width and $4/(3 \pi)$ or ~0.424 of the volume of the square model. For the same K and V, the circular model has $(3 \pi / 4)^{1/4}$ or ~1.239 times the height and width of the square model. For the same P_o and V, the circular model has $(3 \pi / 4)^{1/3}$ or ~1.331 times the height and width of the square model. These modest differences are to be expected given that the square model fracture is open in its 'corners' whereas the circular variant is not.

The aspect ratio C for the induced fracture is not directly specified by the present model and requires separate determination. As many workers have noted, in rheologically-stratified sediments fractures can be 'confined' within shale layers and can thus develop substantial lengths with limited heights, with C>>1; however, one does not expect such behaviour within a relatively homogenous succession such as the Bowland Shale. A potential criterion for constraining C can be derived from consideration of the stress intensity, K_I, during fracturing:

$$K_I = \sigma \sqrt{(\pi \lambda)} , \quad \text{(S4.29)}$$

where σ is the stress tensor element driving the fracture and λ is the length of the fracture in the direction of propagation. Irwin's (1957) work introduced the notion that fractures propagate when K_I reaches or exceeds a critical value, known as the fracture toughness. Assuming that vertical and horizontal fracture growth occur concurrently in the same lithology, both will therefore cease when K_I falls below the fracture toughness. Thus, for a fracture under significant net pressure, σ will approximate the same value, P_o, at all points along the fracture front so λ will be expected to be the same in all directions if K_I is isotropic, making the fracture equidimensional (i.e., C=1/2). Conversely, under minimum pressure conditions, σ will equal 2 P_o at the top of the fracture, for which λ =H, and will equal P_o at its horizontal extremities, which (as noted above; equation (S4.03)) occur halfway up the fracture, where λ = 2 L. Equating the versions of equation (S4.29) for these two points on the fracture front, again assuming that K_I is isotropic, gives

$$2 P_o \sqrt{(\pi H)} = P_o \sqrt{(2 \pi L)}. \quad \text{(S4.30)}$$

or

$$L = 2 H , \quad \text{(S4.31)}$$

so, from equation (S4.03), C=2. Under these minimum-pressure conditions, the model fracture is thus predicted to develop elliptical form, with its length four times its height.

As already noted, Chandler et al. (2016) have argued on the basis of the Mancos Shale that fracture toughness in shale is not isotropic. However, their measurements indicate that fracture toughness does not differ significantly for a fracture developing in 'arrester' mode (corresponding to the upward component of growth of a fracture developing in a vertical plane in response to anisotropic properties determined by horizontal bedding) compared with one developing in 'divider' mode (corresponding to the horizontal component of growth of a fracture developing in a vertical plane in response to anisotropic properties determined by horizontal bedding).

In summary, the above considerations collectively determine the form of the model fracture, points on whose elliptical perimeter have coordinates (x,y) that satisfy the equations

$$x = L \cos(\theta) \qquad \qquad \text{(S4.32)}$$

and

$$y = y_m + \frac{H \sin(\theta)}{2}, \qquad \qquad \text{(S4.33)}$$

where θ varies between 0 and 360°, and y_m (the vertical midpoint of the fracture), L and H are determined using the preceding equations.

The above considerations bear upon the potential for vertical growth of hydraulic fractures to cause environmental pollution, as a result of breaching upward into sediments that are used for water supply (e.g., Fisher and Warpinski, 2012; Davies et al., 2013; Westaway and Younger, 2014; Younger, 2016a). It is evident that if such a breach were to occur then, rather than pollution entering shallower groundwater zones, the result would be for shallower groundwater to flood downward into the fracture, preventing shale gas production, so shale operators have a strong incentive to ensure that this does not happen (e.g., Westaway and Younger, 2014; Younger, 2016b). Nonetheless, the calculations indicate that under minimum pressure conditions the induced fracture height is proportional to the fourth root of the injected volume, whereas at high net pressure it is proportional to the cube root of the injected volume. Moreover, the above suggestion that minimum-pressure conditions will create induced fractures with aspect ratios >1 will further mitigate height growth. Westaway and Younger (2014) recognized this fourth-root dependence for their square and rectangular fracture models under minimum-pressure conditions; it is now apparent that such dependence has wider applicability. Conversely, others (e.g., Flewelling et al., 2013) have previously noted cube root dependence between injected volume and induced fracture height, without realising that this is not always valid; as discussed above, it requires the effect of the vertical gradient in excess pressure to be negligible, so (under real conditions where this gradient is nonzero) will only apply where the net pressure is large compared with the difference in pressure between the top and bottom of the fracture.

5. Theory for Coulomb failure analysis

The Coulomb failure criterion will be used in the present analysis to assess whether the condition for shear failure is satisfied at a given point on a fault or within an unfractured rock mass, like in many previous analyses (e.g., those by Westaway, 2002, 2006, 2015a). The parameter Φ will thus be evaluated:

$$\Phi = \tau - c(\sigma_n - P_f) - S_C, \qquad \qquad \text{(S5.01)}$$

where σ_n, τ and c are the resolved normal stress, shear stress and coefficient of friction on the fault plane (or coefficient of internal friction within the rock mass), and P_f and S_C are the pore-fluid pressure and cohesion of the fault zone or rock mass. $\Phi=0$ marks this condition, with $\Phi<0$ indicating stability at the point analyzed under the current state of stress. In general, this condition for shear failure can also be visualized graphically using the standard Mohr circle construction (Fig. S4.1).
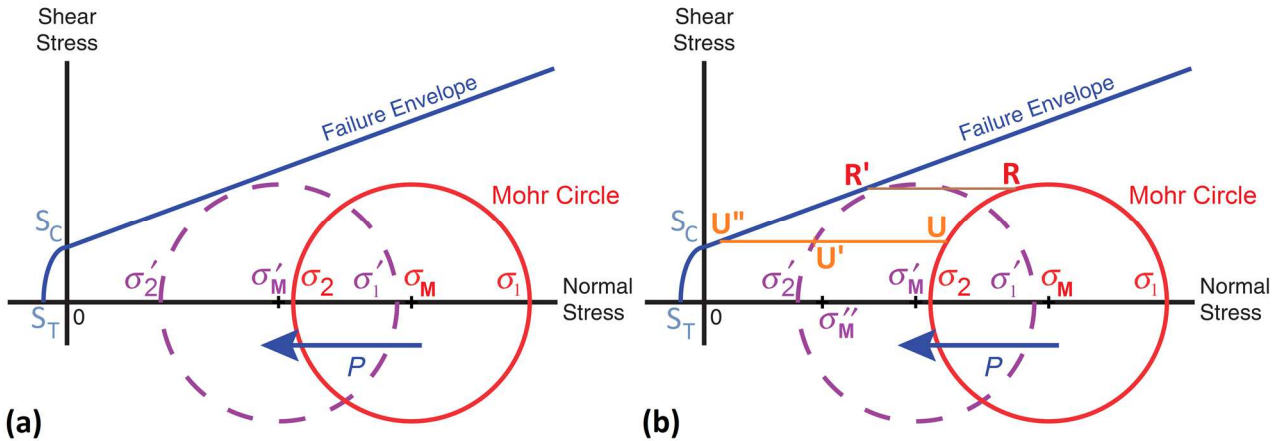
Figure S4.1. *Schematic illustration of the physical mechanism whereby fluid injection can cause induced seismicity, using a Mohr Circle / Failure Envelope representation of stress state. Normal stress (compressional when positive and tensile when negative) is plotted on the horizontal axis, with shear stress on the vertical axis. The maximum and minimum normal stresses acting at a given locality are plotted as σ_1 and σ_2; these lie at opposite ends of a diameter of a circle that is centred at the point on the horizontal axis where the normal stress equals the mean stress σ_M (where $\sigma_M = (\sigma_1 + \sigma_2)/2$) and has radius $\Delta\sigma/2$ where $\Delta\sigma = \sigma_1 - \sigma_2$ is the differential stress. This Mohr Circle represents the set of combinations of normal and shear stress that act in different directions at the locality. The failure envelope represents the set of combinations of normal and shear stress that result in rock failing in shear or in tension, or a pre-existing fault or tensile fracture being reactivated. Its gradient equals the coefficient of friction of a pre-existing fault, or the coefficient of internal friction within a rock mass, c. This envelope passes through a point on the horizontal axis where the tensile normal stress equals the tensile strength S_T of the material, and a point on the vertical axis where the shear stress equals its cohesion S_C. Intact rock will have nonzero S_C and S_T; as discussed by Westaway and Younger (2014), pre-existing faults or fractures in some rocks, such as shale, might likewise have nonzero S_C and S_T, so this possibility is allowed for here. (a) 'Conventional' usage of this method for a permeable rock in which interconnected pore fluid occupies the matrix and its pressure P acts in all directions. When fluid pressure is increased by P, the mean stress decreases from σ_M to $\sigma'_M = \sigma_M - P$ and the Mohr Circle effectively shifts leftward by a distance P (to the dashed circle depicted), resulting in new 'effective' maximum and minimum normal stresses $\sigma'_1 = \sigma_1 - P$ and $\sigma'_2 = \sigma_2 - P$. This normal-stress reduction has the consequence of bringing any fault nearer to the condition for slip, regardless of its orientation, as can be visualized from the closer proximity of all points on the dashed Mohr Circle to the failure envelope. If the pressure increase is large enough such that any point on the adjusted Mohr Circle touches the failure envelope, the fault will slip (or the rock will fail to create a new fault with the orientation indicated) and an induced earthquake will result. The orientation of the failure plane (in Mohr circle space) is that of the normal to the failure envelope at the point where it touches the Mohr circle. (b) Revision to deal with impermeable rocks (cf. Hackston and Rutter, 2016; Rutter and Hackston, in review), in which pore fluid is absent from any matrix and is only present in pre-existing faults and fractures, such that its pressure only acts in the directions perpendicular to the plane of the fault or fracture. Suppose U denotes the orientation (in Mohr circle space) of a pre-existing fault or fracture. The pressure increase within this structure, by P, will displace it in Mohr circle space to U'; since this point lies below the failure envelope, no failure will occur. This is even though the corresponding increase in P displaces another point on the Mohr circle (R, which does not correspond to any pre-existing fault or fracture) to point R', which does lie on the failure envelope. To cause failure on structure U, a much larger pressure increase would be necessary, to displace U to U'' on the failure envelope. At this stage the mean stress would be σ''_M and the orientation of the failure in Mohr circle space would be given by U''-σ''_M which is equivalent to U-σ_M. The orientation of this failure would, therefore, not correspond to that of the normal to the failure envelope. Much of the 'displaced' Mohr circle would lie above this failure envelope but the parts of it that do not correspond to orientations of pre-existing faults or fractures have no meaning in this context and thus provide no indication of the orientation at which failure will occur. When using the Mohr circle construction in this context it is thus preferable to omit the 'displaced' Mohr circle and to only show in Mohr circle space 'displaced' points that correspond to orientations of faults or fractures, as is done in Fig. 8 in the main text. Alternatively, since, in this context of impermeable rocks, failure can only occur on pre-existing structures (unless, of course, the increase in fluid pressure takes the state of stress into the tensile domain), one does not need to use the Mohr circle construction to test whether other orientations might fail preferentially; one can thus solve such problems straightforwardly using vector geometry, as is done in the present text. Modified from Figure 1 of Westaway (2015a), based on Fig. 3 of Rubinstein and Mahani (2015).*

Once the condition $\Phi=0$ occurs and an earthquake results, the state of stress will change across the model, with the patch of fault that slipped becoming de-stressed and an adjoining region of similar dimensions becoming more highly stressed (e.g., Stein et al., 1996, 1997). For rupture of a circular patch of fault, the stress drop $\Delta\sigma$ is given by

$$\Delta\sigma = \frac{3\,(2-\nu)\,\pi}{16\,(1-\nu)}\,\mu\,k\,. \tag{S5.02}$$

(Westaway and Younger, 2014), where k is the ratio of maximum slip to fault radius. Typically, k is observed to be $\sim10^{-4}$ to $\sim10^{-5}$; for the larger of these values, and with $\mu=10$ GPa and $\nu=0.15$, $\Delta\sigma$ is thus ~1.3 MPa. Conversely, regions adjoining patches of fault that slip can become more highly stressed by up to ~1 MPa (e.g., Stein et al., 1996, 1997).

To calculate Φ at points on a model fault, given the stress tensor $\boldsymbol{\sigma}$ with elements σ_{ij} at each point, the following technique (consistent with standard theory; e.g., Ciarlet, 1988; Jaeger et al., 2007, p. 31) has been used. The unit normal vector $\mathbf{n}$ to the fault, with components n_i, was determined, thus giving the Cauchy stress vector $\mathbf{T}$ where, using the standard summation notation,

$$T_j = \sigma_{ij}\,n_j\,. \tag{S5.03}$$

The normal stress was thus determined as

$$\sigma_n = T_i\,n_i = \sigma_{ij}\,n_j\,n_j\,, \tag{S5.04}$$

the corresponding shear stress τ then being found using the standard formula

$$\tau = \sqrt{(T_i\,T_i - \sigma_n^2)}\,. \tag{S5.05}$$

To calculate the corresponding angles for the analysis of the stress state, I note that vector $\mathbf{B}$ where

$$\mathbf{B} = \mathbf{n}\times\mathbf{T} \quad (\text{or } B_i = \varepsilon_{ijk}\,n_j\,T_k) \tag{S5.06}$$

(vectors $\mathbf{n}$ and $\mathbf{T}$ having been defined earlier) is oriented along the null axis and vector $\mathbf{U}$ where

$$\mathbf{U} = \mathbf{n}\times\mathbf{B} \quad (\text{or } U_i = \varepsilon_{ijk}\,n_j\,B_k) \tag{S5.07}$$

is oriented along the direction of slip. The $\times$ symbol in these equations denotes the vector product operation; in the alternative notation, ε_{ijk} is the antisymmetric permutation symbol or Levi-Civita symbol.

References

Adachi, J., Siebrits, E., Peirce, A., Desroches, J., 2007. Computer simulation of hydraulic fractures. International Journal of Rock Mechanics & Mining Sciences, 44, 739–757.

Andrews, I.J., 2013. The Carboniferous Bowland Shale gas study: geology and resource estimation. British Geological Survey for Department of Energy and Climate Change, London, 64 pp.

Baisch, S., Vörös, R., 2011. Geomechanical study of Blackpool seismicity. Report for Cuadrilla Resources, 58 pp. Available online: http://www.cuadrillaresources.com/wp-content/uploads/2012/02/Geomechanical-Study-Appendix-2-2.11.2011.pdf (accessed 30 November 2016)

Baker Hughes, 2011. Wellbore failure analysis and geomechanical modelling in the Bowland Shales, Blackpool, UK: preliminary technical report. Baker Hughes Incorporated, Houston, Texas, 53 pp. Available online: http://www.cuadrillaresources.com/wp-content/uploads/2012/02/Geomechanical-Study-Appendix-1-2.11.2011.pdf (accessed 10 May 2015)

Baptie, B., 2010. Seismogenesis and state of stress in the UK. Tectonophysics, 482, 150–159.

Barree, R.D., Cox, S.A., Gilbert, J.V., Dobson, M.L., 2005. Closing the gap: fracture half length from design, buildup, and production analysis. Society of Petroleum Engineers document SPE-84491-PA. SPE Production & Facilities, 20 (4), 12 pp. doi: http://dx.doi.org/10.2118/84491-PA

Bott, M.H.P., 1988. The Market Weighton gravity anomaly — granite or graben? Proceedings of the Yorkshire Geological Society, 47, 47-53.

Bott, M.H.P., Robinson, J., Kohnstamm, M.A., 1978. Granite beneath Market Weighton, east Yorkshire. Journal of the Geological Society, London, 135, 535-543.

Brady, B., Elbel, J., Mack, M., Morales, H., Nolte, K., Poe, B., 1992. Cracking rock: progress in fracture treatment design. Oilfield Review, October 1992, 4-17.

Bridgland, D.R., Westaway, R., Howard, A.J., Innes, J.B., Long, A.J., Mitchell, W.A., White, M.J., White, T.S., 2010. The role of glacio-isostasy in the formation of post-glacial river terraces in relation to the MIS 2 ice limit: evidence from northern England. Proceedings of the Geologists' Association, 121, 113-127.

Bridgland, D.R., White, T.S., Howard, A.J., White, M.J., Westaway, R., 2014. Chapter 6. Synthesis: the Pleistocene evolution and human occupation of the Trent catchment. In: Bridgland, D.R., Howard, A.J., White, M.J., White, T.S. (eds), The Quaternary of the Trent. Oxbow Books, Oxford, pp. 295-372.

British Coal Corporation, 1997. Three-dimensional seismic surveying to investigate the geological structure of shear zones within the Selby coalfield. European Union, Directorate-General Energy, report EUR 17161 EN. Office for Official Publications of the European Communities, Luxembourg, 122 pp.

Browning, G.R.J., Jacob, A.W.B., 1970. Preliminary study of the North of England earthquake of August 9, 1970. Nature, 228, 835-837.

Busby, J., Lewis, M., Reeves, H., Lawley, R., 2009. Initial geological considerations before installing ground source heat pump systems Quarterly Journal of Engineering Geology and Hydrogeology, 42, 295-306.

Busby, J., Kingdon, A., Williams, J., 2011. The measured shallow temperature field in Britain. Quarterly Journal of Engineering Geology and Hydrogeology, 44, 373-387.

Carter, P.G., Mills, D.A., 1976. Engineering geological investigations for the Kielder Tunnels. Quarterly Journal of Engineering Geology and Hydrogeology, 9, 125-141.

Cartwright, P.B., 1997. A review of recent in-situ stress measurements in United Kingdom Coal Measures strata. In: Sugawara, K., Obara, Y. (eds), Rock Stress: Proceedings of the International Symposium on Rock Stress, Kumamoto, Japan, 7-10 October 1997. Balkema, Rotterdam, pp. 469-474.

Chadwick, R.A., Holliday, D.W., Holloway, S., Hulbert, A.G., 1995. The structure and evolution of the Northumberland-Solway Basin and adjacent areas. British Geological Survey Subsurface Memoir. HMSO, London, 90 pp.

Chadwick, R.A., Pharaoh, T.C., Williamson, J.P., Musson, R.M.W., 1996. Seismotectonics of the UK. British Geological Survey Technical Report, WA/96/3C. British Geological Survey, Keyworth, Nottingham, 172 pp. Available online: http://core.ac.uk/download/pdf/59774.pdf (accessed 16 October 2015)

Chandler, M.R., Meredith, P.G., Brantut, N., Crawford, B.R., 2016. Fracture toughness anisotropy in shale. Journal of Geophysical Research, Solid Earth, 121, 1706–1729, doi: 10.1002/2015JB012756.

Ciarlet, P.G., 1988. Mathematical Elasticity: Three-dimensional elasticity, Volume 1. Elsevier, Amsterdam, 455 pp.

Clarke, H., 2016. Reply to "Hydraulic fracturing in thick shale basins: problems in identifying faults in the Bowland and Weald Basins, UK" by D.K. Smythe. Interactive Discussion item SC9, 7 pp. Available online: http://www.solid-earth-discuss.net/se-2015-134/discussion (accessed 3 March 2016)

Clarke, H., Eisner, L., Styles, P., Turner, P., 2014. Felt seismicity associated with shale gas hydraulic fracturing: The first documented example in Europe. Geophysical Research Letters, 41, 8308–8314.

Cuadrilla, 2014. Temporary Shale Gas Exploration; Preston New Road, Lancashire; Environmental Statement, Appendix L – Induced Seismicity. Cuadrilla Bowland Ltd., Lichfield. 140 pp. Available online: http://planningregister.lancashire.gov.uk/Attachments/6586/PNR_ES_Vol2_Appndx_L_Induced_Seismicity.pdf (accessed 9 March 2015).

Davies, R., Foulger, G., Bindley, A., Styles, P., 2013. Induced seismicity and hydraulic fracturing for the recovery of hydrocarbons. Marine and Petroleum Geology, 45, 171-185.

de Paola, N., Holdsworth, R.E., McCaffrey, K.J.W., 2005. The influence of lithology and pre-existing structures on reservoir-scale faulting patterns in transtensional rift zones. Journal of the Geological Society, London, 162, 471–480.

de Pater, C.J., Baisch, S., 2011. Geomechanical study of Bowland Shale seismicity: synthesis report. Cuadrilla Resources Ltd., Lichfield, 71 pp. Available online: http://www.rijksoverheid.nl/bestanden/documenten-en-publicaties/rapporten/2011/11/04/rapport-geomechanical-study-of-bowland-shale-seismicity/rapport-geomechanical-study-of-bowland-shale-seismicity.pdf (accessed 5 August 2015)

Detournay, E., 2016. Mechanics of hydraulic fractures. Annual Review of Fluid Mechanics, 48, 311–339.

Downing, R.A., Gray, D.A. (eds), 1986. Geothermal Energy - The Potential in the United Kingdom. Her Majesty's Stationery Office, London, 187 pp.

Dunham, K.C., 1974. Granite beneath the Pennines in North Yorkshire. Proceedings of the Yorkshire Geological Society, 40, 191-194.

Dunham, K.C., Wilson, A.A., 1985. Geology of the Northern Pennine Orefield; Volume 2, Stainmore to Craven. Economic Memoir of the British Geological Survey, England and Wales, Sheets 40, 41, and 50 and parts of 31, 32, 51, 60 and 61.

Eshelby, J.D., 1957. The determination of the elastic field of an ellipsoidal inclusion, and related problems. Proceedings of the Royal Society of London, Series A, 241, 376-396.

Evans, C.J., Brereton, N.R., 1990. In situ crustal stress in the United Kingdom from borehole breakouts. In: Hurst, A., Lovell, M.A., Morton, A.C. (eds), Geological Applications of Wireline Logs. Geological Society, London, Special Publications, 48, 327-338.

Fekete Associates, 2013. Wellbore Configuration. IHS, Inc., Houston, Texas. Available online: http://www.fekete.com/SAN/WebHelp/virtuwell/webhelp/c-sw-wellbore.htm (accessed 7 August 2016)

Ferrill, D.A., Morris, A.P., Smart, K.J., 2007. Stratigraphic control on extensional fault propagation folding: Big Brushy Canyon monocline, Sierra Del Carmen, Texas. In: Jolley, S.J., Barr, D., Walsh, J.J., Knipe, R.J. (eds), Structurally Complex Reservoirs. Geological Society, London, Special Publications, 292, 203-217.

Fisher, K., Warpinski, N., 2012. Hydraulic-fracture-height growth: Real data. Society of Petroleum Engineers, Productions and Operations Journal, 27, 8–19.

Flewelling, S.A., Tymchak, M.P., Warpinski, N., 2013. Hydraulic fracture height limits and fault interactions in tight oil and gas formations. Geophysical Research Letters, 40, 3602–3606.

Fraser, A.J., Gawthorpe, R.L., 2003. An atlas of Carboniferous basin evolution in northern England. Geological Society, London, Memoir 28, 79 pp.

Fraser, A.J., Nash, A.J., Steele, R.P., Ebdon, C.C., 1990. A regional assessment of the intra-Carboniferous play of northern England. In: Brooks, J. (ed.), Classic Petroleum Provinces. Geological Society, London, Special Publications, 50, 417-440.

Froidevaux, C., Paquin, C., Souriau, M., 1980. Tectonic stresses in France: in situ measurements with a flat jack. Journal of Geophysical Research, 85, 6342-6346.

Gao Quan, Tao JunLiang, Hu JianYing, Yu Xiong, 2015. Laboratory study on the mechanical behaviors of an anisotropic shale rock. Journal of Rock Mechanics and Geotechnical Engineering, 7, 213–219.

Gawthorpe, R.L., Clemmey, H., 1985. Geometry of submarine slides in the Bowland Basin (Dinantian) and their relation to debris flows. Journal of the Geological Society, London, 142, 555-565.

GFZ, 2015. Download the World Stress Map database Release 2008. http://dc-app3-14.gfz-potsdam.de/pub/stress_data/stress_data_frame.html (accessed 10 May 2015)

Griffith, A.A., 1921. The phenomena of rupture and flow in solids. Philosophical Transactions of the Royal Society of London, Series A, 221, 163–198.

Griffith, A.A., 1924. The theory of rupture. In: Biezeno, C.B., Burgers, J.M. (eds), Proceedings of the First International Congress of Applied Mechanics, Delft, The Netherlands. Technische Boekhandel en Drukkerij, Delft, The Netherlands, pp. 55–63.

Hackston, A., Rutter, E., 2016. The Mohr–Coulomb criterion for intact rock strength and friction – a re-evaluation and consideration of failure under polyaxial stresses. Solid Earth, 7, 493–508. doi: 10.5194/se-7-493-2016

Harding, P., Bridgland, D.R., Allen, P., Bradley, P., Grant, M.J, Peat, D., Schwenninger, J.-L., Scott, R., Westaway, R., White, T.S., 2012 Chronology of the Lower and Middle Palaeolithic in NW Europe: developer-funded investigations at Dunbridge, Hampshire, southern England. Proceedings of the Geologists' Association, 123, 584-607.

Harper, T.R., 2011. Well Preese Hall-1: The mechanism of induced seismicity. Geosphere Ltd., Beaworthy, Devon, 67 pp. Available online: http://www.cuadrillaresources.com/wp-content/uploads/2012/06/Geosphere-Final-Report.pdf (accessed 17 October 2015)

Heidbach, O., Tingay, M., Barth, A., Reinecker, J., Kurfeß, D., Müller, B., 2010. Global crustal stress pattern based on the World Stress Map database release 2008. Tectonophysics, 482, 3-15.

Hills, E.S., 1966. Elements of Structural Geology. Methuen, London, 483 pp.

Hirschfeldt, M., 2016. API casing table specification. Available online: http://www.oilproduction.net/files/002-apicasing.pdf (accessed 7 August 2016)

iGas, 2014. Executive summary of Barton Moss well results. iGas Energy plc, London, 6 pp. Available online: www.igasplc.com/media/10895/barton-moss-results.pdf (accessed 1 December 2016)

Irwin, G., 1957. Analysis of stresses and strains near the end of a crack traversing a plate. Journal of Applied Mechanics, 24, 361–364.

Jaeger, J.C., Cook, N.G.W., Zimmerman, R., 2007. Fundamentals of rock mechanics, 4th edition. Blackwell, Oxford, 475 pp.

Kimbell, G.S., Young, B., Millward, D., Crowley, Q.G., 2010. The North Pennine batholith (Weardale Granite) of northern England: new data on its age and form. Proceedings of the Yorkshire Geological Society, 58, 107-128.

King, D., Browne, J., Layard, R., O'Donnell, G., Rees, M., Stern, N., Turner, A., 2015. A Global Apollo Programme to Combat Climate Change. Centre for Economic Performance, London School of Economics and Political Science, 40 pp. Available online: http://cep.lse.ac.uk/pubs/download/special/Global_Apollo_Programme_Report.pdf (accessed 9 October 2015)

Kingdon, A., Fellgett, M.W., Williams, J.D.O., 2016. Use of borehole imaging to improve understanding of the in-situ stress orientation of Central and Northern England and its implications for unconventional hydrocarbon resources. Marine and Petroleum Geology, 73, 1-20.

Kirby, G.A., Baily, H.E., Chadwick, R.A., Evans, D.J., Holliday, D.W., Holloway, S., Hulbert, A.G., Pharaoh, T.C., Smith, N.J.P., Aitkenhead, N., Birch, B. 2000. The structure and evolution of the Craven Basin and adjacent areas. Subsurface Memoir of the British Geological Survey.

Lyons, W.C., Go BoYun, Graham, R.L., Hawley, G.D., 2009. Air and Gas Drilling Manual: Applications for Oil and Gas Recovery Wells and Geothermal Fluids Recovery Wells. Elsevier, Amsterdam.

Ma Shou, Guo JianChun, Li LianChong, Xia YingJie, Yang Tao, 2016. Experimental and numerical study on fracture propagation near open-hole horizontal well under hydraulic pressure. European Journal of Environmental and Civil Engineering, 20, 412–430.

McKenzie, D.P., 1969. The relationship between fault plane solutions for earthquakes and the directions of the principal stresses. Bulletin of the Seismological Society of America, 59, 591-601.

McKeon, B.J., Swanson, C.J., Zagarola, M.V., Donnelly, R.J., Smits, A.J., 2004. Friction factors for smooth pipe flow. Journal of Fluid Mechanics, 511, 41–44.

Mark, C., Gadde, M., 2008. Global trends in coal mine horizontal stress measurements. In: Peng, S.S., Tadolini, S.C., Mark, C., Finfinger, G.L., Heasley, K.A., Khair, A.W., Luo, Y. (eds), Proceedings of the 27th International Conference on Ground Control in Mining. West Virginia University Press, Morgantown, West Virginia, pp. 319-331.

Millward, D., 2006. Caledonian intrusive rocks of northern England and the Midlands. In: Brenchley, P.J., Rawson, P.F. (eds), The Geology of England and Wales, 2nd edition. The Geological Society, London, pp. 147-154.

Moody, L.F., 1944. Friction factors for pipe flow. Transactions of the American Society of Mechanical Engineers, 66, 671–684.

Musson, R.M.W., 2007. British earthquakes. Proceedings of the Geologists' Association, 118, 305-337.

Parker, R., 1999. The Rosemanowes HDR project 1983-1991. Geothermics, 28, 603-615.

Pharaoh, T.C., Allsop, J.M., Holliday, D.W., Merriman, R.J., Kimbell, G.S., Rundle, C.C., Brewer, T.S., Noble, S.R., Evans, C.J., 1997. The Moorby Microgranite: a deformed high level intrusion of Ordovician age in the concealed Caledonian basement of Lincolnshire. Proceedings of the Yorkshire Geological Society, 51, 329–342.

Pharaoh, T.C., Vincent, C., Bentham, M.S., Hulbert, A.G., Waters, C.N., Smith, N.J.P., 2011. Structure and evolution of the East Midlands region of the Pennine Basin. Subsurface Memoir of the British Geological Survey. British Geological Survey, Nottingham, 144 pp.

Pine, R.J., Batchelor, A.S., 1984. Downward migration of shearing in jointed rock during hydraulic injections. International Journal of Rock Mechanics and Mining Sciences & Geomechanics Abstracts, 21 (5), 249-263.

Rahman, M.M., Rahman, M.K., 2010. A review of hydraulic fracture models and development of an improved pseudo-3d model for stimulating tight oil/gas sand. Energy Sources, Part A, 32, 1416–1436.

Rankine, W.J.M., 1843. On the causes of the unexpected breakage of the journals of railway axles, and on the means of preventing such accidents by observing the law of continuity in their construction. Minutes of the Proceedings of the Institution of Civil Engineers, 2, 105-107.

Rankine, W.J.M., 1858. A Manual of Applied Mechanics. Richard Griffin and Company, Glasgow, 640 pp.

Richards, H.G., Parker, R.H., Green, A.S.P., Jones, R.H., Nicholls, J.D.M., Nicol, D.A.C., Randall, M.M., Richards, S., Stewart, R.C., Willis-Richards, J., 1994. The performance and characteristics of the experimental hot dry rock geothermal reservoir at Rosemanowes, Cornwall (1985–1988). Geothermics, 23, 73-109.

Richardson, R.M., Solomon, S.C., Sleep, N.H., 1979. Tectonic stress in the plates. Reviews of Geophysics and Space Physics, 17, 981-1019.

Ringrose, P.S., 1989. Recent fault movement and palaeoseismicity in western Scotland. Tectonophysics, 163, 315-321.

Robson, D.A., 1964. The Acklington Dyke – a proton magnetometer survey. Proceedings of the Yorkshire Geological Society, 34, 293-308.

Robson, D.A., 1977. The structural history of the Cheviot and adjacent regions. Scottish Journal of Geology, 13, 255-262.

Roche, V., Grob, M., Eyre, T., Van Der Baan, M., 2015. Statistical characteristics of microseismic events and in-situ stress in the Horn River Basin. In: Proceedings of GeoConvention 2015, Calgary, Canada, 4-8 May 2015, 5 pp. Available online: http://www.geoconvention.com/uploads/2015abstracts/080_GC2015_Statistical_characteristics_of_microseismic_events.pdf (accessed 11 May 2015)

Rollin, K.E., 1995. A simple heat-flow quality function and appraisal of heat-flow measurements and heat-flow estimates from the UK Geothermal Catalogue. Tectonophysics, 244, 185–196.

Rowland, J.P., 1933. Wensleydale earthquake. Nature, 131, 128.

Rubinstein, J.L., Mahani, A.B., 2015. Myths and facts on waste water injection, hydraulic fracturing, enhanced oil recovery, and induced seismicity. Seismological Research Letters, 86, 1060-1067.

Rutter, E.H., Hackston, A., in review. On the effective stress law for rock-on-rock frictional sliding, and fault slip triggered by means of fluid injection

Rutter, E.H., Mecklenburgh, J., 2017. Hydraulic conductivity of bedding-parallel cracks in shale as a function of shear and normal stress. In: Rutter, E.H., Mecklenburgh, J., Taylor, K.G. (eds), Geomechanical and Petrophysical Properties of Mudrocks. Geological Society, London, Special Publications, 454, http://doi.org/10.1144/SP454.

Sneddon, I.N., 1951. Fourier Transforms. McGraw-Hill, New York, 542 pp.

Stein, R.S., Barka, A.A., Dieterich, J.H., 1997. Progressive failure on the North Anatolian fault since 1939 by earthquake stress triggering. Geophysical Journal International, 128, 594-604.

Stein, R.S., Dieterich, J.H., Barka, A.A., 1996. Role of stress triggering in earthquake migration on the North Anatolian Fault. Physics and Chemistry of the Earth, 21, 225-230.

Stewart, I., Firth, C., Rust, D., Collins, P., Firth, J., 2001. Postglacial fault movement and palaeoseismicity in western Scotland: a reappraisal of the Kinloch Hourn fault, Kintail. Journal of Seismology, 5, 307-328.

Sylvester, A.G., 1988. Strike-slip faults. GSA Bulletin, 100, 1666-1703.

Turner, B.R., Robson, D.A., Dearman, W.R., Jones, J.M., Magraw, D., Smith, F.W., 1995. Structure. In: Johnson, G.A.L. (ed.), Robson's Geology of North East England, 2nd edition. Transactions of the Natural History Society of Northumbria, 56, 331-343.

Versey, H.C., 1939. The North Sea earthquake of 1931 June 7. Monthly Notices of the Royal Astronomical Society, Geophysical Supplement, 4 (6), 416–423.

Versey, H.C. 1948. The Skipton earthquake of 1944. Transactions of the Leeds Geological. Association 6, 95-97.

Versey, H.C., 1949. Skipton earthquake of 1944. Nature, 163, 596.

Wan RenPu, 2011. Advanced Well Completion Engineering, 3rd Edition. Elsevier, Amsterdam, 715 pp.

Waters, C.N., Davies, S.J., 2006. Carboniferous: extensional basins, advancing deltas and coal swamps. In: Brenchley, P.J., Rawson, P.F. (eds), The Geology of England and Wales, 2nd edition. The Geological Society, London, pp. 173-223.

Waters, C.N., Somerville, I.D., Jones, N.S., and 16 others, 2011. A revised correlation of Carboniferous Rocks in the British Isles. Geological Society, London, Special Report 26.

Waters, C.N., Glover, B.W., Powell, J.H., 1994. Structural synthesis of south Staffordshire, UK: implications for the Variscan evolution of the Pennine Basin. Journal of the Geological Society, London, 151, 697–713.

Westaway, R., 2002. Seasonal seismicity of northern California before the great 1906 earthquake. Pure and Applied Geophysics 159, 7-62.

Westaway, R., 2006. Investigation of coupling between surface processes and induced flow in the lower continental crust as a cause of intraplate seismicity. Earth Surface Processes and Landforms 31, 1480-1509.

Westaway, R., 2009. Quaternary uplift of northern England. Global and Planetary Change, 68, 357-382.

Westaway R., 2010. Cenozoic uplift of southwest England. Journal of Quaternary Science, 25, 419-432.

Westaway R., 2015a. Induced seismicity. In: Environmental and Health Issues in Unconventional Oil and Gas Development, Edited by: Debra Kaden and Tracie L. Rose. Elsevier, Amsterdam, pp. 175-210.

Westaway R., 2015b. Review of 'Caves and Karst of the Yorkshire Dales, Volume 1, edited by Tony Waltham and David Lowe.' British Cave Research Association, Buxton, 2013, 264 pp. Quaternary Science Reviews, 126, 276-277.

Westaway R., 2016a. The importance of characterizing uncertainty in controversial geoscience applications: induced seismicity associated with hydraulic fracturing for shale gas in northwest England. Proceedings of the Geologists' Association, 127, 1–17.

Westaway, R., 2016b. Some additional thoughts on Preese Hall. Solid Earth Discussions, Interactive Discussion item SC10, 9 pp. Available online: http://www.solid-earth-discuss.net/se-2015-134/discussion (accessed 13 August 2016)

Westaway R., 2017. Isostatic compensation of Quaternary vertical crustal motions: coupling between uplift of Britain and subsidence beneath the North Sea. Journal of Quaternary Science, in press. doi: 10.1002/jqs.2832.

Westaway, R., Bridgland, D.R., White, M.J., 2006. The Quaternary uplift history of central southern England: evidence from the terraces of the Solent River system and nearby raised beaches, Quaternary Science Reviews, 25, 2212-2250.

Westaway, R., Bridgland, D.R., White, T.S., Howard, A.J., White, M.J., 2015. The use of uplift modelling in the reconstruction of drainage development and landscape evolution in the repeatedly glaciated Trent catchment, English Midlands, UK. Proceedings of the Geologists' Association, 126, 480–521.

Westaway, R., Younger, P.L., 2014. Quantification of potential macroseismic effects of the induced seismicity that might result from hydraulic fracturing for shale gas exploitation in the UK. Quarterly Journal of Engineering Geology and Hydrogeology, 47, 333–350.

Withjack, M.O., Olson, J., Peterson, E., 1990. Experimental models of extensional forced folds. AAPG Bulletin, 74, 1038-1054.

Woodcock, N.H., Fischer, M., 1986. Strike-slip duplexes. Journal of Structural Geology, 8, 725-735.

Younger, P.L., 2016a. How can we be sure fracking will not pollute aquifers? Lessons from a major longwall coal mining analogue (Selby, Yorkshire, UK). Earth and Environmental Science Transactions of the Royal Society of Edinburgh, 106, 89-113.

Younger, P.L., 2016b. Interactive comment on "Hydraulic fracturing in thick shale basins: problems in identifying faults in the Bowland and Weald Basins, UK" by David K. Smythe. Solid Earth Discussions, Interactive Discussion item SC6, 8 pp. Available online: http://www.solid-earth-discuss.net/se-2015-134/discussion (accessed 21 August 2016)

Zhang ZhaoBin, Li Xiao, 2016. The shear mechanisms of natural fractures during the hydraulic stimulation of shale gas reservoirs. Materials, 9, 713, 14 pp. doi: 10.3390/ma9090713